Title
Growth and Band Engineering of Layered Gallium Monochalcogenide Nanowires

Author
Cardona, Edy

Publication Date
2021

Growth and Band Engineering of Layered Gallium Monochalcogenide Nanowires

by

Edy Cardona

A dissertation submitted in partial satisfaction of the

requirements for the degree of

Doctor of Philosophy

in

Engineering – Materials Science and Engineering

in the

Graduate Division

of the

University of California, Berkeley

Committee in charge:

Professor Oscar Dubón, Chair
Professor Junqiao Wu
Professor Costas Grigoropoulos

Summer 2021

Growth and Band Engineering of Layered Gallium Monochalcogenide Nanowires

by

Edy Cardona

Abstract

Growth and Band Engineering of Layered Gallium Monochalcogenide Nanowires

by

Edy Cardona

Doctor of Philosophy in Engineering – Materials Science and Engineering

University of California, Berkeley

Professor Oscar Dubón, Chair

Ternary alloys composed of layered gallium monochalcogenides—that is GaS, GaSe, and GaTe—possess improved and tunable optoelectronic properties compared to their constituent binary compounds. In particular, the compositional dependence of the bandgap has been shown to be linear for $GaSe_{1-x}S_x$ and slightly bowed for $GaSe_{1-x}Te_x$ alloys. The difference in the bowing behavior between these two alloys arises from the mismatch in electronegativity, ionization energy, and atomic radius between the chalcogens in each system. Based on this trend, $GaS_{1-x}Te_x$ alloys are expected to exhibit a much larger degree of band gap bowing as a result of the higher mismatch between sulfur and tellurium. However, $GaS_{1-x}Te_x$ alloys have not been synthesized thus far because of the higher volatility of sulfur and tellurium—which present experimental challenges to attaining compositional control—and the lower miscibility between the more stable GaS and GaTe compounds.

In this dissertation, sulfur-rich, $GaS_{1-x}Te_x$ alloy nanostructures were synthesized for the first time using a gold-catalyzed, vapor transport method. The dominant growth mechanism for alloy nanowires is the vapor-liquid-solid growth mechanism as evidenced by the presence of catalyst droplets at the end of the nanowires and by the large ratio of the length to width of the alloy nanowires. The morphology of pure GaS nanostructures is comprised of straight, zigzag, and saw-tooth nanobelts while the morphology of the alloy nanostructures is predominantly straight nanowires with trapezoidal cross-section. Furthermore, the fast-growth direction of GaS nanobelts is in the direction of layer edges while the growth direction of sulfur-rich, alloy nanowires is parallel to the c-axis (i.e., normal to the van der Waals layers). Alloy, c-axis nanowires offer new and exciting opportunities for sensor technologies due to the dangling bonds decorating the nanowire.

In addition to the changes in growth direction, the alloy nanowires showed an initial red shift in the Raman-active modes from GaS Raman-active modes with tellurium incorporation. As the tellurium composition continued to increase, the Raman-active modes did not continue

to red shift. This behavior may indicate a solubility limit of substitutional tellurium in sulfur-rich $GaS_{1-x}Te_x$ alloys.

Sulfur-rich, alloy nanowires also showed strong luminescence. The room-temperature photoluminescence (PL) signal is characterized by strong peaks at 1.42 eV and 1.55 eV while the low-temperature (85 K) cathodoluminescence (CL) signal has a high-intensity peak at 2.23 eV. A band model was proposed to explain the origins of the luminescence observed. In this model, two types of transitions can occur. In the first type of transition, CL excites carriers across the direct band gap of the alloy nanowire. This transitions corresponds to the high-intensity CL peak located at 2.23 eV. The second type of transition that occurs is the indirect exciton transition. Each of the two high-intensity, PL peaks is attributed to an indirect exciton transition from a different polytype. These observations point to a decrease of the fundamental (indirect) band gap of GaS by approximately 1 eV by its dilute alloying with GaTe (i.e., $x < 0.1$ in $GaS_{1-x}Te_x$). Overall, the environmental stability and strong luminescence in the near infra-red region displayed by the $GaS_{1-x}Te_x$ alloy nanowires makes this material system a promising candidate for optoelectronic applications, such as photodetector technology.

Finally, DFT calculations support a picture in which the $GaS_{1-x}Te_x$ alloy system displays strong band gap bowing in the sulfur-rich side of composition (i.e., $x < 0.5$). These results are consistent with PL and CL results. The bowing originates from the large differences in atomic size and electronegativity between sulfur and tellurium. Further, DFT calculations predict a miscibility gap as well as a metastable phase in the $GaS_{1-x}Te_x$ alloy system. Such immiscibility supports the attribution of the optical trends (Raman and PL) with increasing tellurium composition to a saturation of the substitutional incorporation of tellurium in sulfur-rich alloys. These calculations contribute to the foundation for studying highly-mismatched, layered materials possessing different crystal structures and polytypes.

To my parents, Adolfo and Oralia,
and my siblings, Adolfo Jr., Tanya, Astrid, Pedro, and Benny

Contents

List of Figures

List of Tables

Acknowledgments

I would like to express my profound gratitude to the many mentors, colleagues, friends and family who helped me complete this work and finish my degree.

I would like to thank my advisor, Professor Oscar Dubón, for his unwavering support and belief in me. I am grateful for his mentorship, guidance, patience, care and encouragement at all steps during my Ph.D. process. I truly admire his commitment and passion for scientific discovery and excellence as well as his efforts to advance diversity and inclusion in academia. It has been a true privilege to have worked with and learned from him.

I would like to thank my dissertation committee, Professor Junqiao Wu and Professor Costas Grigoropoulos, for taking the time to review and provide insight on this work. I would also like to thank Professor Mark Asta and Professor Jie Yao for serving on my qualifying exam committee and for providing valuable insight into this project as well.

I would like to thank past and present Dubón Group members, in particular Dr. Petra Specht, Dr. Jose Fonseca, Dr. Thang Pham, James Chavez, Dr. Carlos Biaou, Dr. Chris Francis, Dr. Raj Kumar, Dr. Maribel Jaquez, Clarissa Bhargava, and Anthony Salazar for their insight, advice, and support. A very special thanks to the bright, undergraduate researchers that worked with me, Andre Palacios and Daniel Paulo-Wach, for putting their trust in me as a mentor; I thank them both for their motivation, diligence, insight, and contributions to this project. I feel grateful and privileged to have been part of such wonderful research group.

I would like to thank Dr. Shaul Aloni at the Molecular Foundry for his mentorship and contributions to this project. He has been a great source of encouragement and I have learned much from him. I would also like to thank Jeffrey Beemen for all of his help in setting up experiments at LBNL; I appreciate his patience and willingness to always help others.

I would like to thank the many support groups I have had the privilege to be part of at UC Berkeley. I am grateful to my peers in the MSE/AS&T departments for their support in studying for classes, preliminary exams, and qualifying exams. I am grateful to the LAGSES community for proving support during my time as a graduate student and for the wonderful friendships that developed from that support. I would like to warmly thank Dr. Adisa Anderson and Dr. Rich Chiovarelli for holding spaces of support for students at UC Berkeley. Lastly, I would like to thank Alex and Rex de Guia at the Student Learning Center for first teaching me about having a growth-mindset as an undergraduate student at Berkeley and for giving me tools to become a better learner.

I am grateful to the undergraduate programs that opened the door for me to a new world of discovery by allowing me to participate in undergraduate research experiences. A very

heartfelt thanks to the Cal NERDS program, and its directors Diana Lizarraga and Chris Noble, for being a foundational pillar of support during my undergraduate and graduate studies at UC Berkeley. Thank you for being my home away from home. I thank the Environmental Leadership Pathway (ELP) program and Dr. Sang Lee for first teaching me about research. I am very thankful to Meltem Erol and the Center of Integrated Nanomechanical Systems (COINS) program for giving me my first opportunity to conduct research at UC Berkeley. Since then, Meltem Erol has been a great source of support and encouragement during my Ph.D. journey. I would also like to thank Professor Michael Aziz at Harvard's School of Engineering and Applied Sciences (SEAS) and Professor Junqiao Wu at Berkeley's Materials Science and Engineering department for allowing me to work in their laboratory as an undergraduate student and for providing invaluable mentorship. Finally, I am very grateful to the graduate student mentors I had as an undergraduate researcher, Dr. Paul Birkmeyer, Dr. Daniel Recht, and Dr. Kevin Wang, for being great teachers.

I would like to thank my parents, Adolfo and Oralia, and my siblings, Adolfo Jr., Tania, Astrid, Peter, and Benny for all their teachings, patience, support, and belief in me. From them, I learned to be kind, loving, and strive to help others. They have been there for me during the most challenging and wonderful of times and have loved me unconditionally at every step of the way. This accomplishment is as much theirs as it is mine.

Lastly, I would like to thank the NSF Bridge to the Doctorate Fellowship for providing funding during the first two years of my doctoral program. I would also like to acknowledge that this work was supported by the Electronic Materials Program, funded by the Director, Office of Science, Office of Basic Energy Sciences, Materials Sciences and Engineering Division of the US Department of Energy under Contract No. DE-AC02-05Ch11231. Finally, my advisor and I recognize and honor that this work was performed at the Berkeley Lab and UC Berkeley, which sit on the territory of xučyun (Huichin), the ancestral and unceded land of the Chochenyo speaking Ohlone people, and that every member of the Berkeley community continues to benefit from the use and occupation of this land.

Chapter 1

Introduction

1.1 Brief Overview of Layered Materials

1.1.1 Graphene

Layered materials possess bonding anisotropy with strong covalent-ionic, intralayer bonding and weak van der Waals, interlayer bonding. This bonding anisotropy allows for the cleavage of atomically thin crystals (i.e. single crystals with one atomic layer in thickness, also known as 2D materials). Layered materials possess many desirable properties. For instance, a layered material, when exfoliated, possesses a pristine surface free of dangling bonds. The absence of dangling bonds at the surface of a material renders its band gap free of surface states [1]. Consequently, the energy difference between the bulk energy bands and the Fermi energy is constant throughout the semiconductor, removing the energy barrier, known as Fermi level pinning, that forms when two defective surfaces come in contact [1]. This property makes layered materials desirable, for example, for tuning electrical contacts.

The stability of atomically thin crystals was not always as clear as it is today. In the case of graphene, it was believed that curved structures, such as nanotubes, were more stable than planar structures [2]. Furthermore, experiments involving thin-film growth indicated that films below a certain thickness decomposed or phase segregated [3, 4]. However, with the isolation of freestanding graphene in 2004, atomically thin crystals were proven to be stable, macroscopically continuous, and to possess high crystal quality [3]. This discovery opened the door to a wide range of new physics and applications [2].

Graphene, in particular, possesses remarkable properties as a result of its bonding hybridization and electronic structure. Graphene is a single layer of sp^2-hybridized carbon atoms arranged in a honeycomb lattice [5], as shown in Figure 1.1a. Furthermore, graphene's conduction band minimum and valence band maximum meet at the Dirac points, as shown in Figure 1.1b, rendering graphene a zero band gap semiconductor [3]. One remarkable property of graphene is that when electrons interact with the periodic potential of the lattice, they behave, at low energies, as massless Dirac fermions moving at a speed 300 times slower than the speed of light, allowing for the study of novel quantum electrodynamics phenomena [3, 5]. Another salient property of graphene is its large, room-temperature charge carrier mobility of $\mu \approx 140{,}000\ \mathrm{cm}^2/\mathrm{V}\cdot\mathrm{s}$ [6]. Such large mobility means that ballistic transport is possible over micrometer ranges. One application of graphene's high mobility is the fast extraction of carriers in photodetectors [7, 8].

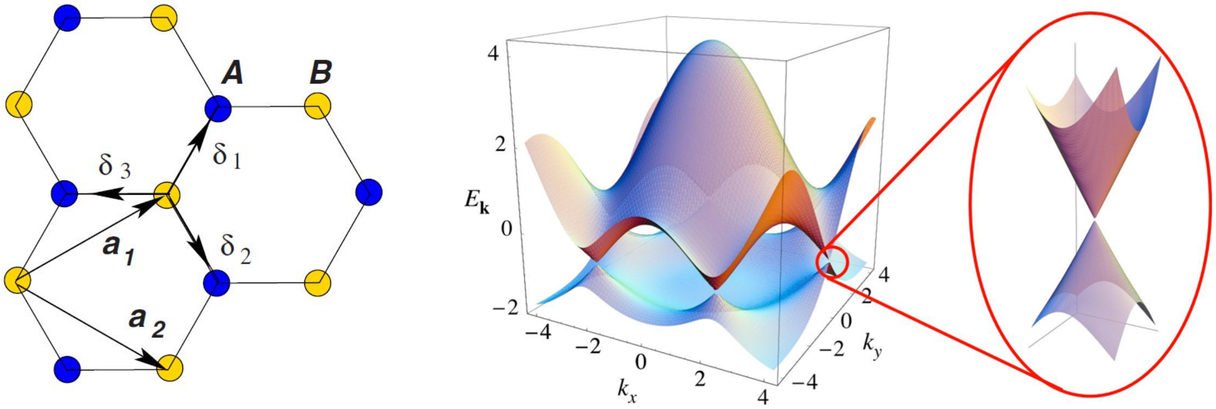

Figure 1.1: Left: Graphene crystal structure. A and B represent the two triangular sublattices. $\vec{a_1}$ and $\vec{a_2}$ are the primitive lattice vectors and $\vec{\delta_1}$, $\vec{\delta_2}$, $\vec{\delta_3}$ are the nearest neighbor vectors. Right: Graphene band structure. The conduction and valence band touch at the Dirac points. Images from Ref [5]

Although graphene possesses remarkable qualities, the absence of a band gap presents challenges in numerous optoelectronic applications [2]. Thus, the semiconductor industry relies on other layered semiconductors, such as the transition metal dichalcogenides (TMDs), to develop more efficient and versatile optoelectronic devices, such as photoemitters, photodetectors, and field-effect transistors [9, 10].

1.1.2 Transition Metal Dichalcogenides (TMDs)

Transition metal dichalcogenides (TMDs) have the chemical formula MX_2, where M is a transition metal (e.g. molybdenum, tungstem, halfnium) and X is a chalcogen (sulfur, selenium, or tellurium) [11]. Each layer has the sequence X-M-X, with each metal atom having a trigonal prismatic or octahedral coordination [9, 12–14]. There are about 60 TMDs with electronic properties ranging from insulating, semiconducting, semi-metallic, and metallic [9, 15, 16]. TMDs with a transition metal from groups IV-VII are predominantly layered [9]. Layered, semiconductor TMDs, such as MoS_2 and WS_2, are of great interest because they possess a non-zero band gap while also retaining the benefits of being a layered material, such as bonding anisotropy and pristine surfaces. These properties make layered, semiconductor TMDs promising materials for optoelectronic devices.

Due to their weak, var der Waals, interlayer boding, layered materials are prone to stacking faults, which may result in a layered material having different stacking sequences, or polytypes [13]. For example, TMDs are commonly found in three polytypes: 1T (trigonal symmetry, octahedral metal coordination), 2H (hexagonal symmetry, trigonal prismatic metal coordination), and 3R (rhombohedral symmetry, trigonal prismatic metal coordination) [9, 12]. The stacking sequence is important because it can influence the physical properties of a crystal. For example, Luo *et al.* reported that the transition temperature to superconductivity for the $TaSe_{2-x}Te_x$ alloy system changes as the addition of Te causes transitions among different polytypes [17].

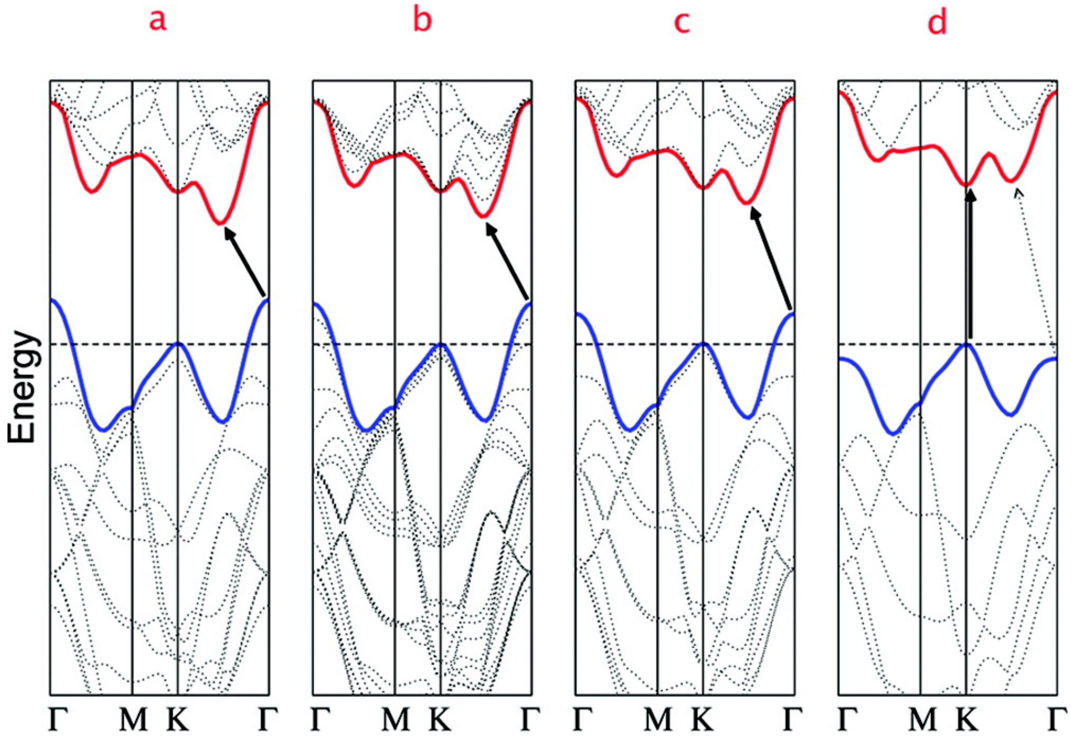

Figure 1.2: Calculated bandstructures of MoS_2 depicting the indirect to direct band gap transition as the number of layers, n, approaches 1. (a) n = bulk (b) n = 4 (c) n = 2 (d) n = 1. Image from Ref [18].

Another salient property of several TMDs is the transition from indirect to direct band gap in the monolayer regime. For example, MoS_2, in its bulk form, has an indirect band gap of 1.29 eV [19]. As the number of layers decreases, there is a downward energy shift at the Γ-point in the Brillouin zone due to quantum confinement, as shown in Fig 1.2 [14, 18, 19].

Consequently, the MoS_2 band gap transitions to a larger, direct band gap of 1.80 eV [19]. This transition results in its photoluminescence quantum yield increasing by 10^4 compared to its bulk form [19]. Other layered, semiconductor TMDs, such as $MoSe_2$, WS_2, and WSe_2, also undergo this indirect to direct band gap transition and band gap enlargement when transitioning from bulk to monolayer form [20, 21].

TMDs have many applications in optoelectronic devices. For example, TMDs have short radiative lifetimes due to their high excitonic binding energy (≈ 0.6 eV in bulk), which could have applications in high modulation bandwidth light emitters [10]. Another application of TMDs that has been studied extensively due to the visible range of their band gaps is photodetection. For instance, phototransistors fabricated from $MoSe_2$ exfoliated layers, WS_2 films grown by CVD, and WSe_2 monolayers grown by CVD have been reported to have fast response times, high photoresponsitivity and stability [22–24]. In the case of MoS_2, ultresensitive photodetectors with photoresponsivity of $880\,\mathrm{A\,W^{-1}}$ and phototransistors with thickness-modulated energy gap have been reported as well [25, 26].

1.1.3 Gallium Monochalcogenide Family

The gallium monochalcogenide family is composed of the group III-VI binary compounds gallium sulfide (GaS), gallium selenide (GaSe), and gallium telluride (GaTe). Each layer has the atomic sequence X-M-M-X, where M is the metal gallium and X is the chalcogen sulfur, selenium, or tellurium. The different polytypes of GaS and GaSe are shown in Fig 1.3. Similar to other layered materials, the gallium monochalcogenide family possesses a strong structural anisotropy in which interlayer bonding consists of weak, van deer Waals bonds and intralayer bonding consists of strong, covalent-ionic bonds.

In this section, the structural and optical properties of each gallium monochalcogenide are discussed in more depth, with an emphasis on the optical properties of GaS, in order to lay the foundation for the sulfur-rich $GaS_{1-x}Te_x$ alloy system discussed in Chapter 2.

1.1.3.1 Gallium Sulfide

Gallium Sulfide is an n-type, layered semiconductor. It has a hexagonal crystal structure with each layer being composed of four atoms, S-Ga-Ga-S, stacked along the c-axis, and with each unit cell containing two layers [27, 28]. GaS has lattice parameters $a = 0.359$ nm and $c = 1.549$ nm [27]. The thermodynamically stable polytype of GaS is the hexagonal β stacking phase with space group $P6_3/mmc$ [27].

Several studies have reported on the interband transitions of GaS. Aulich *et al.* first established the indirect nature of β-GaS's band gap by measuring optical absorption at 77 K [29]. The indirect band gap was reported to be 2.59 eV and the direct band gap was reported to be 3.05 eV [29]. Ho *et al.* also reported on the interband transitions of β-GaS in the range of 15 K to 300 K through optical absorption and piezoreflectance (PzR) [30]. The indirect

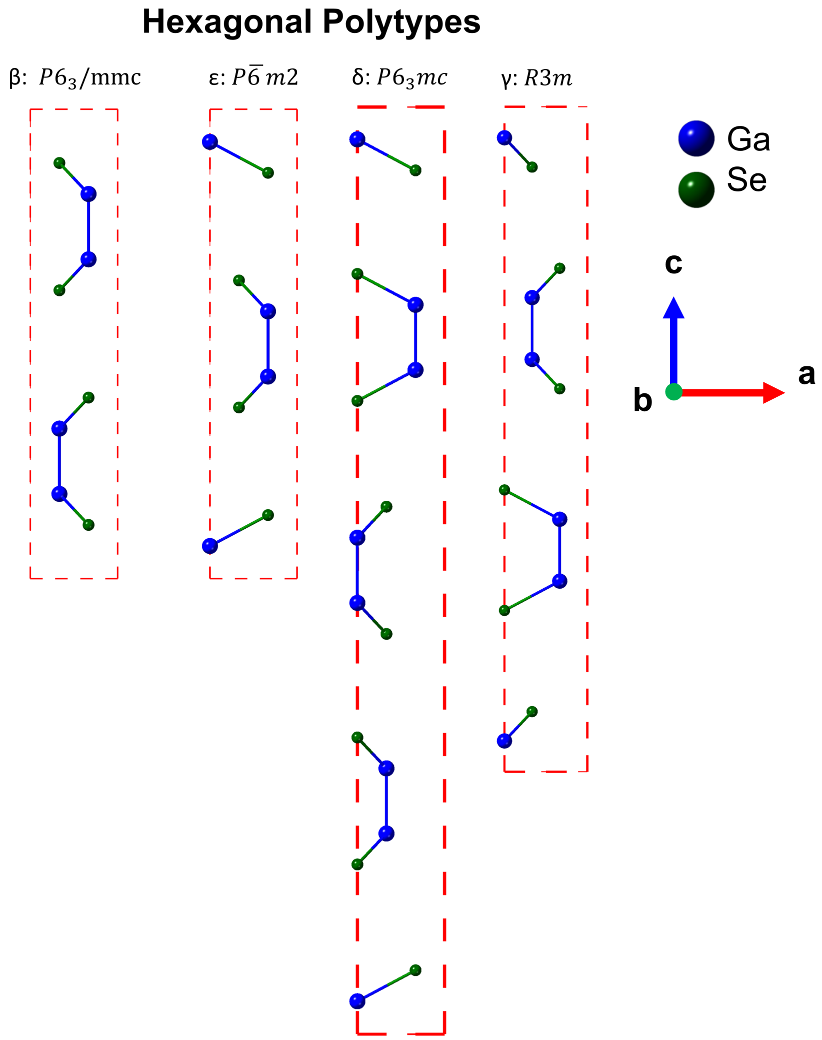

Figure 1.3: Side view of the unit cells for the different GaSe hexagonal polytypes: β, ϵ, δ, and γ. The unit cells were generated using the software Crystal Maker and the lattice parameters and Wyckoff positions were obtained from the Materials Project database.

band gap of GaS was reported to be 2.53 eV at 300 K and the direct band gap was reported to be 3.05 eV at 15 K, in agreement with the values reported by Aulich *et al.* From these two studies, the indirect and direct band gap energies of β-GaS are well established.

In addition to studies using optical absorption and PzR, there are several reports on the interband transitions of GaS from luminescence excitation. Springford *et al.* first measured variable temperature luminescence of GaS plates [31]. The luminescence showed broad peaks near 1.91 eV and 1.65 eV at 65 K and 1.43 eV and 1.65 eV at 133 K [31]. The origin of these transitions was unclear from this study. Cingolani *et al.* reported photoluminescence (PL) measurements at 77 K of GaS crystals grown by an iodine transport method. The PL spectrum had three peaks located at 2.89 eV, 2.59 eV, and 2.15 eV [32]. The first two peaks were attributed to the direct and indirect transitions of GaS, and the third peak at 2.15 eV was attributed to iodine impurities from the crystal growth [32]. Catalano *et al.* also reported on the variable temperature luminescence of GaS crystals grown by the Bridgman technique. It was reported that at 4 K, there were four peaks located at 2.561 eV, 2.516 eV, 2.455 eV, and 2.407 eV and a broad band centered at 2.12 eV [33]. The peak at 2.561 eV was tentatively attributed to a bound indirect exciton with binding energy of $\approx$ 10 meV. The other peaks were thought to be phonon replicas of the 2.561 eV peak [33]. Finally, Aydinli *et al.* reported that at temperatures below 90 K, there were three peaks in the luminescence spectra of GaS at 2.22 eV, 2.02 eV, and 1.59 eV [27]. The peaks were attributed to deep acceptor and shallow donor levels from point defects, such as sulfur interstitials and gallium vacancies with different charge states [27].

In addition to reports on the luminescence of GaS bulk crystals, there are reports on the luminescence of GaS nanostructures. For example, Jin *et al.* reported on the photoluminescence of GaS nanowires, nanoclusters, and nanoparticles grown by the vapor-liquid-solid (VLS) growth mechanism [34]. The nanowires had a PL peak centered at around 2.00 eV (620nm), the nanoclusters had a high-intensity peak centered at 1.73 eV (715nm) and a low-intensity shoulder centered at 2.82 eV (440nm), and the nanoparticles had a broad, low -intensity peak centered at 1.73 eV (715 nm) [34]. The low-intensity shoulder centered at 2.82 eV from the nanoclusters was attributed to the direct band gap of GaS and the other transitions were attributed to donor-acceptor levels from sulfur interstitials, gallium vacancies, and stacking defects [34]. Sinha *et al.* also reported on the luminescence of GaS nanohorns grown by VLS [35]. The room-temperature, PL peaks were located at 2.74 eV (452nm) and 2.50 eV (495nm) and were attributed to structural defects, such as sulfur and gallium vacancies and staking defects, in the vicinity of the direct and indirect band gaps [35].

Overall, the luminescence studies of GaS highlighted in this section, and summarized in Table 1.1, show that the luminescence spectra vary widely depending on the impurities incorporated and structural defects formed during the synthesis process of the GaS crystals.

Form	**Exc.** (eV)	**T** (K)	**A** (eV)	**B** (eV)	**C** (eV)	**D** (eV)	**E** (eV)	**Ref**
Bulk crystal	UV	65 133	1.65 1.43, 1.65	1.91 –	–	–	–	*[31]
Bulk crystal	3.40	77	–	–	2.32	2.51	–	[36]
Bulk crystal	UV	77	1.62	2.17	–	2.55	–	[37]
Bulk crystal	3.54	77	–	2.15	–	2.59	2.89	[32]
Bulk crystal	3.40	4.2 77	–	2.12	–	2.57 –	–	*[33]
Bulk crystal	3.40	97	–	2.17	–	–	–	[38]
Bulk crystal	2.71	9 80 280	1.59 1.68 1.65	2.02 2.00 –	2.22 2.20 –	–	–	[27]
Flakes	3.68	77	1.67	2.14	2.20	2.61	–	*[39]
Bulk crystal	3.06	77	–	–	–	2.56, 2.57	–	[40]
Bulk crystal	3.82	RT	–	–	–	2.43	–	[41]
Nanotubes	>3.5	RT	–	2.12, 2.02	–	–	–	[42]
Bulk lamellar Nanotubes	3.82	77	–	–	–	2.53, 2.67 2.53	2.74, 2.88 2.74	*[43]
Nanohorns	3.54	RT	–	–	–	2.51	2.74	[35]
Nanowires Nanoclusters Nanoparticles	3.89	RT	– 1.73 1.73	2.00 – –	–	–	– 2.82 –	[34]
Nanosheets	3.89	8	–	–	–	2.54	–	[44]
Nanobelts	3.89	RT	–	–	–	2.53	–	[45]
Flakes	2.33	–	–	1.99	–	–	–	*[46]

Table 1.1: Summary of PL studies performed on different forms of GaS found in literature. Exc. is the excitation energy, T is the temperature of the measurement (RT is room temperature), and A-E are the different PL peaks observed in the studies. The studies are listed in chronological order, from oldest to newest.

*Ref [31] has an additional peak at 1.43 eV that's unique from all other reports.

*Ref [33] reported phonon replicas of the 2.57 eV peak at 2.544 eV, 2.536 eV, and 2.522 eV.

*Ref [8] peaks are for moderate excitation of $\approx 10^{17}$ photon/cm^2. At higher excitations, the PL spectrum had peaks at 1.89 eV, 2.00 eV, 2.13 eV, 2.25 eV, 2.30 eV, 2.40 eV, 2.57 eV, and 2.61 eV.

*Ref [43] is unclear in its wording whether nanotubes also exhibit a peak at 2.53 eV, but the PL spectrum appears to have a small shoulder at this energy.

*Ref [46] does not explicitly state the temperature of the PL measurement, but due to the broad shape of the peak, it is likely room temperature. Furthermore, the peak could be convoluted by two smaller peaks, but the study only states the energy of the maximum intensity.

Luminescence of GaS doped with various elements has been reported as well. Aono *et al.* reported on the undoped and Zn-doped luminescence of GaS crystals grown by an iodine transport method [38]. The reported luminescence of undoped GaS at 97 K had a peak at 2.17 eV. This peak was attributed to the transition between the iodine impurity donor and gallium vacancy acceptor from the growth process. Zn-doped GaS crystals showed a new PL peak at 2.47 eV attributed to a $[Zn^{-1} - I^{+1}]$ complex [38]. Finally, with the introduction of Zn into the GaS crystal, a broad shoulder emerged in the 1.60 eV to 2.10 eV region which was attributed to lattice defects. Chiricenco *et al.* reported on GaS single crystal films isolated from bulk crystals and doped with Cu through thermal diffusion [39]. At 78 K, the undoped GaS photoluminescence showed two broad shoulders with the first broad shoulder being composed of peaks at 2.40 eV, 2.30 eV, 2.25 eV, 2.13 eV (maximum intensity), 2.00 eV, and 1.89 eV. The second broad shoulder was composed of peaks at 2.57 eV and 2.61 eV [39]. The peaks at 2.57 eV and 2.61 eV were attributed to photonic replicas of indirect excitons while the peak with maximum intensity at 2.12 eV was attributed to recombination of conduction band electrons and holes from deep acceptor centers at 0.73 eV, 0.78 eV, 0.90 eV, 1.03 eV, and 1.15 eV from the valence band [39]. The PL from Cu-doped GaS had two peaks at 1.80 eV and 2.13 eV and were attributed to recombination via deep impurity levels. Shigetomi *et al.* reported on the photoluminescence of Mn, Zn, Cd, P, As, Ge, and Sn on GaS [40, 47–51]. All of the GaS crystal were grown by the Bridgman method and the PL was conducted at 77 K. The reported peaks in the PL were attributed to impurity levels and structural defects in the GaS crystals. Table 1.2 summarizes the results of these studies.

Dopant	**at%**	**PL Temp (K)**	**Undoped GaS PL Peak (eV)**	**Doped GaS PL peak (eV)**	**Ref**
Zn	8.27	97	2.17	broad band 1.6-21, 2.47	[38]
Zn	1.00	77	1.23	1.85	[47]
Cd	1.00	77	1.23	1.95	[47]
Cu	–	78	2.13, 2.57	1.80, 2.12 and 1.55, 2.30 shoulders	[39]
Mn	0.10	77	2.57, 2.56	2.00	[40]
P	0.10	77	1.23	2.12, 2.35	[48]
As	0.10	77	2.57, 2.56	2.08, 2.38	[49]
Ge	0.20	77	1.23	1.96, 2.30	[50]
Sn	0.20	77	1.23	broad peak 1.5-2.3	[51]

Table 1.2: Photoluminescence studies of doped GaS crystals with different impurity species. All the measurements were conducted at 77 K except for the first Zn (97 K) and Cu (78 K) studies.

1.1.3.2 Gallium Selenide

Gallium Selenide is a p-type semiconductor with different polytypes [52]. When grown by the Bridgman method, GaSe can exist as a mixture of the ϵ (space group $P\bar{6}m2$) and γ (space group $R3m$) polytypes due to glide stacking faults introduced by mechanical deformation [52]. GaSe can be synthesized in the β (space group $P6_3/mmc$) polytype as well [53–55]. From optical absorption measurements at 77 K, GaSe has been reported to have an indirect band gap of 2.065 eV for the ϵ and γ stacking phases and 2.117 eV for the β stacking phase, and a direct band gap of 2.120 eV for ϵ and γ stacking phases and 2.169 eV for the β stacking phase [29].

In addition to optical absorption, the photoluminescence of GaSe has been studied as well. For example, Cingolani *et al.* reported that the emission spectrum of GaSe at 77 K had a broad peak between 2.10 eV and 2.13 eV that was attributed to the direct band gap transition and a fine structure with peaks at 2.084 eV, 2.083 eV, 2.082 eV, and 2.080 eV attributed to the splitting of the excitonic ground level from the presence of $\epsilon + \gamma$ phases [32]. The luminescence of doped GaSe with Sn, Cu, Zn, I, and Cd has been studied as well [56, 57]. It was reported that the spectra did not depend on the type of dopant added to the crystal but only on the concentration of the dopant in the crystal. This observation was explained by the presence of shallow defect states originating from intrinsic structural defects, such as glide stacking faults in GaSe, and extrinsic structural defects caused by the high concentration of dopants [56]. More recently, Shigetomi *et al.* reported on the photoluminescence at 77 K of GaSe crystals grown by the Bridgman method and doped with Ag in the range of 0.02-0.5 at% [58]. For undoped GaSe, the PL spectra had peaks at 2.10 eV and 2.03 eV attributed to the direct free exciton recombination and the indirect free exciton radiative decay, respectively. For Ag-doped GaSe, two additional peaks emerged at 2.02 eV and 1.74 eV. The peak at 2.02 eV was attributed to the recombination of bound excitons or to the conduction band to shallow acceptor transition. The peak at 1.74 eV was attributed to the impurity level localized within the band gap.

1.1.3.3 Gallium Telluride

Bulk GaTe is a p-type semiconductor [59]. Optical absorption measurements showed a direct band gap of 1.78 eV at 4.2 K and 1.65 eV at 300 K [60]. Furthermore, GaTe has an indirect, forbidden energy gap of 1.55 eV at room-temperature [61]. Its thermodynamically stable crystal structure is monoclinic, with two different Ga-Ga configurations: one third parallel to the layer, and two thirds perpendicular to the layer [62, 63]. GaTe has space group $C2/m$ with lattice parameters $a = 1.74\,\mathrm{nm}$, $b = 0.41\,\mathrm{nm}$, $c = 1.05\,\mathrm{nm}$, $\beta = 104.44°$ [64–66].

The luminescence of GaTe has also been reported. Pozo-Zamudio *et al.* reported that at 10 K, the PL of GaTe had a peak at 1.75 eV, which is consistent with the optical absorption measurement by Brebner *et al.* previously described [67]. GaTe did not possess a transition from direct to indirect band gap in the few layer regime.

GaTe also has a metastable hexagonal phase. The band gap of this phase has been reported, but there isn't a clear consensus on the band gap energy. Gillan *et al.*, Cai *et al.*, and Fonseca *et al.* have reported values for hexagonal GaTe of 1.75 eV to 1.90 eV, 1.44 eV, 1.03 eV, respectively [64, 68, 69]. Additionally, Zhao *et al.* showed that GaTe undergoes a transition from monoclinic to hexagonal phase in the few layer regime [70]. The lattice parameters of the few-layer, hexagonal GaTe were reported to be $a = b = 0.41\,\text{nm}$ and $c = 1.70\,\text{nm}$. This transition was also observed by Bae *et al.* in GaTe films grown by molecular beam epitaxy [71].

Finally, GaTe has been shown to be sensitive to oxygen chemisorption under ambient conditions [72, 73]. The band structure of GaTe has been reported to undergo a transformation from pristine GaTe direct gap of 1.65 eV to an aged GaTe narrow gap below 0.80 eV [72].

1.1.3.4 Gallium Monochalcogenide Applications

All three binary compounds in the gallium monochalcogenide family have been shown to have applications in optoelectronic devices. For example, exfoliated GaS nanosheets have been used to fabricate flexible photodetectors with superior photoresponsivity than graphene and MoS_2 and superior external quantum yield than graphene at 254 nm [74]. Rigid and flexible photodetectors fabricated with GaSe obtained from mechanical exfoliation, vapor phase deposition, and van deer Waals epitaxy have also shown promising response times and responsivities [75–77]. Furthermore, due to its p-type nature, GaSe has been shown to form vertically stacked and lateral heterojunctions with $MoSe_2$, an n-type material [78]. These p-n junctions showed effective transport and charge carrier separation, making them promising structures for gate-tunable photodetectors [78]. GaTe is also a desirable candidate for next-generation optoelectronic devices due to its direct band gap. For example, GaTe nanosheets grown by CVD have been fabricated into flexible photodetectors with excellent responsivities [63, 79]. Table 1.3 shows the superiority of the gallium monochalcogenide family for important photodetector parameters relative to other common layered materials.

Material	**Spectral Range**	**Responsivity** $(\mathrm{A\,W^{-1}})$	**Response time** (ms)
Graphene	Vis IR	0.01	1.5×10^{-8}
monolayer MoS_2	Vis	880	4000
multilayer MoS_2	UV-IR	0.1	–
multilayer WS_2	Vis	92×10^{-6}	5
multilayer GaS	UV-Vis	4.2	30
multilayer GaSe	UV-Vis	2.8	20
multilayer GaTe	Vis	10^4	6

Table 1.3: Summary of photodetector parameters for common layered materials. Table adapted from Ref [74, 79].

1.2 Layered Nanowires, Nanoribbons, and Nanobelts

1D nanostructures are single crystals that allow for the study of the effects of morphology, dimensionality, size, and composition on physical properties, and thus are key to understand and engineer new materials [80, 81]. In this section, the advantages of using nanostructures to study alloying effects, particularly between dissimilar materials, are discussed. Furthermore, a brief overview of the growth mechanisms and morphologies of nanostructures synthesized from layered materials is given, with an emphasis on GaS, GaSe, and GeS nanostructures.

1D nanostructures, such as nanowires, nanoribbons, and nanobelts, are typically confined to less than 100 nm in their lateral dimension [80]. A particular advantage of the reduced dimension of nanowires is their ability to accommodate stress through lateral relaxation [82]. Ertekin *et al.* reported on the critical radius of a nanowire heterostructure at which misfit dislocations start forming to accommodate the strain from the lattice mismatch [82]. The critical radius was reported to be an order of magnitude larger than the critical thickness for a film of the same materials. From this work, it is implied that nanowires could be better material systems than bulk crystals and thin films to study mismatched materials due to this enhanced stress-relaxation ability.

A widely used nanowire growth mechanism is the vapor-liquid-solid (VLS) growth mechanism first developed by Wagner and Ellis in 1964 [83]. In this growth mechanism, a metal catalyst droplet is used to provide a low surface energy, absorption site for the incoming gas phase reactant. Subsequently, the gas phase reactant incorporates into the metal catalyst droplet until the droplet supersaturates with the gas phase reactant and the single-crystal nanowire precipitates and grows at the solid-liquid interface [84].

The role of the metal catalyst is extremely important in the initialization of nanowire growth and in determining the morphology and size of nanowires grown through the VLS growth mechanism [85]. The requirements of a metal catalyst should be: it must form a liquid alloy with the growth species; its solubility in the liquid phase must be higher than in the solid phase of the growth species; its vapor pressure should be smaller than the vapor pressure of the liquid alloy formed with the growth species; and it must be chemically inert [86, 87]. Typical choices of metal catalyst include gold, silver, nickel, and iron [85, 87, 88].

The VLS growth mechanism has been used to synthesize nanowires from layered materials. For example, Peng *et al.* synthesized GaSe nanobelts with different morphologies (i.e. straight, zig-zag, and saw-toothed nanobelts) by changing the catalyst's size and composition (i.e. changing among pure gold, gallium and gold alloy, and pure gallium catalyst compositions) [89]. Control over the catalyst size and composition was achieved by varying the growth temperature and time [89]. Other examples of nanostructures grown by the VLS growth mechanism are GaS nanohorns, nanobelts, and nanowires, as shown in Fig 1.4 [34, 35, 90, 91]. Furthermore, it is also possible to use the VLS growth mechanism to synthesize alloy nanowires. For instance, Pan *et al.* synthesized CdS_xSe_{1-x} "sword-like" nanobelts across the entire composition range using a gold-catalyzed VLS method [92].

In recent years, a new type of layered nanowires whose growth direction is parallel to the c-axis have been reported. For example, Sutter *et al.* synthesized c-axis GeS and β-GaS nanowires by using gold and silver catalyzed VLS growth, respectively [88]. In the case of β-GaS, the nanowires were composed of alternating, truncated triangular stacks with an overall tapered morphology, as shown in Figure 1.4f. The authors attributed this difference in morphology from previous GaS nanostructures to the wetting angle of the Ag-Ga catalyst droplet, the vapor species, and the behavior of the liquidus in the Ag-Ga phase diagram [88]. In general, because the wetting angle is smaller when the basal plane of the nanowire is in contact with the catalyst droplet, the nanowire basal plane size follows more closely the size of the catalyst. Furthermore, the reactant gas supplies GaS and Ga gas species to the catalyst, causing the catalyst to grow with the absorption of Ga. These changes in catalyst composition result in changes in catalyst size, melting temperature, and solubility, and are responsible for the c-axis GaS nanowire morphology. Layered GeS has also been reported to grow as a helically twisted nanowire along the c-axis, as shown in Figure 1.4h [93, 94]. It was reported that the Eshelby twist drives the twisted morphology of these nanowires grown by gold-catalyzed VLS method. These new types of layered nanowires offer exciting opportunities to tune material properties by controlling the growth direction and the degree of twisting of the layered nanowires.

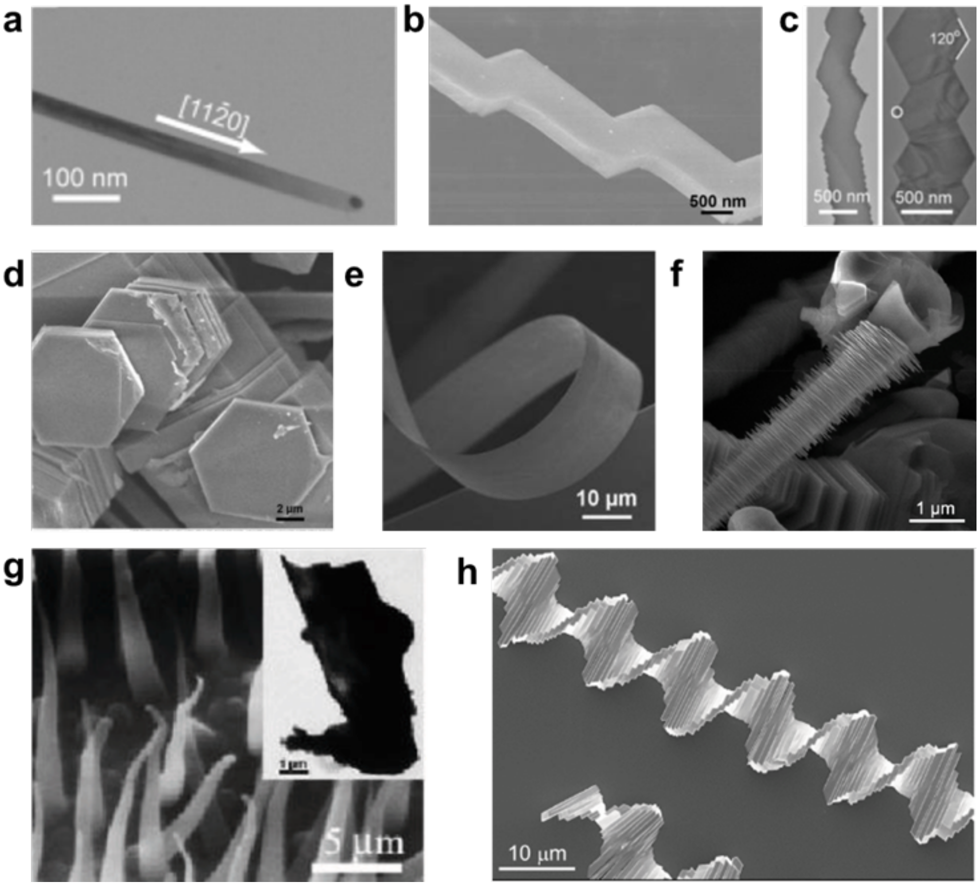

Figure 1.4: Examples from literature of different layered nanostructure morphologies grown by the vapor-liquid-solid growth (a, c, f-h) and vapor-solid growth mechanisms (b, d, and e). (a) GaSe straight nanowire [89]. (b) GaS zig-zag nanobelt [91]. (c) GaSe sawtooth nanobelt [89]. (d) GaS microbelts [91]. (e) GaS nanobelt [91]. (f) GaS twinned, c-axis nanowire [88]. (g) GaS nanohorns [35]. (h) GeS helical nanowire [93].

1.3 Band Engineering Through Alloying

As highlighted in previous sections of this chapter, the band gaps of layered semiconductor compounds span a wide range of energies, with applications in photodetectors, photovoltaics, and nanoelectronics [10, 14]. However, it is desirable from an engineering standpoint to achieve a higher control of the tunability of band gap energies for two reasons: 1) to tailor material properties for specific applications with a higher degree of precision, and 2) to extend the range of band gap energies currently available. One way to achieve this band engineering is through alloying. Alloying components allows for the controlled tuning of a material property as a function of composition and may also give rise to novel properties beyond the properties of its constituents. In this section, the basic principles of alloying are discussed, with a focus on the gallium monochalcogenide alloys.

When synthesizing a binary, metallic alloy, the Hume-Rothery rules serve as a starting point to assess the solubility limit of an element into a metal [95]. These rules state that solubility can be limited if the atomic size between the solute and the solvent is greater than 15%, there is a large difference in electronegativity between the solute and the solvent, and the solvent valency is lower than the solute. Similarly, for ternary semiconductor alloys, when the structural and chemical properties of the alloy constituents are well-matched, the alloy properties, such as lattice parameters and band gap, tend to follow a linear relationship with alloy composition between the end-point materials. In this case, the virtual crystal approximation (VCA) can be used to describe the electronic band structure of the disordered alloy system [96]. Furthermore, if an alloy's property, such as the lattice parameter, has a linear relationship with composition, Vegard's law can be used to interpolate the values of that property between its end-points. Using these principles, several studies have focused on synthesizing TMD alloys.

Initially, the $MoS_{2(1-x)}Se_{2x}$ alloy system was calculated to be thermodynamically stable at room-temperature and possess full band gap tunability [97]. Since then, several experimental reports have confirmed the stability and synthesis of TMD alloys, primarily $MoS_{2(1-x)}Se_{2x}$, $MoSe_{2(1-x)}Te_{2x}$, $WS_{2(1-x)}Se_{2x}$, $WSe_{2(1-x)}Te_{2x}$, $Mo_{1-x}W_xS_2$, and $Mo_{1-x}W_xSe_2$ through CVD and exfoliation with full band gap tunability [98–110]. Overall, TMD alloys have shown to have potential applications in optoelectronics, such as photodectectors and solar cell thin-films [98].

1.3.1 Gallium Monochalcogenide Alloys

1.3.1.1 $GaSe_{1-x}S_x$

Gallium monochalcogenide alloy systems are ideal to study the role of varying crystal structures and polytypes on the optoelectronic and structural properties of the alloy system. In particular, the $GaSe_{1-x}S_x$ alloy system has been studied extensively due to the complete miscibility between GaS and GaSe. For example, Aulich *et al.* reported on the synthesis of $GaSe_{1-x}S_x$ alloy crystals grown by the Bridgman technique across the entire composition range [29]. In this study, it was reported that the alloy system had three different phase regions. In the first region, $0 \leq x \leq 0.1$, the ϵ and γ stacking phases were present. In the second region, $0.2 \leq x \leq 0.4$, all stacking phases $(\epsilon, \gamma, \beta)$ were present. In the third region, $0.6 \leq x \leq 1$, the β stacking phase was present.

Interestingly, the polytypes present in the alloy system are not only influenced by composition but by the growth technique and growth conditions as well. For example, Arancia *et al.* reported on the optical and structural properties of $GaSe_{1-x}S_x$ alloys grown by the Bridgman and iodine vapor transport techniques [111]. The lattice parameters were different based on the growth technique employed. Furthermore, the c lattice parameter changed abruptly as the crystals transitioned from the ϵ, γ stacking phase to the β stacking phase with increasing sulfur composition. The composition at which this transition occurred was dependent on the growth technique as well. For the Bridgman technique, the transition happened at $x = 0.45$ while for iodine vapor transport technique it occurred at $x = 0.25$. In a study by Cardetta *et al.*, the iodine vapor transport technique was proposed to involve a growth mechanism by screw dislocations [112]. Consequently, it was hypothesized that the iodine vapor transport growth technique allows for the coexistance of $\epsilon + \beta$ stacking phases below $x = 0.25$. This result was confirmed by Terhell *et al.* with the study of $\mathrm{GaSe}_{1-x}\mathrm{S}_x$ crystals grown by iodine vapor transport and characterized through X-ray diffraction [113]. In that study, the region of $\epsilon + \beta$ mixed phases was found to be $0.15 \leq x \leq 0.35$.

In addition to its structural properties, the interband transitions of the $\mathrm{GaSe}_{1-x}\mathrm{S}_x$ alloy system have been studied as well. For instance, Ho *et al.* reported on the room-temperature interband transitions of $\mathrm{GaSe}_{1-x}\mathrm{S}_x$ alloy crystals grown by the Bridgman technique across the entire composition range [41, 114, 115]. As in previous studies, the presence of different stacking phases depended on the composition of the crystal, with compositions $x \leq 0.10$ having an ϵ stacking phase, and intermdediate compositions having a mixed $\epsilon + \beta$ stacking phases. The indirect band gap for β-GaS was estimated from PzR to be 2.53 eV. The direct band gap was calculated to be 2.86 eV. Furthermore, the PL was reported to have a peak at 2.40 eV, which was attributed to a donor defect level from the ϵ stacking fault within the β-GaS crystal. The overall band gap dependence with composition was linear.

The optical and structural properties of $\mathrm{GaSe}_{1-x}\mathrm{S}_x$ alloy nanostructures have also been reported. Jung *et al.* synthesized monolayers and multilayers of $\mathrm{GaSe}_{1-x}\mathrm{S}_x$ alloys through chemical vapor transport [44]. This growth technique yielded β-GaS, β-GaSe, γ-GaSe (grown at lower temperatures), and a mixture of $\beta + \gamma$ stacking phases for the alloys. The band gap dependence with composition was linear, as shown in Figure 1.5a. From cathodoluminescence (CL) measurements, it was observed that, as the number of layers decreased, the band gap of GaS and GaSe increased. However, unlike some common TMDs, GaS and GaSe did not show a cross over from indirect to direct band gap in the monolayer regime. A possible explanation for the increased luminescence emission in GaS was attributed to the adsorption of oxygen, just as oxygen had enhanced the PL emission of n-type MoS_2 [116]. It was proposed that O_2 chemisorption in sulfur-rich β-GaS is more favorable than in β-or γ-GaSe because β-GaS compensates for electrostatic interlayer repulsion by increasing interlayer distance compared to γ-GaSe, and oxygen binds more strongly to sulfur compared to selenium [45]. Due to the oxygen chemisorption, the direct and indirect band gaps of GaS converge.

1.3.1.2 $\mathrm{GaSe}_{1-x}\mathrm{Te}_x$

The $\mathrm{GaSe}_{1-x}\mathrm{Te}_x$ alloy system presents new synthesis challenges as well as opportunities for novel technological applications, compared to the $\mathrm{GaSe}_{1-x}\mathrm{S}_x$ alloy system, due to the dissimilar crystal structure of the constituent compounds. For example, Camassel *et al.* reported on the synthesis and optical properties of bulk $GaSe_{1-x}Te_x$ alloy crystals grown by Bridgman technique [117]. That study reported bulk alloy crystals with different crystal structures in two compositional regions: hexagonal crystals in the $0 \leq x \leq 0.30$ region and monoclinic crystals in the $0.65 \leq x \leq 1.00$ region. However, there were no bulk crystal alloys synthesized in the intermediate compositions of $0.30 < x < 0.65$, as predicted by the phase diagram of this alloy system [117].

Fonseca *et al.* reported the synthesis of single-phase, macro and nanostructures of the $GaSe_{1-x}Te_x$ alloy across the entire composition range [68]. It was reported that monoclinic crystals were present in the range $0 \leq x \leq 0.28$; monoclinic and hexagonal crystals were present in $0.28 \leq x \leq 0.32$; and hexagonal crystals were present in $0.32 \leq x \leq 1.00$, as shown in Figure 1.5b. The morphology was indicative of the underlying crystal structure with monoclinic crystals having a triangular morphology and hexagonal crystals having a zig-zag and serrated morphology. The behavior of the band gap followed a linear relationship with composition for monoclinic crystals and for hexagonal crystals with a high selenium composition. However, for hexagonal crystals with low selenium composition, the band gap displayed a shallow band bowing. Cai *et al.* simultaneously confirmed the mixed-phase region and the shallow band bowing of the $GaSe_{1-x}Te_x$ alloy system [69]. It is important to highlight that synthesis of macro and nanostructures allowed for crystals to be alloyed across the entire composition range, as opposed to the limited range synthesized by Camassel *et al.*

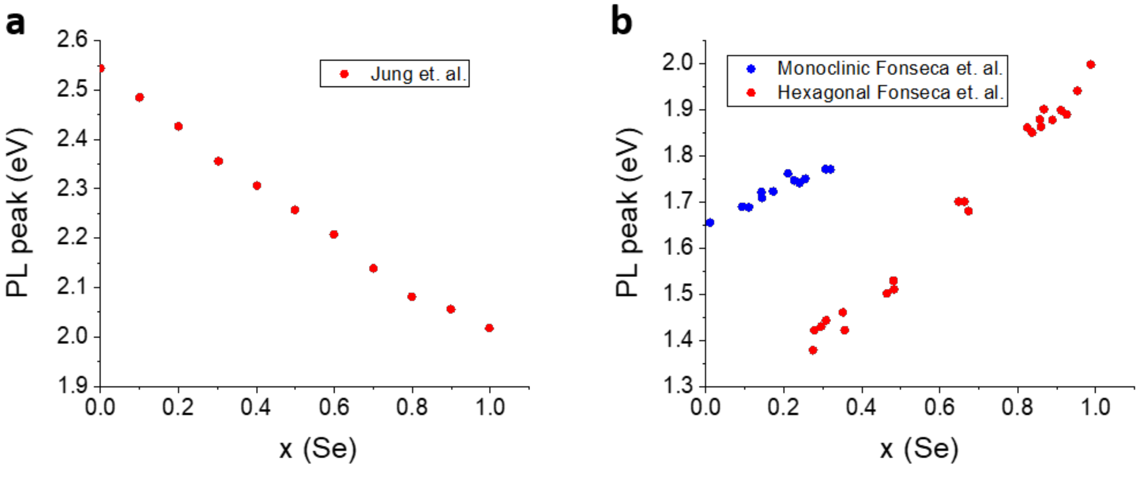

Figure 1.5: (a) PL peaks versus selenium composition for $GaSe_{1-x}S_x$ alloy crystals [44]. (b) PL peaks versus selenium composition for $GaSe_{1-x}Te_x$ alloy crystals [68].

1.3.2 Highly Mismatched Alloys

Highly mismatched alloys (HMAs) are alloys whose constituent elements have large differences in electronegativity, atomic radius and ionization energy. Due to these differences in chemical properties, the band gap has a non-linear relation with composition, as shown in Figure 1.6. The degree of non-linearity is described by a bowing parameter. One advantage of highly mismatched alloys is that the range of band gap energies accessible could be larger than the range of the constituent compounds. Another advantage of highly mismatched alloys is that a lower fraction of alloying is needed to tune the properties of a material due to the drastic changes in band gap from the non-linear behavior.

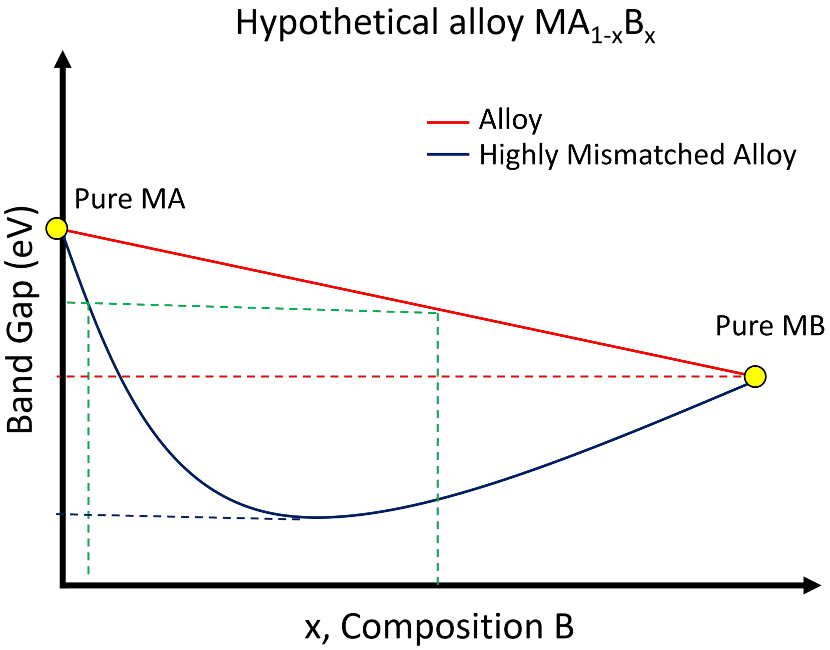

Figure 1.6: Schematic of the band gap dependency over composition for two cases of a hypothetical alloy $MA_{1-x}B_x$. In the first case, the alloy is well matched and the band gap follows a linear relationship with composition. In the second case, the alloy is highly mismatched, and the band gap has a non-linear relationship with composition.

Examples of HMAs include $ZnTe_{1-x}S_x$, $ZnTe_{1-x}Se_x$, $GaAs_{1-x}Sb_x$, $ZnO_{1-x}S_x$ [118–120]. However, the most extreme example of band bowing is the $GaAs_{1-x}N_x$ alloy system [121]. For this alloy system, luminescence studies showed that the PL peaks drastically decreased in energy with increasing nitrogen composition. For example, with the addition of 1% N, the band gap decreased by 180 meV [121]. This drastic decrease in the band gap was explained in the framework of the band anti-crossing model by Wu *et al.* [122]. In this model, the nitrogen forms an impurity band that hybridizes with the conduction band and splits into an E_+ and

E_- energy bands, as shown in Figure 1.7. HMAs are promising materials because property tuning can be achieved through small changes in composition and because properties beyond the initial endpoints can be accessed.

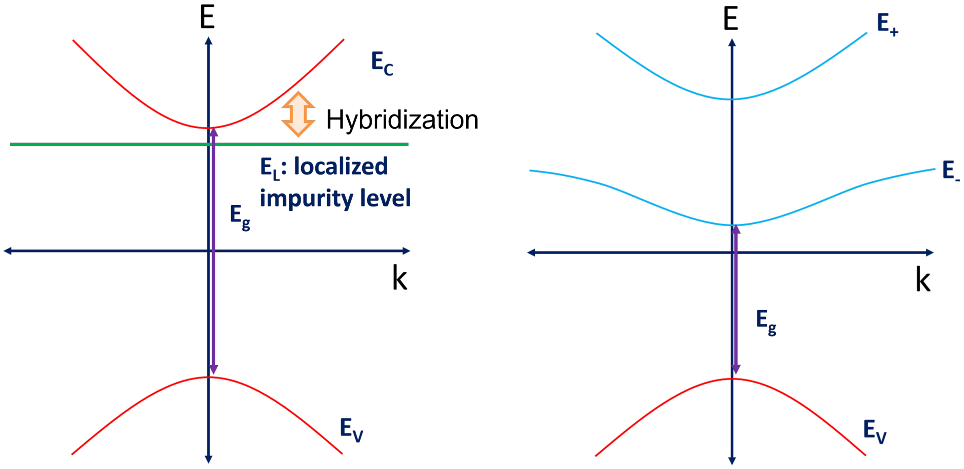

Figure 1.7: Schematic of the E-k diagrams for a direct band gap semiconductor when (a) the impurity level is formed close to the conduction band, E_c and when (b) the impurity level hybridizes with the conduction band and the E_- and E_+ bands form.

1.4 Scope of this Dissertation

In this chapter, the importance of layered materials, such as graphene, transition metal dichalcogenides, and the gallium monochalcogenide family was discussed. Emphasis was given to the structural and optical properties of these materials and their applications in optoelectronic devices, such as photodetectors. Furthermore, the need for alloying as a band engineering tool and the advantages of using nanostructures to study mismatched alloys were highlighted. The rest of this dissertation will focus on the sulfur-rich $GaS_{1-x}Te_x$ nanostructures grown along the c-axis by a gold-catalyzed, vapor-liquid-solid growth mechanism. The interplay between morphology, crystal structure, and composition will be explored in Chapter 2. In Chapter 3, the optical properties of the alloy crystals are explored through photoluminescence and cathodoluminescence spectroscopy and a band model is proposed to reconcile the PL and CL data. In Chapter 4, DFT calculations are presented to further elucidate on the experimental data presented in Chapter 3. Finally, in Chapter 5, the significance of this work will be discussed as well as the future direction of this project.

Chapter 2

$\mathrm{GaS}_{1-x}\mathrm{Te}_x$ Alloy Nanostructures

As discussed in Chapter 1, layered materials possess many desirable properties for optoelectronic applications. In particular, the gallium monochalcogenide family has been shown to have applications in photodetector technology, such as flexible photodetectors [63, 74, 75, 123]. Furthermore, two alloy systems of the gallium monochalcogenide family–that is, the $\mathrm{GaSe}_{1-x}\mathrm{S}_x$ [29, 36, 37, 41, 44, 45, 124] and $\mathrm{GaSe}_{1-x}\mathrm{Te}_x$ [68, 69, 117]–have been reported to possess a unique opportunity to study the interplay of structure and composition due to the different crystal structures and polytypes among the GaS, GaSe, and GaTe binary compounds. However, the $\mathrm{GaS}_{1-x}\mathrm{Te}_x$ alloy system has not been studied before due to the expected miscibility gap. In this work, the $\mathrm{GaS}_{1-x}\mathrm{Te}_x$ nanostructures are synthesized using a gold-catalyzed, vapor transport method. Nanostructures were synthesized to better accommodate stress through lateral relaxation, compared to bulk crystals. The synsthesis of $\mathrm{GaS}_{1-x}\mathrm{Te}_x$ presents new opportunities to study the synthesis of mismatched, layered semiconductors and their crystal structure, growth direction, and optoelectronic properties.

In this chapter, a description of the alloy nanostructure synthesis and transfer process is given in Section 2.1. Then, in Sections 2.2 and 2.3, the morphology, size, growth direction, and growth mechanisms for GaS nanobelts and $\mathrm{GaS}_{1-x}\mathrm{Te}_x$ alloy nanowires, respectively, are discussed. Finally, a summary of the results presented in this chapter is given in Section 2.4.

2.1 Nanostructure Synthesis

In this work, $\mathrm{GaS}_{1-x}\mathrm{Te}_x$ nanostructures were synthesized using a gold-catalyzed, vapor transport method. The substrate used for the growth was a silicon chip (p-type, $< 100 >$ orientation) with dimensions 7 mm by 15 mm. The substrate preparation consisted of three steps. First, the substrate was sonicated in isopropyl alcohol (IPA) for 15 minutes to remove debris from the cleavage process. Second, after drying the substrate with nitrogen gas, the substrate was cleaned in oxygen plasma for five minutes to remove hybrocarbons from the surface. Finally, 5 nm of gold were deposited on the substrate using e-beam evaporation at a rate of 0.5 Å s^{-1}.

The source materials for the growth were 50 mg of gallium sulfide and 50 mg of gallium telluride powders (American Elements, 99.999% purity). For the synthesis of alloy nanowires, the powders were placed in separate cylindrical alumina crucibles (crucible dimensions: height = 12 mm, outer diameter = 8 mm). For the synthesis of GaS nanobelts, only GaS powder was used. The substrate and crucibles were placed inside a cylindrical, quartz furnace tube (furnace dimensions: length = 600 mm, inner diameter = 20.5 mm) and the tube was loaded into a single-zone furnace (Lindberg/Blue M furnace) as shown in Figure 2.1.

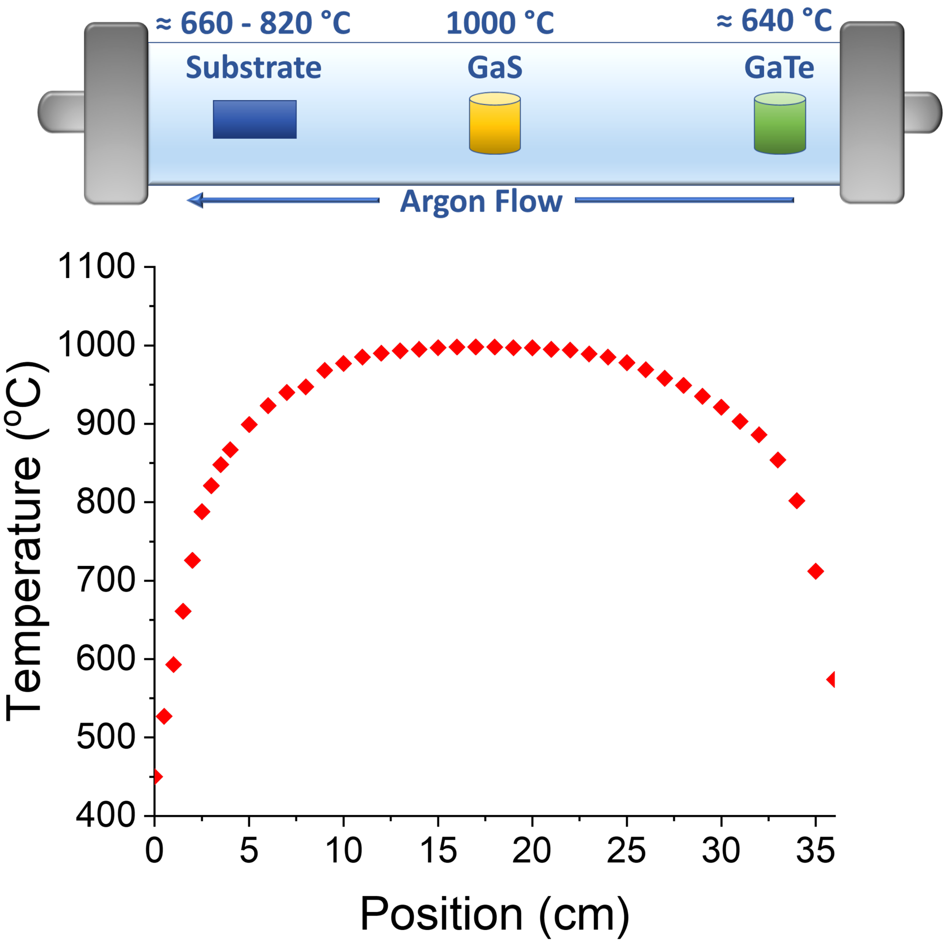

Figure 2.1: Schematic of the experimental set up for an alloy growth with nominal composition of $x = 0.10$ (i.e. GaS$_{0.90}$Te$_{0.10}$). For growths with other compositions, the temperature of the GaTe powder was changed by moving the crucible position along the temperature gradient of the furnace.

The nanostructure growth recipe consisted of three steps. In the first step, the furnace was heated to 70 °C and the furnace tube was flushed with argon gas (Praxair, 99.999% purity) at 200 sccm for 30 min to remove water vapor. In the second step, the furnace temperature was raised to the target temperature for GaS evaporation and the gas flow was reduced to 100 sccm. Once the temperature reached steady state, the nanostructures were allowed to grow for 30 min. In the last step, the furnace was gradually cooled down to room-temperature with a gas flow of 10 sccm for several hours. The gas was decreased to a minimal flow to prevent back flow from the potassium hydroxide neutralizing solution at the outflow of the furnace system and to minimize nanowire growth by decreasing transport of the source powders to the substrate. The furnace tube was kept at atmospheric pressure during all steps.

It is important to describe the set up of the furnace in greater detail in order to understand the experimental limitations of this work. The furnace used in this work has one heating zone that is 350 mm in length. In this case, a single heating zone means that the temperature of the furnace coils are set by one controller. This is different from a multi-zone furnace, in which there are separate, independently controlled sets of heating coils for each zone. Furthermore, the temperature along the single heating zone is not uniform. The temperature profile of the heating zone with a set temperature of 1000 °C and measured with a thermocouple is shown in Figure 2.1. There is a 50 mm interval at the center of the heating zone where the temperature is uniform and it is the same as the set temperature of the controller. Outside of this 50 mm interval, the temperature of the heating zone slowly starts to decrease. Towards the edges of the heating zone, the temperature decays very rapidly. Based on this set up, the temperatures of the substrate and the source materials are determined by their positions along the heating zone of the furnace, and not by independent heating zones. Therefore, to obtain different alloy compositions across different growths, the position of the GaTe powder was moved along the furnace heating zone while the positions of the substrate and GaS powder were fixed.

Although several growths were attempted to synthesize alloy nanowires with different tellurium compositions, the heating zone's limited temperature range along its gradient and the drastic temperature variability near the edges of the heating zone presented experimental challenges to achieving compositional control, morphological control, and reproducibility. Consequently, this dissertation will focus on selected growths that yielded a high number of alloy nanowires with their fast-growth direction parallel to the c-axis and with the following morphological criteria: continuously straight edges parallel to the fast-growth direction of the nanowire (i.e. the c-axis of the nanowire), sharp termination for surface planes perpendicular to the c-axis of the nanowire, and a hexagonal cross-section, as shown in Figure 2.8. For an overview of the diversity of nanowire morphologies observed from all the growths conducted, see Appendix G. Finally, in Chapter 5, the advantages of using a three-zone furnace, which is currently being set up in our laboratory, to explore the full experimental parameter space will be discussed in more detail.

Figure 2.2 shows an SEM image of an as-grown, alloy growth with nominal composition of $x = 0.10$. The nominal compositions of the alloy nanowires were obtained from EDS measurements as shown in Appendix A. This growth yielded the highest density of c-axis alloy nanowires that meet the morphological criteria described above. The as-grown nanowires are randomly oriented with respect to the substrate and span tens of microns in length. The density of the as-grown nanowires in this growth is higher than the density of the as-grown, GaS nanowires reported by Sutter *et al.* in a similar VLS experimental set up [88]. Although most alloy nanowires exhibited a nominal composition of $x = 0.10$, the compositional range for alloy nanowires observed in this growth is $0.05 \leq x \leq 0.13$. Finally, the growth temperature of the substrate was 660 °C at the cooler edge and 820 °C at the hotter edge while the temperatures of the GaS and GaTe powders were 1000 °C and 640 °C, respectively. These temperatures were chosen based on the thermal decomposition temperatures reported for gallium monochalcogenides [125].

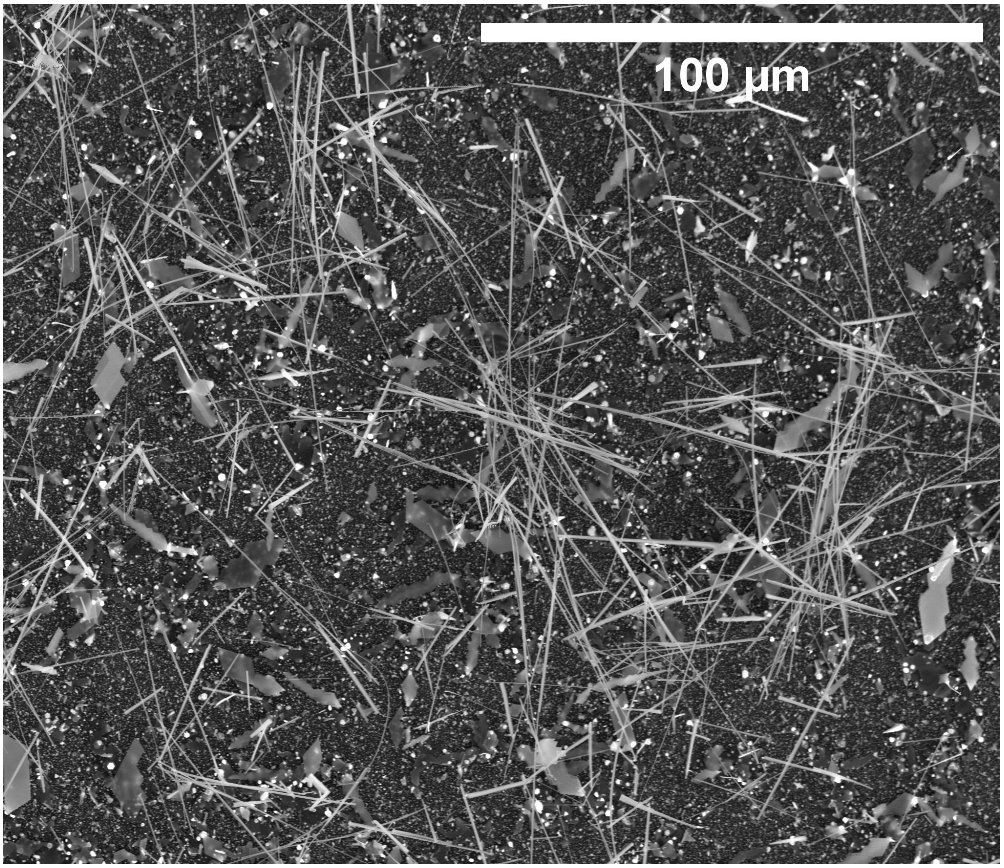

Figure 2.2: SEM image of alloy growth with nominal composition of $x = 0.10$ (i.e. $GaS_{0.90}Te_{0.10}$).

Finally, the nanostructures were mechanically transferred to a handle substrate for characterization. Two types of handle substrates were used in this work. The first type is a SiO_2-on-Si chip patterned with enumerated gold markers to aid in locating nanowires. This substrate was used to perform SEM, EDS, micro-Raman, micro-photoluminescence, and cathodoluminescence. The second type of handle substrate is a SiN TEM grid used to perform TEM analysis. The mechanical transfer process consisted of manually aligning the surfaces of the as-grown substrate and handle substrate and applying pressure to transfer wires. This facile method was efficient in transferring a large number of wires to the handle substrate.

2.2 Gallium Sulfide Nanobelts

2.2.1 GaS Nanobelt Morphology

Gallium sulfide nanobelts (GaS NBs) have a straight or ziz-zag morphology, as shown in Figure 2.3a and b, respectively. The zig-zag angle is 120°, typical of hexagonal GaSe and GaS nanobelts reported in literature [89, 91]. GaS NBs may also display sawtooth faceting along the sides parallel to the fast-growth direction of the nanobelt. The sawtooth faceting can be on both sides of the nanobelt (symmetric sawtooth faceting) or only on one side of the nanobelt (asymmetric sawtooth faceting). Finally, sawtooth faceting may be present in both straight and zig-zag morphologies. For example, straight nanobelts with asymmetric sawtooth faceting and zig-zag nanobelts with symmetric sawtooth faceting were observed, as shown in 2.3c and d, respectively.

GaS NBs are tens of microns in length and hundreds of nanometers in width. A typical thickness for a GaS nanobelt is 50 nm, as seen in the AFM line scan in Fig 2.4. The reported thickness of a GaS monolayer is 0.75 nm with a Ga-Ga bond length of 2.48 Å and a Ga-S bond length of 2.37 Å [126]. Therefore, the GaS NB shown in Fig 2.4 is composed of about 200 layers. Furthermore, the AFM line scan in Fig 2.4b shows that a GaS NB has a rectangular cross section. Finally, energy dispersive x-ray spectroscopy (EDS) analysis confirms that that the composition of the GaS nanobelts is stoichiometric.

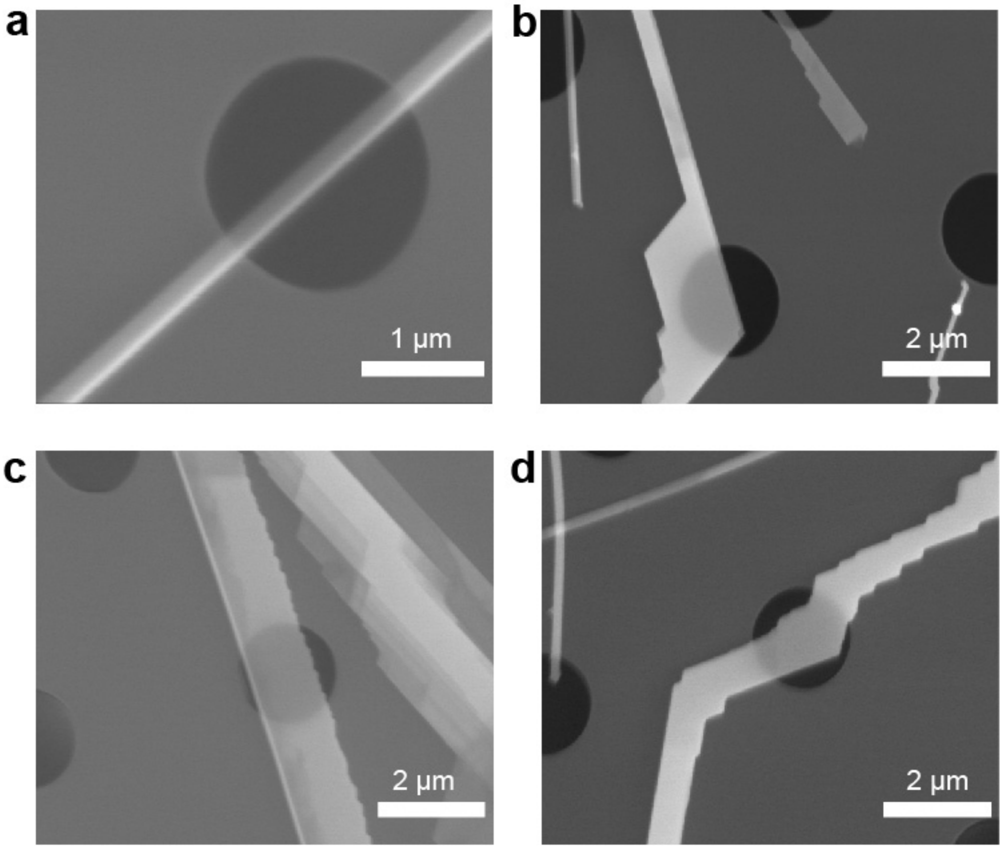

Figure 2.3: SEM images of GaS nanobelts with different morphologies transferred to a SiN grid: (a) straight nanobelt, (b) zig-zag nanobelt, (c) straight, asymmetric sawtooth nanobelt, and (d) zig-zag, symmetric sawtooth nanobelt.

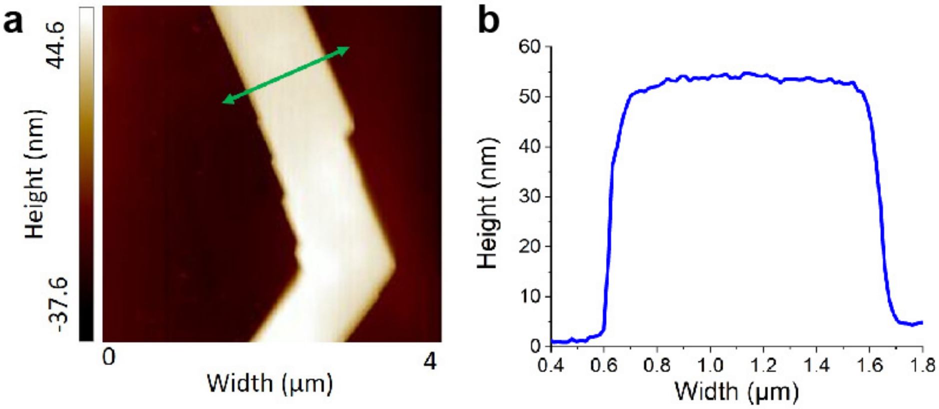

Figure 2.4: (a) AFM image of a zig-zag GaS nanobelt. (b) AFM line scan of the ziz-zag GaS nanobelt shown in (a) and indicated by the green line.

2.2.2 GaS Nanobelt Crystal Structure

The crystal structure and growth direction of GaS nanobelts were studied by TEM. GaS NBs were mechanically transferred to a SiN TEM grid, as shown in Figure 2.5a. The higher-resolution image in Figure 2.5b shows that there is a thin later of material covering the edge of the GaS nanobelt. EDS measurements did not distinguish a compositional difference between the nanobelt and this thin layer. Two possibilities for the composition of this thin layer are oxygen passivation or amorphous deposition during the cool down step of the growth. The selected-area electron diffraction (SAED) in Figure 2.5c shows that the GaS NB are single crystalline. The diffraction pattern was indexed as the [001] zone axis of the hexagonal crystal system with space group $P6_3/mmc$ (β-GaS). Therefore, the growth direction of GaS NBs is perpendicular to the $\{001\}$ family of planes. The lattice constant a for this GaS nanobelt was calculated to be $a = 3.512\,\text{Å}$, which is 2% smaller than the GaS lattice constant a reported in literature ($a = 3.585\,\text{Å}$) [127].

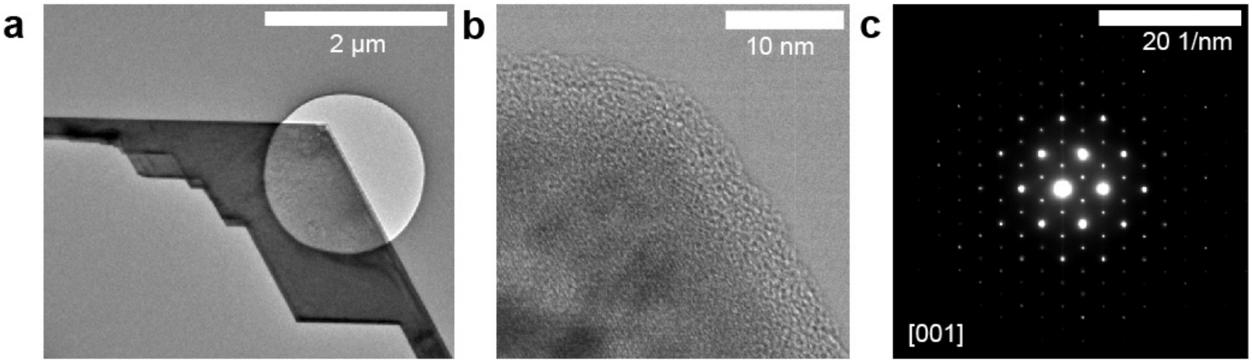

Figure 2.5: TEM characterization of a GaS nanobelt. (a) Low-magnification TEM image of GaS nanobelt (b) High-resolution TEM image of nanobelt in (a). (c) Selected-area electron diffraction pattern from nanobelt in (a) indexed for a hexagonal crystal structure. TEM performed by Dr. Shaul Aloni.

Room-temperature, micro-Raman spectroscopy was performed to assess the crystal quality of the GaS NBs. The experimental set up consisted of a 488nm laser as the excitation source, a silicon-based CCD as the detector, and a 2400 gr/mm grating. GaS has six non-degenerate, Raman-active modes [128]. Four Raman-active modes are shear modes with wavenumbers at $22\,\text{cm}^{-1}$, $75\,\text{cm}^{-1}$, $291\,\text{cm}^{-1}$, and $295\,\text{cm}^{-1}$, and two are compression modes with wavenumbers $188\,\text{cm}^{-1}$ and $360\,\text{cm}^{-1}$ as shown in Figure 2.6 [28, 128–130]. The three highest-intensity peaks in the Raman spectra of GaS are the two compression modes, A^1_{1g} and A^2_{1g}, and the E^1_{2g} shear mode at $188\,\text{cm}^{-1}$, $360\,\text{cm}^{-1}$, and $291\,\text{cm}^{-1}$, respectively. The Raman spectrum of the transferred GaS NB shown in Figure 2.6 has intense and narrow peaks at $189\,\text{cm}^{-1}$ and $360\,\text{cm}^{-1}$, indicating that the GaS NB possesses high crystal quality. Furthermore, the Raman spectrum of the transferred GaS NB agrees well with the Raman spectrum of GaS bulk crystals reported in literature [28]. Therefore, the peaks in Figure

2.6 are assigned to the following modes: $A^1_{1g} = 188.9\,\mathrm{cm}^{-1}$, $A^2_{1g} = 359.9\,\mathrm{cm}^{-1}$, and $E^2_{1g} = 291.9\,\mathrm{cm}^{-1}$.

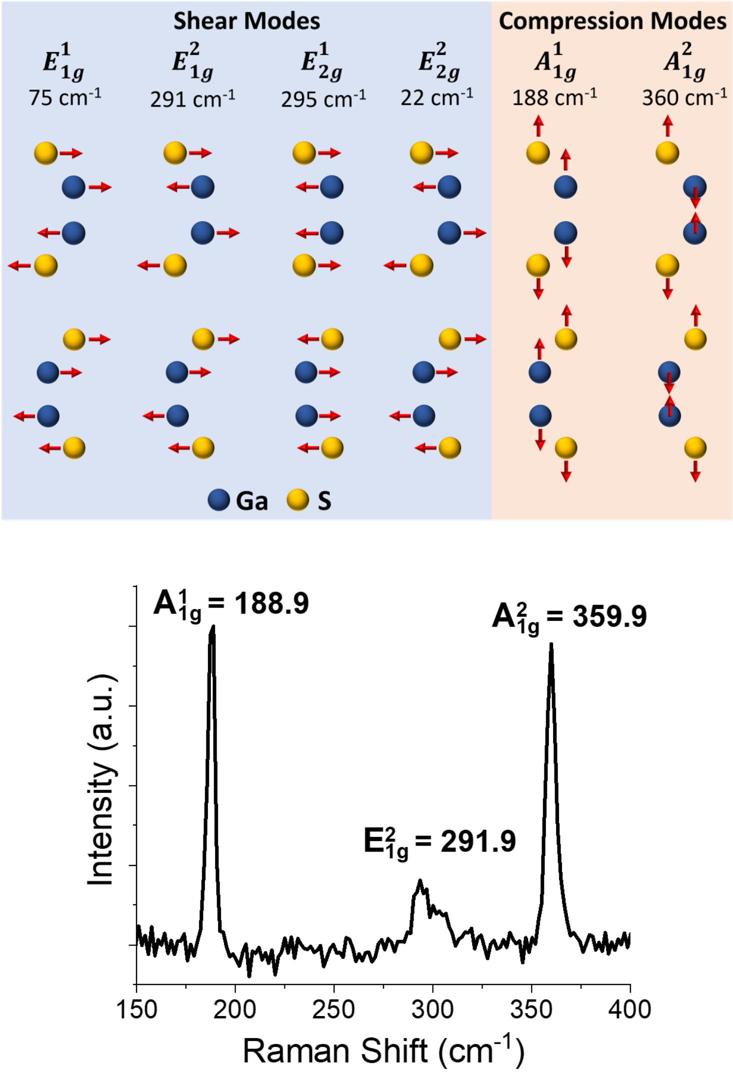

Figure 2.6: Raman spectroscopy of a GaS nanobelt. Top: Schematic of Raman-active modes in GaS. Figure adapted from Ref [28]. Bottom: Room-temperature, micro-Raman spectra of a GaS nanobelt measured with a 488 nm laser line.

2.2.3 Growth Mechanism of GaS Nanobelts

Similar to the GaSe nanowires reported by Peng *et al.* [89], the growth mechanisms leading to the formation of GaS nanobelts are a combination of vapor-liquid-solid (VLS) and vapor-solid-solid (VSS) growth mechanisms, with VLS being the dominant growth mechanism. Evidence of the VLS growth mechanism leading to nanobelt formation is the presence of a small droplet at the end of the nanobelt, as shown in Figure 2.7. Note that the small size of this droplet, as well as charging effects during EDS measurements, presented challenges in determining its chemical composition. However, based on its spherical morphology and its higher brightness compared to the GaS nanobelt, it is likely that this droplet is a metal catalyst. Further characterization of droplets found at the ends of GaS nanobelts will need to be conducted to determine their composition. Additionally, the large ratio of length to width of the nanobelt serves as evidence that VLS is the dominant growth mechanism. Evidence of the VSS growth mechanism contributing to the growth of GaS nanobelts is the larger nanobelt width compared to the droplet diameter found at the end of the nanowire. The contribution of the VSS growth mechanism to the formation of the GaS nanobelt is consistent with the growth of layered nanowires because dangling bonds at the two edges parallel to the fast-growth direction facilitate the incorporation of atoms from the vapor phase and from the surfaces through diffusion [89]. Finally, the origin of the ziz-zag morphology is attributed to perturbations to the catalyst droplet, such as substrate temperature, catalyst composition, and gas flow, as in the case of GaSe nanowires reported by Peng *et al.* [89].

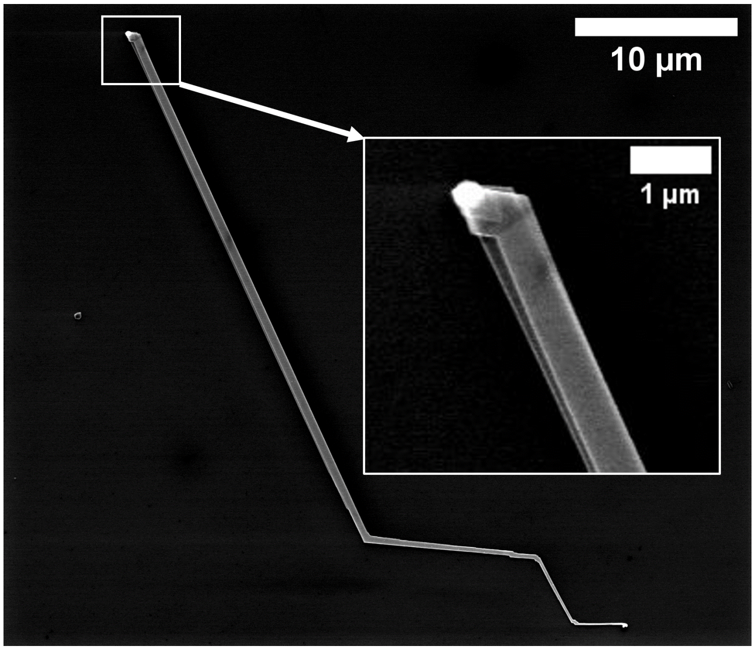

Figure 2.7: SEM image of a GaS nanobelt showing what appears to be a catalyst droplet at the end of the GaS nanobelt.

For the case of sawtooth facets, there are two mechanisms that explain the symmetric and asymmetric nature of sawtooth facets. In the case of asymmetric sawtooth facets, the origin is likely the alternating planes of opposite charged ions stacked along the c-axis that result in negatively and positively charged polar surfaces, depending on the species terminating the surface [131]. The resulting dipole moment perpendicular to the surface of the crystal causes the surface energy to diverge [132]. The sawtooth facets are then a compensation mechanism for the electrostatic charge on the surface [131]. In the asymmetric sawtooth GaS nanobelt, the straight side of the nanobelt is likely terminated with the more stable sulfur atoms and the sawtooth side of the nanobelt is likely terminated with the more reactive gallium atoms. This mechanism has been observed in ionic crystal nanowires, such as ZnO, ZnS, and CdSe nanowires [131, 133, 134]. In the case of symmetric sawtooth faceting, the origin is likely explained by the oscillatory surface energy force balance between the wire and the catalyst droplet [135]. In other words, as the facet of the nanowire grows wider, the catalyst droplet's contact angle decreases, driving an inward force to favor the narrowing facet, and vice-versa [135]. This symmetric sawtooth faceting has been observed in Si nanowires as well [135].

2.3 Sulfur-rich, GaS$_{1-x}$Te$_x$ Alloy Nanowires

2.3.1 Alloy Nanowire Morphology

The sulfur-rich (i.e. $x \leq 0.13$), GaS$_{1-x}$Te$_x$ alloy nanowires selected in this work possess three morphological criteria. The first criterion is that the nanowire edges parallel to the fast-growth direction (i.e. parallel to the c-axis) are continuously straight (i.e. no ziz-zag morphology or sawtooth faceting), as shown in Figure 2.8a. The second criterion is that the surface planes perpendicular to the fast-growth direction of the nanowires are sharply terminated, as show in Figure 2.8a and b. The third criterion is that, unlike GaS nanobelts which have a rectangular cross-section, alloy nanowires have a hexagonal cross-section, as shown in Figure 2.8b. The hexagonal cross-section can be confirmed by taking a tilted SEM image and through AFM measurements, as shown in Figure 2.8c and d. It is important to note that in the AFM line scan, the short sides of the hexagonal cross-section are 40 nm, which is about twenty times shorter than the long sides. Consequently, the large ratio of the length of the long side to the length of the short side creates a quasi-triangular cross-section in the SEM image. Alloy nanowires that meet these three criteria span tens of microns in length and range 400 nm to 1000 nm in width. In this work, the length of an alloy nanowire is defined as the length parallel to the fast-growth direction and the width of an alloy nanowire is defined as the length of one of the long sides of the hexagonal cross-section.

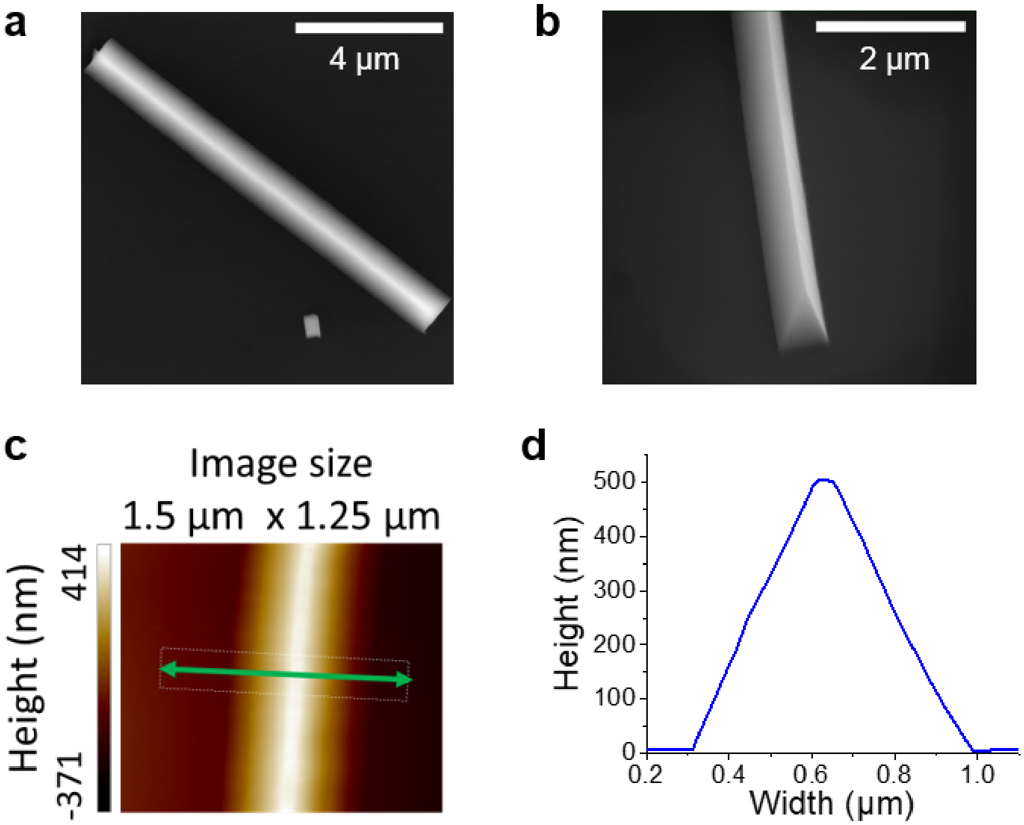

Figure 2.8: Alloy nanowire morphology. (a) SEM image of alloy nanowire with composition $x = 0.11$. (b) SEM image of alloy nanowire with composition $x = 0.10$ tilted by 52°. (c) AFM image of alloy nanowire with composition $x = 0.13$. (d) AFM line scan of alloy nanowire shown in (c) by a green line.

2.3.2 Alloy Nanowire Crystal Structure

The crystal structure and growth direction of alloy nanowires were studied by TEM. Alloy nanowires were mechanically transferred to a SiN TEM grid. The electron diffraction pattern in Figure 2.9a shows that the alloy nanowire is single crystalline. The diffraction pattern was indexed as the [210] zone axis of the hexagonal crystal system and therefore its growth direction is parallel to the {001} family of planes. Note that TEM measurement and indexing of the diffraction pattern shown in Figure 2.9a were performed by former graduate student James Chavez. A detailed description of James Chavez's indexing methodology is outlined in his master's thesis. The lattice parameters of a different alloy nanowire with similar nominal composition of $x = 0.11$ were also calculated by James Chavez to be $a = 3.65$ Å and $c = 15.80$ Å. These lattice parameters show a 1.78% and 1.9% expansion of the a and c lattice parameters of GaS reported in literature, respectively [127]. This is consistent with the larger atomic radius of Te (140 pm) compared to S (100 pm). Similar to GaS nanobelts, the higher-resolution image in Figure 2.9b shows that there is a thin later of material covering the edge of the alloy nanowire. EDS measurements did not distinguish a compositional difference between the alloy nanowire and this thin layer. Two possibilities for the composition of this thin layer are oxygen passivation or amorphous deposition during the cool down step of the growth. Finally, EDS shows that Ga, S, and Te are randomly and homogeneously distributed throughout the nanowire, as shown in 2.9c.

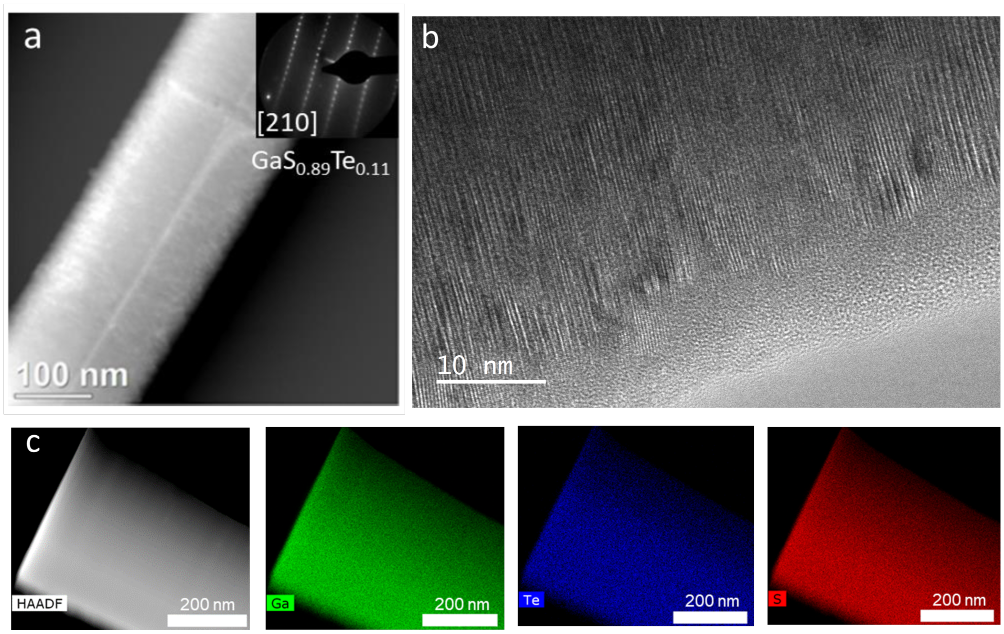

Figure 2.9: Crystal structure and composition of alloy nanowires. Alloy nanowires were transferred to a SiN TEM grid and Si handle substrates to perform TEM and EDS, respectively. (a) STEM image and diffraction pattern of an alloy nanowire with nominal composition of $x = 0.11$. STEM measurements and indexing were performed by James Chavez. (b) High-resolution TEM image of alloy nanowire with nominal composition of $x = 0.09$. TEM images were performed in collaboration with Dr. Shaul Aloni. (d) HAADF and EDS maps of alloy nanowire with composition $x = 0.10$. HAADF and EDS measurements were performed in collaboration with Dr. Petra Specht.

2.3.2.1 Kinematic Simulations of GaS Polytypes

Analyzing TEM diffraction patterns of alloy systems presents challenges because diffraction features could have multiple origins, such as stacking faults and insterstitials. Although simulating the diffraction pattern from an alloy would be ideal to inform about the nature of the experimentally observed diffraction pattern, these simulations would require sophisticated computational methods. Nevertheless, important information can still be obtained from basic simulation software. In this section, simulations were conducted with the software Crystal Maker for the two different GaS polytypes, ϵ and β, to establish a reference for future TEM measurements.

The two GaS polytype models are built using Crystal Maker with the parameters outlined in Appendix B. For the β-GaS polytype, the Wyckoff positions and lattice parameters are obtained from the Crystallography Open Database (COD), Reference [127]. However, for the ϵ-GaS polytype, the crystallographic information is not available from COD at the time this dissertation is written. Therefore, two assumptions are made to construct the ϵ-GaS polytype based on the analogous nature between GaS and GaSe crystal structures and the similar atomic radii of sulfur and selenium. The first assumption is that the lattice parameters for the ϵ-GaS polytype are the same as the β-GaS polytype lattice parameters. This assumptions is based on the lattice parameters of ϵ-and β-GaSe being the same to within two significant figures [136]. The second assumption is that the Wyckoff positions for the ϵ-GaS polytype are the same as the Wyckoff positions for the ϵ-GaSe polytype. This assumption is based on the Wyoff positions of β-GaS and β-GaSe are the same within two significant figures as well [127].

The crystal models and simulated TEM diffraction patterns are shown in Figure 2.10 and 2.11. Figure 2.10 shows the crystal models viewed from the [001] direction. In this view direction, the β-GaS crystal model shows the sulfur atoms positioned on top of the gallium atoms. In the ϵ-GaS crystal model, the sulfur atoms appear positioned at the center of the gallium hexagon. Despite these differences, the simulated TEM diffraction pattern shows that the two polytypes have identical diffraction patterns. For the [100] view direction shown in Figure 2.11, the atoms in the unit cell have more prominent differences in positions between the two polytypes, resulting in the simulated TEM diffraction pattern of the ϵ polytype having additional diffraction spots.

As expected, the TEM diffraction pattern in Figure 2.9 does not completely match either of the simulated diffraction patterns. This is because the simulated diffraction patterns are for a perfect, GaS crystal. Tellurium incorporation into the pristine GaS matrix will cause an expansion of the lattice constants due to the larger tellurium atoms, resulting in a different spacing for the diffraction spots. Furthermore, tellurium will likely introduce stacking faults into the system to accommodate the larger tellurium atoms. Consequently, the crystal structure might resemble more a mixture of an ϵ stacking phase within a β phase matrix. Therefore, it is important to highlight the differences in the diffraction patterns between the two polytypes in order to distinguish the subtleties that might arise in the experimental data.

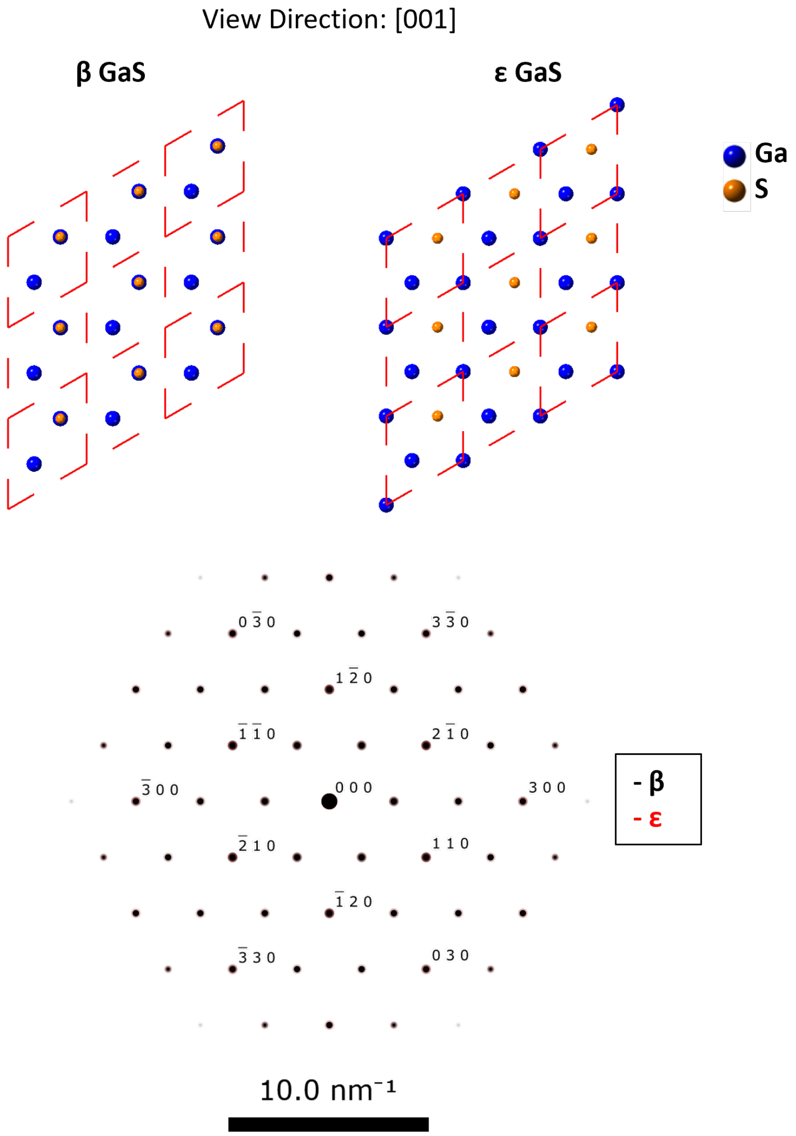

Figure 2.10: Models of the crystal structure for the β-and ϵ-GaS polytypes as viewed from the [001] direction. The red lines delineate the crystal's unit cell. The simulated, TEM diffraction pattern of the β-GaS polytype is overlayed on top of the simulated, TEM diffraction pattern of the ϵ-GaS polytype.

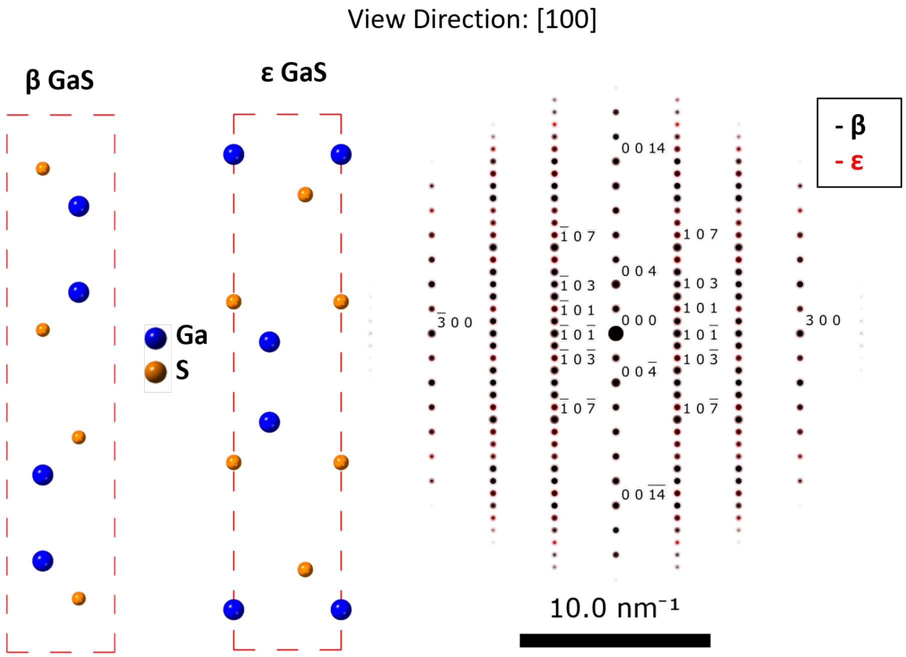

Figure 2.11: Models of the crystal structures for the β-and ϵ-GaS polytypes as viewed from the [100] direction. The red lines delineate the crystal's unit cell. The simulated, TEM diffraction pattern of the β-GaS polytype is overlayed on top of the simulated, TEM diffraction pattern of the ϵ-GaS polytype.

2.3.3 Raman Spectroscopy

Room-temperature, micro-Raman spectroscopy was performed with a 488 nm laser line to assess the crystal quality of the alloy nanowires and to obtain further structural information. The three GaS Raman-active modes, $A^1_{1g} = 188\,\mathrm{cm}^{-1}$, $A^2_{1g} = 360\,\mathrm{cm}^{-1}$, and $E^2_{1g} = 291\,\mathrm{cm}^{-1}$, were analyzed as a function of composition to observe changes in phonon vibrations with tellurium incorporation.

Figure 2.12a shows the Raman spectra of alloy nanowires with compositions $x = 0$ to 0.13. The three GaS Raman-active modes are indicated by the dashed, vertical lines. With the addition of tellurium, the intensity of the A^2_{1g} mode decreased relative to the intensity of the A^1_{1g} mode. Furthermore, all three GaS Raman modes red shifted with the addition of tellurium. Finally, mode A^1_{1g} split into two modes for $x > 0.04$, as shown in Figure 2.12b. The splitting of Raman peaks has been observed before for the GaS$_{1-x}$Se$_x$ alloy system [137, 138]. In the case of GaS$_{0.5}$Se$_{0.5}$ alloy crystals, the A^1_{1g} compression mode split into four modes. Gasanly *et al.* described the two outer peaks to be related to the stretching vibrations in GaSe and GaS binary compounds and attributed the intermediate peaks to the β and ϵ stacking phases of the alloy [137]. Specifically, the four modes were explained in the context of the cell isodisplacement model in which each cell type, Se-Ga-Ga-Se, S-Ga-Ga-S, and Se-Ga-Ga-S, can be identified with a different set of vibrations [137]. In the case of the mixed cell, Se-Ga-Ga-S, it has different vibrations depending on the stacking sequence. Therefore, it is possible that for the alloy nanowires in this work, the splitting of the A^1_{1g} mode into two modes is due to the presence of S-Ga-Ga-S and S-Ga-Ga-Te domains within the crystal, or to the different stacking sequence, β or ϵ, within each cell configuration.

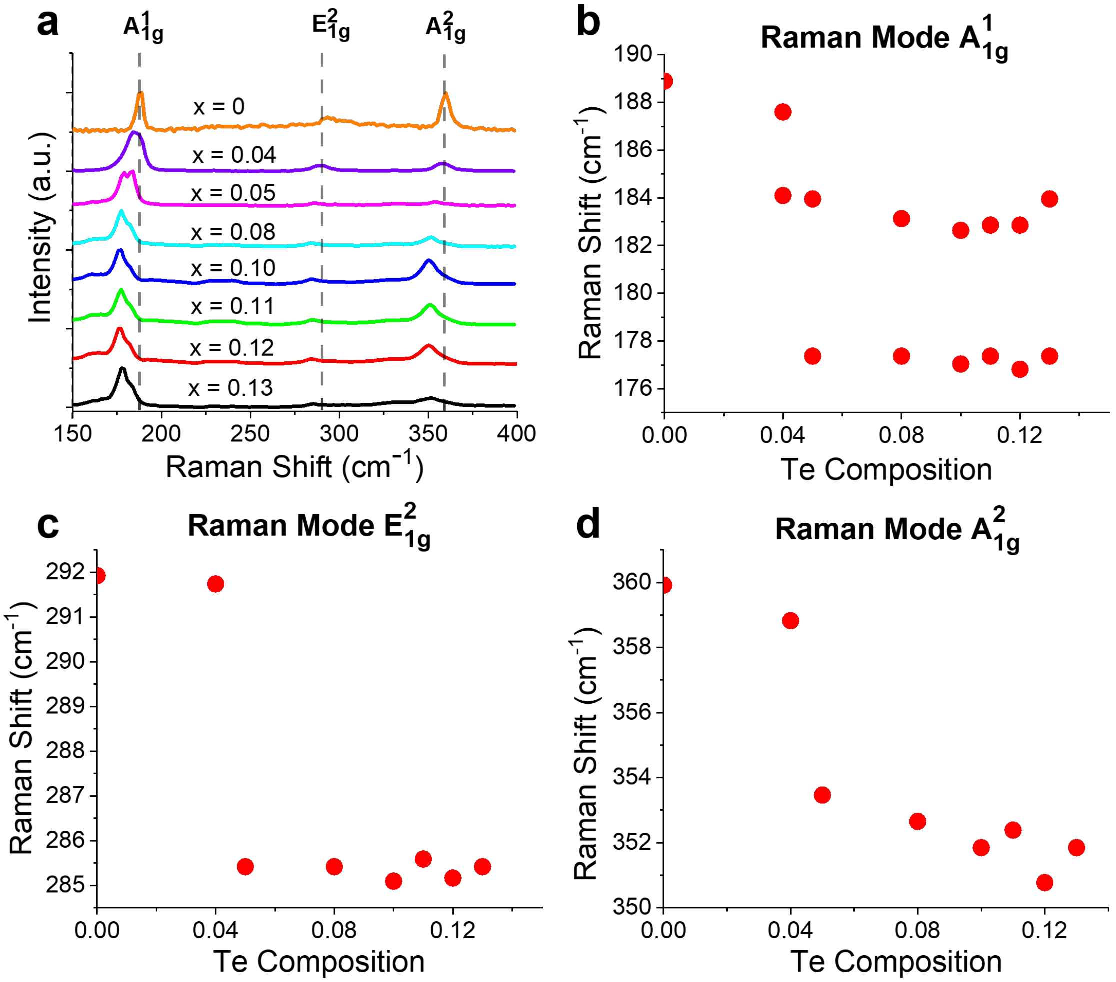

Figure 2.12: Raman of alloy nanowires. Alloy nanowires were mechanically transferred to a Si handle substrate. (a) Room-temperature Raman spectra versus composition of GaS$_{1-x}$Te$_x$ nanowires. (b-d) Raman-active optical modes versus composition

Figure 2.12b-d shows the quantitative red shift of the GaS Raman-active modes with tellurium incorporation. Modes A^1_{1g} and E^2_{1g} red shift by $5\,\mathrm{cm}^{-1}$ and $6\,\mathrm{cm}^{-1}$, respectively, with the addition of $x = 0.05$ tellurium but do not continue to significantly red shift with higher tellurium compositions. Mode A_{1g}^2 also shows a red shift of $7\,\mathrm{cm}^{-1}$ relative to the pure GaS Raman mode with the addition of $x = 0.05$ tellurium. This mode, however, does show a gradual red shift with higher tellurium compositions. Physically, the hardening of the Raman modes is consistent with the introduction of the heavier tellurium atom ($\mathrm{Te} = 126\,\mathrm{u}$, $\mathrm{S} = 30\,\mathrm{u}$). The differences in the behavior of the compression modes with the addition of tellurium atoms may be associated with the compressional and shear force constants for GaS atomic planes displacement summarized in Table 2.1. The force constants show the weaker nature of the S-S bond and the stronger nature of the Ga-Ga and Ga-S bonds. In the A_{1g}^1 mode, the restoring forces only involve Ga-Ga and S-S bonds, whereas in the A_{1g}^2 mode, the restoring forces also involve the Ga-S bonds. Therefore, the additional dependence of the A_{1g}^2 mode on the stronger Ga-S bonds results in a higher sensitivity in its Raman shift as tellurium atoms substitute sulfur atoms in the Ga-S bonds.

Bond	Compression (Nm^{-1})	Shear (Nm^{-1})
Ga-Ga	110	15.3
Ga-S	130	111
S-S	9.5	1.5

Table 2.1: Force constants for the different bonds in GaS [28].

2.3.4 Alloy Nanowire Growth Mechanism

Similar to GaS nanobelts, the primary growth mechanism of alloy nanowires is the vapor-liquid-solid growth mechanism. Evidence of the VLS growth mechanism lies in the presence of metal catalyst droplets at the end of the alloy nanowires as well as the large ratio of length to width of the nanowire. Note that the droplet shown in Figure 2.13 has not been characterized with EDS in order to preserve its pristine morphology for illustrations purposes (the extended exposure of the electron beam during EDS measurements can damage the nanowire and the droplet). However, from the spherical morphology of the droplet and the higher brightness compared to the alloy nanowire, it is likely that this droplet is a metal catalyst. In general, characterizing the composition of droplets from alloy nanowires is challenging because most alloy nanowires do not transfer with a catalyst droplet (it is likely that the droplets break off during the mechanical transfer process) and because the droplet composition cannot be decoupled from the composition of the nanowire due to the small size of the droplet relative to the nanowire and the electron beam spot size. For the few nanowires that did transfer with a droplet, the droplet composition has been found to be either a gallium-chalcogen alloy (i.e. self-catalyzed growth) or a gold-gallium-chalcogen alloy. Therefore, the post-growth composition of the catalyst droplet does not seem to determine the growth direction of the nanowire, meaning that both self-catalyzed and gold-catalyzed compositions have been found in c-axis nanowires. A more systematic study of the catalyst morphology, size and composition is necessary to further elucidate on the growth mechanism of alloy nanowires.

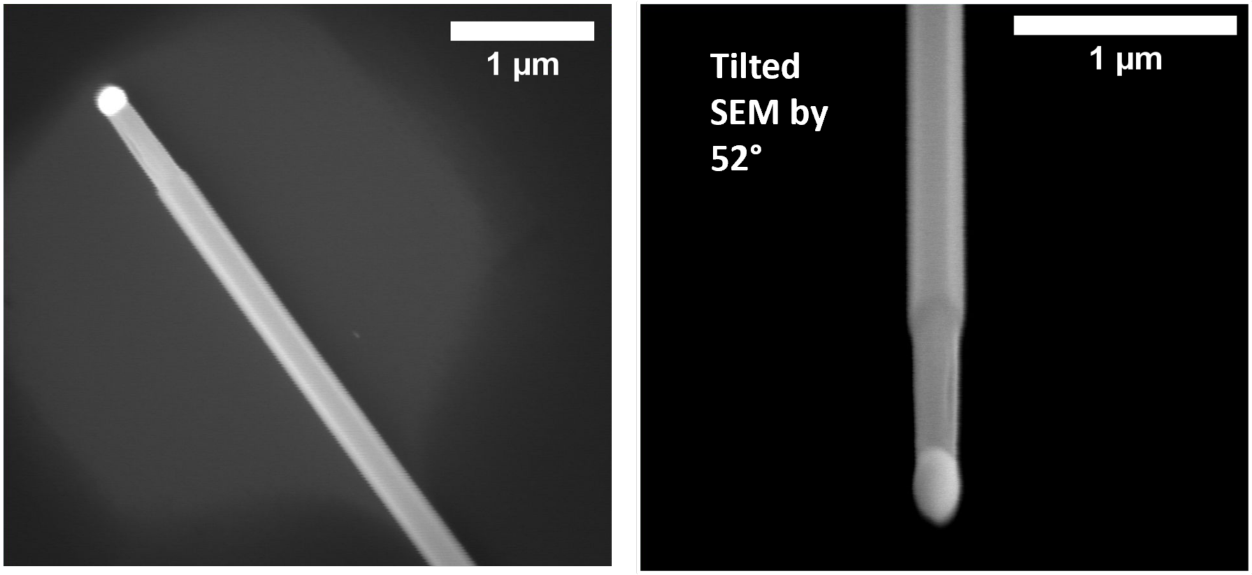

Figure 2.13: SEM of an alloy nanowire with nominal composition of $x = 0.05$ showing a droplet at its end.

In general, nanowires grow in the direction that minimizes the free energy of the nanowire-catalyst interface [139]. The growth direction can be controlled through the choice of catalyst, substrate, or growth parameters, such as temperature [139]. For example, Sutter *et al.* showed that using silver as the catalyst results in c-axis GaS nanowires [88]. However, in this work, the catalyst, substrate, and growth parameters are fixed, and the only variable is the introduction and modulation of tellurium during the growth. Therefore, it is proposed that the c-axis growth originates from the edge growth passivation by tellurium atoms.[1] Due to their larger atomic radius, tellurium atoms at the edges might bind to other tellurium atoms, forming a lower energy and less chemically reactive edge. Furthermore, due to the different evaporation rates from the GaS and GaTe powders, different ratios of GaS and GaTe gas molecules are present at the nucleation sites, influencing the edge growth rate based on the starting edge terminations. The quasi-triangular cross-section seen in 2.8b is then a kinetic Wulff shape resulting from three edges growing at a slower growth rate in the original hexagonal cross-section.

---

[1] Dr. Jerry Tersoff contributed to the discussion of the alloy nanowire growth mechanism.

2.4 Summary

In summary, GaS$_{1-x}$Te$_x$ alloy nanowires were successfully synthesized by using a gold-catalyzed, vapor transport method. GaS nanobelts possessed a rectangular cross-section and growth direction perpendicular to the c-axis. On the other hand, sulfur-rich, alloy nanowires possessed a hexagonal cross-section and growth direction parallel to the c-axis of the nanowire. The difference in growth directions between GaS nanobelts and alloy nanowires is hypothesized to be induced by the edge growth passivation by tellurium atoms. Due to the larger atomic radius of tellurium compared to sulfur, tellurium atoms at the edges might bind to other tellurium atoms, forming a lower energy and less chemically reactive edge.

In addition to the changes in morphology and growth direction, the alloy nanowires show a red shift in the Raman-active modes from GaS Raman-active modes with tellurium incorporation. This red shift can be explained by the heavier tellurium atoms incorporating into the GaS matrix. However, as the tellurium composition continues to increase, the Raman-active modes from the alloy nanowires do not continue to red shift significantly. This behavior might be indicative of a tellurium solubility limit in the GaS$_{1-x}$Te$_x$ alloy system. Additionally, although EDS measurements show a homogeneous distribution of tellurium atoms within the alloy nanowire, it is possible that the tellurium atoms are actually being incorporated interstitially or intercalted in the alloy nanowire, instead of being substitutionally incorporated. Therefore, the nominal composition of an alloy nanowire measured from EDS might be different than the actual, substitutional tellurium composition of the alloy nanowire. Finally, the splitting of Raman-active modes with nominal composition of $x > 0.04$ might be indicative of two polytypes being present in the alloy system. Possible ways to investigate the presence of polytypes will be discussed in Chapter 5.

Controlling the growth orientation of semiconductor nanowires is highly desirable to tailor properties for specific applications. The growth orientation has been shown to be controlled through the choice of catalyst, substrate, or growth parameters, such as temperature. [139] However, changing the morphology and growth direction through alloying offers exciting opportunities in tuning the properties of a material through composition.

Chapter 3

Optical Properties of GaS$_{1-x}$Te$_x$ Alloy Nanowires

Gallium telluride is a promising material for optoelectronic applications due to its direct band gap of 1.65 eV at 300 K [60]. However, it has been shown to be susceptible to oxidation under ambient conditions [72, 73]. On the other hand, gallium sulfide is an environmentally robust material under ambient conditions and possesses a wide, direct band gap of 3.05 eV and an indirect band gap of 2.59 eV at 77 K [29]. Therefore, the GaS$_{1-x}$Te$_x$ alloy system could offer a wide range of band gap tunability from near-infrared to visible, blue light, as well as environmental stability. In Chapter 2, the process of synthesizing sulfur-rich, GaS$_{1-x}$Te$_x$ nanostructures was described and their structural properties were characterized. The GaS$_{1-x}$Te$_x$ nanostructures were found to possess a fast-growth direction parallel to the c-axis and the presence of an ϵ stacking phase within the β matrix was proposed based on the splitting of the A_{1g}^1 Raman-active mode.

In this chapter, the optical properties of sulfur-rich, c-axis, GaS$_{1-x}$Te$_x$ alloy nanostructures are studied. In Section 3.1, a background of photoluminescence spectroscopy is given and PL measurements for the alloy nanostructures are discussed. In Section 3.2, cathodoluminescence spectroscopy measurements are presented. Finally, in Section 3.3, a summary of the results are given. Studying the optical properties of c-axis, alloy nanowires with possible polytypes could offer more degrees of freedom to engineer the optoelectronic properties of a material.

3.1 Photoluminescence Spectroscopy of Alloy Nanowires

3.1.1 Luminescence Fundamentals

Luminescence is a non-equilibrium process in which light is emitted as a result of an external excitation [140]. The excitation sources can be monochromatic light (photoluminescence), electron beam (cathodoluminescence), electrical injection of carriers through metal contacts (electroluminescence), and heat (thermoluminescence). This work will focus on photoluminescence and cathodoluminesnce as characterization techniques to study the optical behaviours of GaS nanobelts and alloy nanowires.

Photoluminescence (PL) spectroscopy is a widely used technique to characterize a material's intrinsic electronic transitions between energy bands as well as extrinsic electronic transitions among energy bands, impurity and defect levels [140]. In PL, absorbed photons excite electrons from the valence band into the conduction band. The generated electrons and holes then thermalize to the lowest state in the conduction and valence bands, respectively, through phonon emission. Finally, the electrons and holes recombine across the fundamental band gap or via defect levels through photon emission [140, 141].

PL can be divided into intrinsic and extrinsic luminescence. Two types of transitions involved in intrinsic luminescence are interband and excitonic transitions [142]. Interband transitions involve the recombination of an electron in the conduction band and a hole in the valence. Interband transitions in indirect band gap semiconductors require the assistance of a phonon and consequently have up to four orders of magnitude lower probability of occurring than interband transitions in direct band gap semiconductors [142]. Interband transitions can be observed at relatively high temperatures for very pure semiconductors [142]. Excitonic transitions involve the recombination of a Wannier exciton. A Wannier exciton is a quasi-particle composed of an electron in the conduction band bound to a hole in the valence band by Coulombic forces, analogous to a hydrogen atom [141, 142]. Two characteristics of a Wannier exciton are that it can move around the crystal but carries no current due to its charge neutrality and that its radius is larger than the lattice constant of the crystal [142]. Wannier excitons are only observed at low temperatures, when the exciton binding energy is much larger than the thermal energy [142], and at low doping concentrations, when free charges cannot screen the Coulombic forces [141].

Extrinsic luminescence involves the intentional addition of impurities or defects into the semiconductor. Extrinsic luminescence can involve unlocalized and localized transitions [142]. In unlocalized transitions, free electrons in the conduction band and free holes in the valence band partake in the light emission process [142]. Transitions can occur between a free and bound carrier and between a bound electron at a donor and a bound hole at an acceptor in what is known as a donor-acceptor pair transition [142]. Finally, localized transitions occur in localized, luminescence centers, such as impurities and lattice defects (e.g. an electron trapped in an anion vacancy) [142]. The possible emission processes for PL are shown schematically in Figure 3.1.

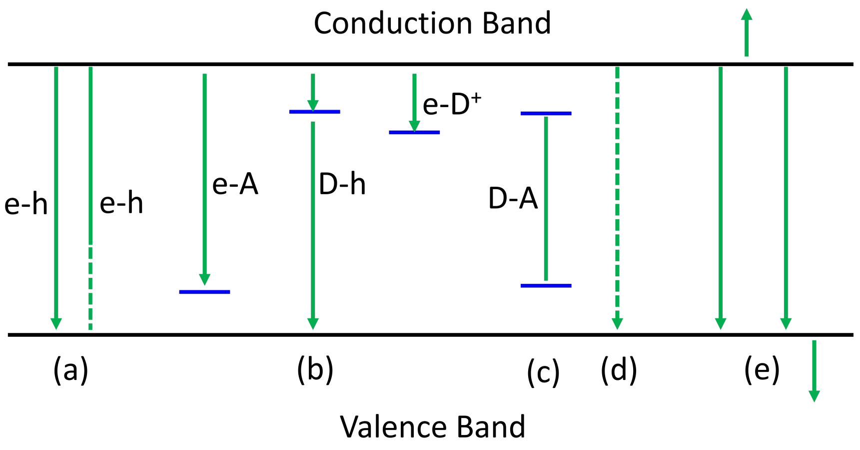

Figure 3.1: Schematic of emission processes. (a) Band-to-band emission (b) Conduction band or valence band defect recombination (c) Donor-acceptor pair recombination (d) Multiphonon emission (e) Auger recombination. Figure adapted from [140].

Peaks in a PL spectrum have three main features that give important information about the sample. The first feature is the wavelength of the emission peak, which gives information about the transitions. The intensity of the peaks is a direct indicator of the sample's optical quality; higher intensity is an indication of a higher optical quality [140]. Finally, the linewidth gives information about defect density, surface quality, and alloy disorder [140].

Changing the parameters of a luminescence experiment, such as the sample temperature, laser exposure time, and laser pumping power, allows for the study of various optical behavior in a material. For example, at low temperatures, non-radiative recombination can be suppressed and new states are observed in the PL spectrum as fine structures [140]. Another important parameter in a micro-photoluminescence experiment is the spatial resolution of the system. The spatial resolution of a micro-PL system can be estimated by Equation 3.1, where λ is the laser wavelength, NA is the numerical aperture of the objective lens, and d is the diameter of the laser spot on the sample,

$$d = 1.22 \times \frac{\lambda}{NA}. \tag{3.1}$$

In the following sections, two different micro-photoluminescence spectroscopy systems were used to probe the optical transitions of the alloy nanowires. The first micro-PL system consisted of a 488 nm laser line with 100 mW maximum power output as the excitation source, a silicon-based CCD as the detector, and a 1200 gr/mm grating. The second micro-PL system consisted of a 660 nm laser line with 500 mW maximum power output as the excitation source, a silicon-based CCD as the detector, and a 830 gr/mm grating. The conversions between power percentage (the parameter tuned in the experiment) and power density on the sample are given in Appendix C.

3.1.2 Photoluminescence of Handle Substrate

To characterize the true, optical transitions from the nanowires, it is imperative to characterize the luminescence from the handle substrate in order to distinguish it from the nanowire luminescence. Therefore, the PL spectra of Si, SiO_2, a pristine handle substrate, and two transferred handle substrate sites were measured with the 488 nm laser line, as shown in Figure 3.2. In this work, the handle substrate is a 100 nm SiO_2-on-Si substrate patterned with enumerated gold markers. A pristine handle substrate (PHS) refers to a handle substrate that has not been used to transfer nanowires. A transferred handle substrate (THS) refers to a handle substrate to which nanowires have been transferred to. The sites on the THS were chosen based on the criteria that no nanowires were visible in the field of view of the optical microscope. The PHS and THS sites were characterized with PL to observe if chemical residue from the lithography process used for the gold markers or debris from the nanowire transfer process, respectively, contributes to the handle wafer luminescence.

Figure 3.2a compares the PL spectra from a Si substrate measured at 5% and 100% laser powers. The spectrum measured with 5% power does not have any peaks or distinct features. However, the spectrum measured with 100% power has a high-intensity signal near 1.25 eV and has a broad, low-intensity signal that spans the energy region from 1.4 eV to 2.5 eV, as shown in Figure 3.2b. Figure 3.2c compares the PL spectra for a pristine handle substrate and SiO_2 and Si wafers. The PL spectrum from the SiO_2 wafer has the same features as the PL spectrum from the Si wafer; but the PL spectrum from the SiO_2 wafer is higher in intensity, even though the Si wafer was measured at 100% power and the SiO_2 wafer was measured at 10% power. A possible explanation for this discrepancy is that the features near 1.25 eV are related to the luminescence from the oxide layer thickness of the wafer. Since the Si wafer only has a thin layer of native oxide, it does not show a significant PL signal near 1.25 eV at 5% power and shows a low-intensity signal at 100% power. On the other hand, the SiO_2 wafer has 100 nm of grown oxide (which is expected to be much thicker than the native oxide on the Si wafer) and therefore its luminescence intensity at 10% power is higher than the luminescence from the Si wafer at 100% power. The PL spectrum from the PHS had a more intense and broader peak near 1.25 eV than the PL spectra from the SiO_2 and Si wafers. This indicates that the photolithography process likely leaves a chemical residue that contributes to the luminescence from the SiO_2. Figure 3.2e compares the PL spectra from a PHS and two THS sites. The specta from the PHS and THS2 have similar features near 1.25 eV. However, THS1 does not have prominent features near 1.25 eV. This can be explained by chemical residue inhomogeneity throughout the sample.

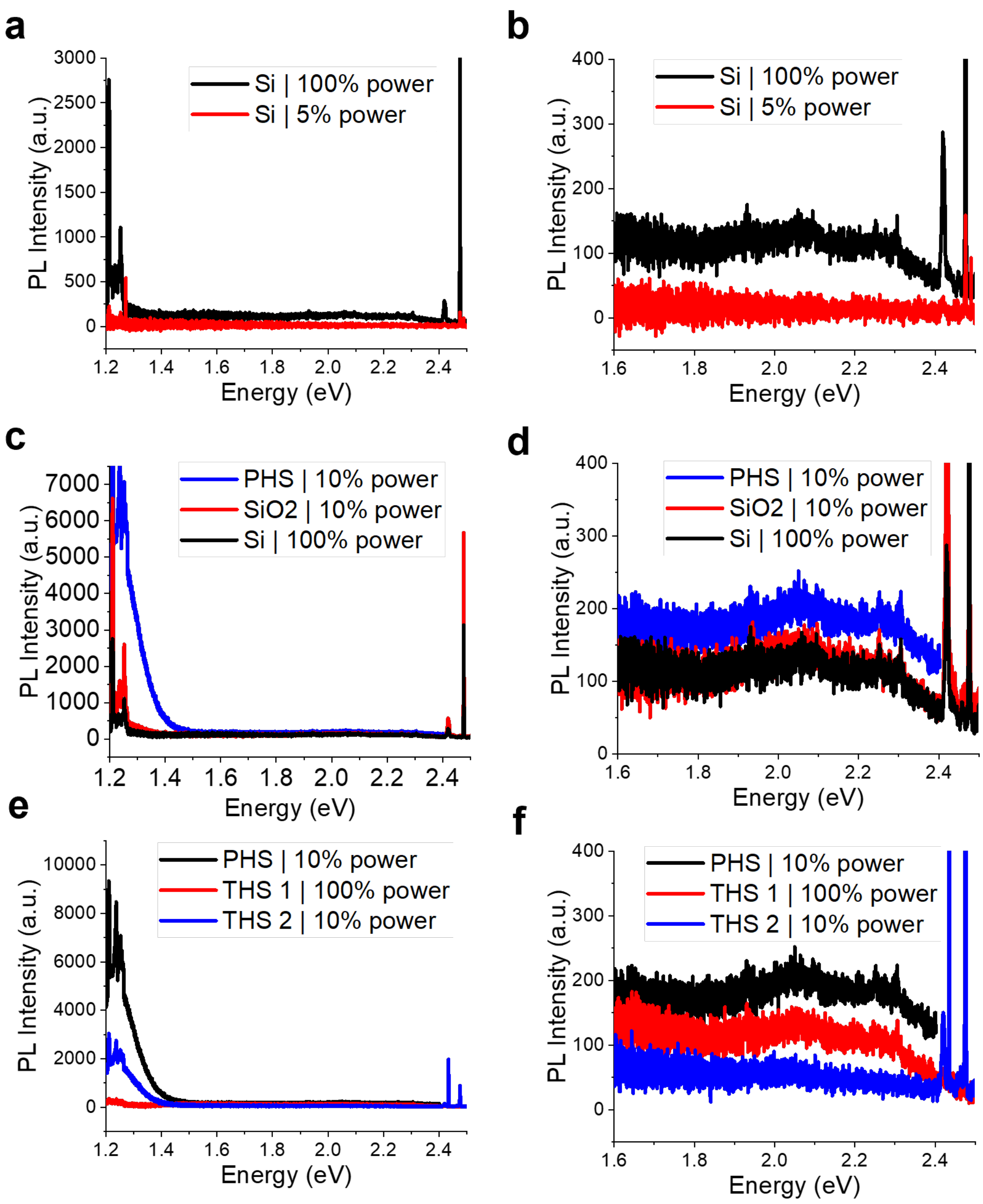

Figure 3.2: PL spectra from various substrates measured with a 488 nm laser line at room-temperature. (a) Si substrate measured with 5% and 100% laser power. (b) Pristine handle substrate (PHS) and SiO_2 wafer measured at 10% laser power, and a Si wafer measured at 100% laser power. (c) PHS measured at 10% power and two transferred handle substrates (THS) measured at 100% and 10% laser powers. (b,d,f) Magnified regions of the PL spectra shown in (a, c, d), respectively.

3.1.3 Photoluminescence of GaS Nanobelts

Room-temperature, micro-PL spectroscopy was used to probe the optical transitions of GaS nanobelts. The experimental set up consisted of a 488 nm laser line with 100 mW maximum power output as the excitation source, a silicon-based CCD as the detector, and a 1200 gr/mm grating.

The PL spectra of two different GaS nanobelt morphologies were measured at 10% laser power, as shown in Figure 3.3. Both spectra display a low-intensity, broad signal spanning from 1.40 eV to 2.40 eV. The broad signal can be fitted with two Gaussian functions. The Gaussian function centers, C_1 and C_2, of the two GaS nanobelts agree to 0.04 eV.

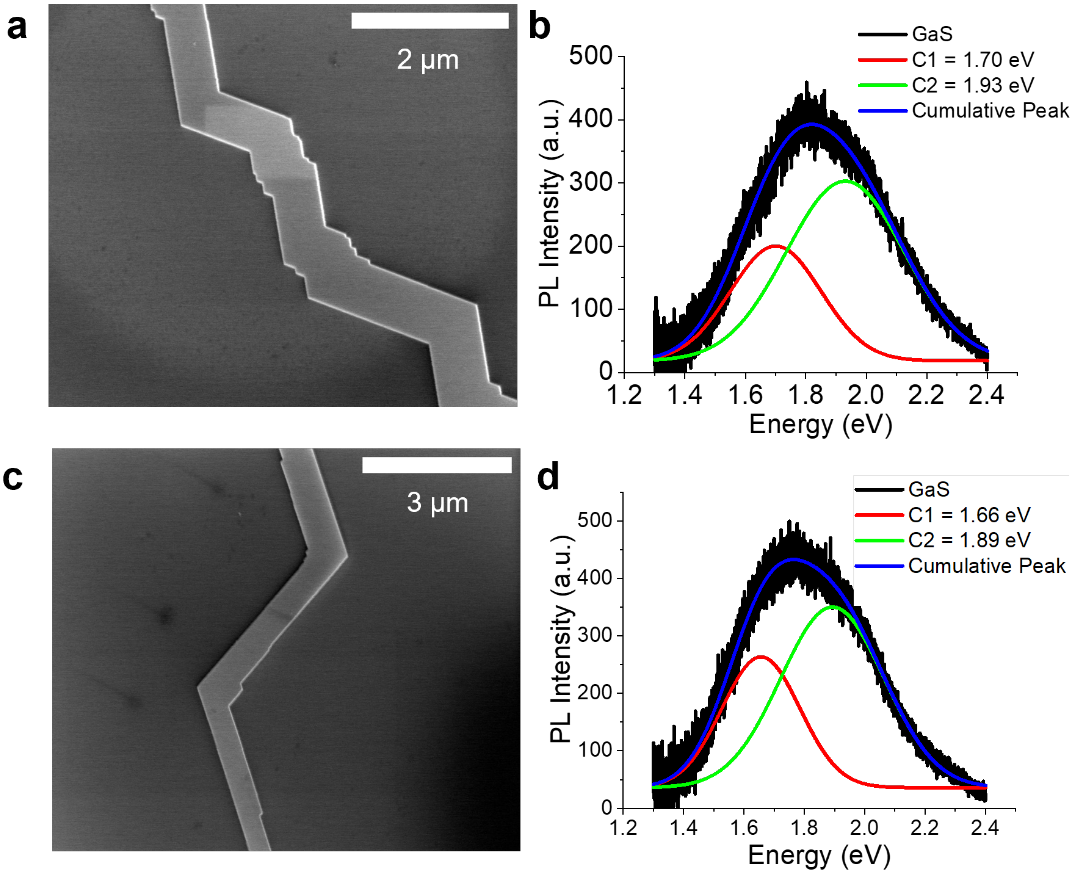

Figure 3.3: PL spectra from two GaS nanobelts with different morphologies measured at room-temperature with a 488 nm laser line. (a) Zig-zag GaS nanobelt with short intervals of sawtooth faceting. (b) Zig-zag GaS nanobelt without sawtooth faceting.

The band gap of GaS has been measured by optical absorption to be 2.59 eV for indirect transitions and 3.05 eV for direct transitions at 77 K [29]. However, PL measurements at

77 K have shown energy peaks that are lower energy than the reported band gaps from absorption in addition to lower energy peaks attributed to defects, as is shown in Table 1.1. Only two studies performed at 77 K have reported PL peaks close to the direct band gap of GaS at 2.89 eV [32] and 2.74 eV [43]. Several studies have reported a PL peak in the range of 2.51 eV to 2.61 eV. This PL peak has been attributed to the bound indirect exciton in GaS. The third peak reported is in the range of 2.0 eV to 2.32 eV and is attributed to donor-acceptor pair recombination. A slightly lower energy peak is reported in the range of 1.91 eV to 2.17 eV and is commonly attributed to acceptor levels from Ga vacancies. Finally, the fifth PL peak reported is in the range of 1.62 eV to 1.68 eV and is attributed to sulfur interstitials. Interestingly, only one study reported a PL peak at 1.43 eV and it was for GaS bulk crystals grown in oxidizing atmosphere [31]. The role of oxygen was studied by Jung *et al.* through DFT calculations, and it was reported that oxygen chemisorption leads to a decrease in the direct band gap until it converges with the indirect gap of GaS. As shown in Table 1.1, room-temperature PL has been reported to have peaks with similar energies as PL peaks measured at 77 K. The only exception is the study by Ho *et al.*, which reported room-temperature PL with a peak at 2.43 eV attributed to a donor defect level due to epsilon stacking in the beta GaS matrix [114].

The excitation energy used to characterize the GaS nanobelts grown in this work was 488 nm (2.54 eV). This energy is right at the excitation limit for the indirect band gap of GaS. Therefore, it is likely that the origin of the two low-intensity peaks in the GaS PL spectra near 1.70 eV and 1.90 eV originate from structural defects formed during the growth, such as sulfur interstitials and gallium vacancies.

3.1.4 Photoluminescence of Alloy Nanowires

3.1.4.1 PL of Alloy Nanowires Measured with a 488 nm Laser Line

Room-temperature, micro-PL spectroscopy was used to probe the optical transitions of alloy nanowires. The experimental set up consisted of a 488 nm laser line with 100 mW maximum power output as the excitation source, a silicon-based CCD as the detector, and a 1200 gr/mm grating. All the wires were measured at 0.05% laser power to minimize damage to the nanowire and signal from the handle substrate. The general shape of the PL spectrum for an alloy with $x = 0.10$ nominal composition is a high-intensity signal centered near 1.50 eV, as shown in Figure 3.4a. The alloy PL signal is much more intense than the PL signal from the pure GaS nanobelt and the handle substrate, as shown in Figure 3.4a and magnified in b. Note that the intensity of the PL signal from the GaS nanowire in Figure 3.4 is lower than the PL signal in Figure 3.3 because the power used to measure the PL signal in Figure 3.4 is lower.

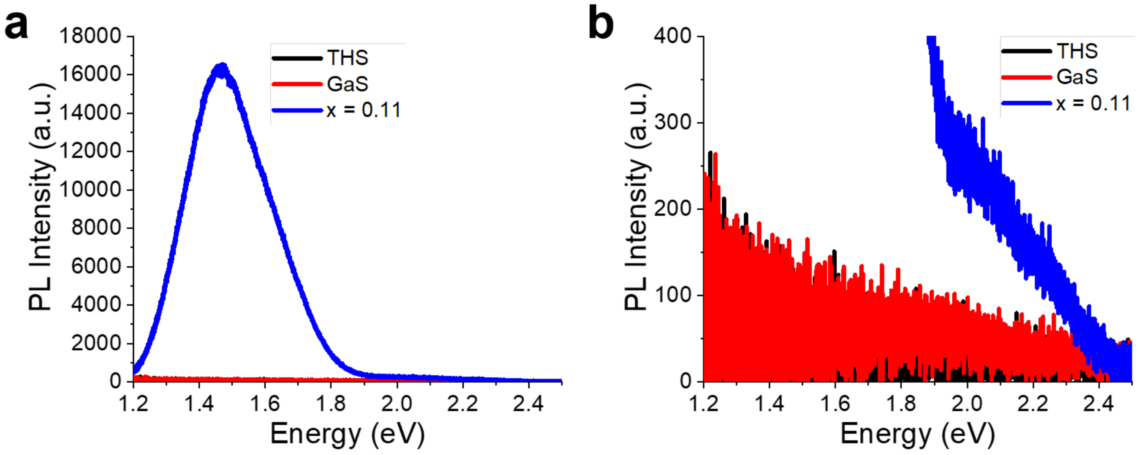

Figure 3.4: Comparison of the PL spectra from a GaS nanobelt and an alloy nanowire. (a) Room-temperature, micro-PL measured with a 488 nm laser line for an alloy nanowire with composition $x = 0.11$, a GaS nanobelt, and a clean section in the transferred handle substrate (THS). (b) Magnified section of (a) to highlight the features of the GaS nanobelt and THS spectra.

Furthermore, the PL spectrum from an alloy nanowire may exhibit low-intensity peaks in addition to the primary, high-intensity peak, as shown in Figure 3.5. The spectra shown in Figure 3.5 are from three different wires and were chosen to highlight the differences in features among PL spectra. In Figure 3.5a, the spectrum has a prominent shoulder near 1.60 eV in addition to the primary peak near 1.55 eV. In Figure 3.5b, there are no major shoulders that appear besides the primary peak near 1.50 eV. Finally, in Figure 3.5c, the spectrum has a broad and low-intensity shoulder near 2.00 eV in addition to the primary peak. Additionally, this spectrum has much lower intensity than the first two, possibly due to the higher tellurium composition changing the crystalline quality of the nanowire. When fitting the alloy PL spectra with Gaussian functions, it is clear that the signal is a convolution of PL peaks. For example, the centers of the Gaussian functions are 1.31 eV, 1.44 eV, and 1.57 eV for the alloy nanowire with $x = 0.12$ composition.

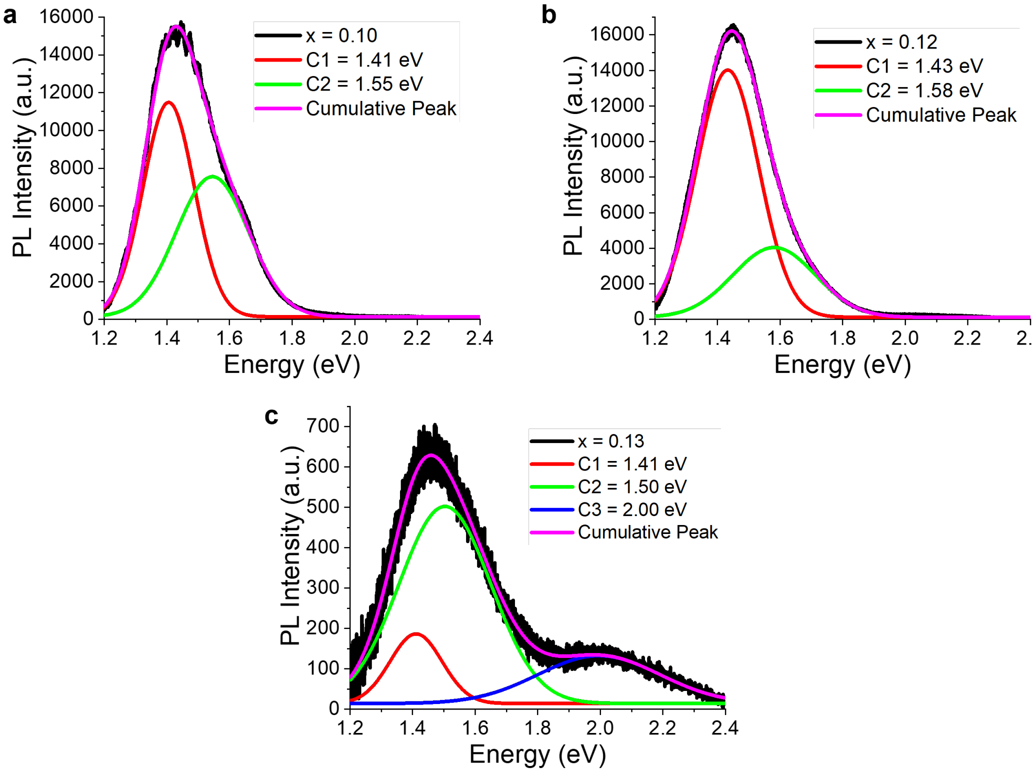

Figure 3.5: PL spectra from alloy nanowires measured at room-temperature with a 488 nm laser line. The different spectra exemplify the various lower-intensity shoulders that may appear in addition to the primary, high-intensity peak near 1.50 eV. The alloy nanowires have nominal compositions of (a) $x = 0.10$ (b) $x = 0.12$ and (c) $x = 0.13$.

3.1.4.2 PL of Alloy Nanowires Measured with a 660 nm Laser Line

The room-temperature PL of GaS has been reported to have peaks at 2.43 eV for bulk crystals [41], 2.51 eV and 2.74 eV for nanohorns [35], and 2.53 eV for nanobelts [45]. Therefore, performing PL measurements with a 488 nm (2.54 eV) laser means that the laser energy could be exciting above the indirect band gap of GaS. If this is the case, then it is possible that the room-temperature PL peaks observed originate from defect levels within the band gap. However, if the nanostructures are excited with a laser wavelength below the indirect band gap of GaS, then it is likely that the observed PL peaks are from a new, fundamental band gap shifted to lower energies by alloying. Therefore, the alloy nanostructures were measured with a 660 nm (1.88 eV) laser line to test whether the PL peaks observed with the 488 nm (2.54 eV) laser line are still observed when measured with a laser below the band gap.

The experimental set up consisted of a room-temperature, micro-PL system with a 660 nm (1.88 eV), 500 mW maximum power laser line as the excitation source, a silicon-based CCD as the detector, and a 830 gr/mm grating. The alloy nanowires were measured with 0.06 mW (0.012%) nominal laser power to minimize wire damage and handle substrate luminescence.

The shape of the PL spectrum from an alloy nanowire with $x = 0.10$ nominal composition is a low-intensity, broad signal centered near 1.40 eV. Compared to the spectra measured with the 488 nm laser line, the spectra from the 660 nm laser line have lower intensity and a more prominent, curved baseline, as shown in Figure 3.6. Therefore, signal processing of the original spectra was necessary to more accurately fit PL peaks. Figure 3.6 shows the sequence of signal processing steps. Initially, the spikes are manually removed from the spectrum and the energy range is trimmed to the 1.1 eV (detector limit) to 1.8 eV (laser limit) energy region. In the second step, the spectrum is smoothed using a Savitzky-Golay function with a window size of 50 data points. The smoothing allows for a more accurate baseline removal in the next step. The baseline removal is performed by manually selecting points on the spectrum and using a straight line interpolation or exponential growth function, depending on the curvature of the baseline, to remove the baseline. Finally, two Gaussian functions are used to fit the PL spectra. Note that the PL spectra for alloy nanowires measured with the 488 nm laser line were also processed with the same steps, except that the data was smoothed with a percent filter function with window size of 20 points.

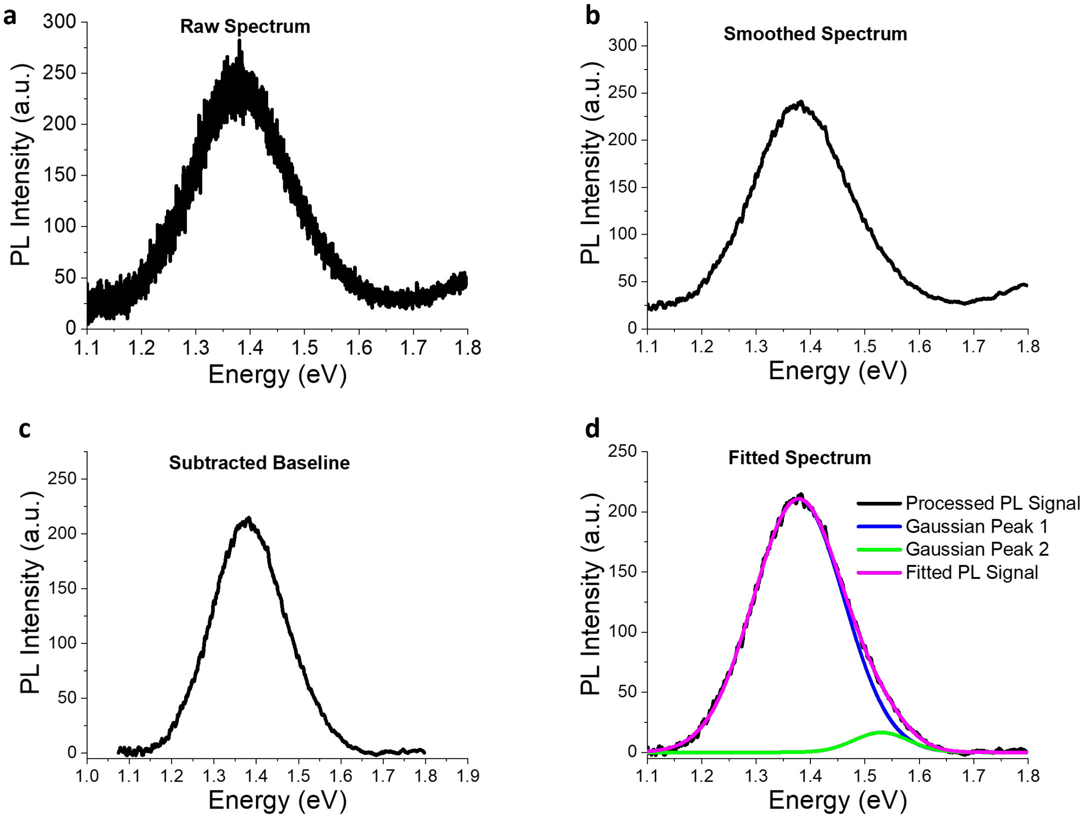

Figure 3.6: Data processing steps for PL spectra measured with the 660 nm laser line. (a) Raw PL spectrum. (b) PL spectrum smoothed with a Savitzky-Golay function. (c) PL spectrum after the baseline removal step. (e) Processed PL spectrum fitted with two Gaussian functions.

The PL spectra measured with the 660 nm and 488 nm laser lines are compared in Appendix D. The PL spectra from the 660 nm laser line has two center peaks that, on average, are lower in energy compared to the center peaks measured with the 488 nm laser line. The lower energy peaks from the 660 nm laser line are lower in energy compared to the lower energy peaks from the 488 nm laser line by 0.048 eV while the higher energy peaks are lower in energy by 0.045 eV. The PL peak energy difference between the two laser lines could be explained by nanowire heating effects. The 660 nm laser line has a power output that is five times higher than the 488 nm laser line and therefore could raise the local temperature of the nanowire more drastically during the measurement, causing the PL peaks to shift to lower energy. A relationship for the temperature dependence of semiconductor band gaps was developed by O'Donnell and Chen [143]. The relationship is described in Equation 3.2, where $E_g(0)$ is the band gap at zero temperature, S is a dimensionless coupling constant, and $\langle\hbar\omega\rangle$ is an average photon energy [143].

$$E_g(T) = E_g(0) - S\langle\hbar\omega\rangle[coth(\langle\hbar\omega\rangle/2kT) - 1] \tag{3.2}$$

The fitting parameters for the indirect band of GaS are $E_g(0) = 2.69 \pm 0.002\,\text{eV}$, $S = 4.8 \pm 0.4$, and $\langle\hbar\omega\rangle = 22 \pm 3\,\text{meV}$ in the range of 0 K to 300 K [30]. The resulting plot for the indirect band gap energy of GaS versus temperature is shown in Figure 3.7. The plot was extrapolated in the temperature range of 300 K to 600 K using Equation 3.2 in order to show the indirect band gap change up to the growth temperature of an alloy nanowire with nominal composition of $x = 0.10$. Assuming a linear relationship at temperatures above 200 K, the slope of the linear region is 7.6×10^{-4}eV K^{-1}, or a 0.076 eV change per 100 K temperature change. Based on this plot, the indirect band gap of GaS at 300 K is 2.53 eV, and decreases by 0.047 eV, the same energy difference between the PL spectra of the two laser lines, at 360 K. Therefore, it is possible that local laser heating due to different laser powers could result in PL peak shifts.

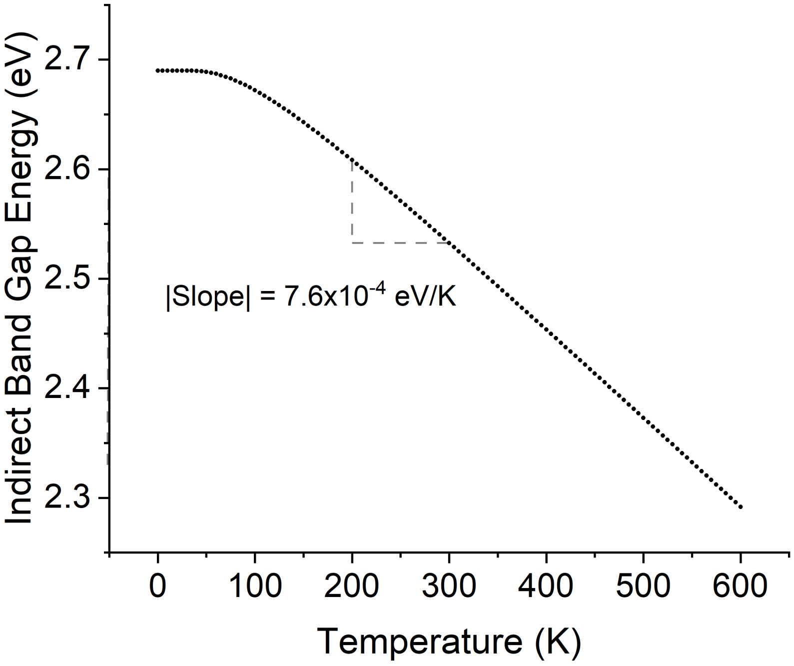

Figure 3.7: Temperature dependence of the indirect band gap of GaS as described in Ref [30, 143]

3.1.4.3 PL Power Dependence of Alloy Nanowires

Due to the differences observed in PL peak positions between the 488 nm and 660 nm laser lines, it is important to verify whether changes in laser power within a laser line also cause shifts in PL peak positions. Therefore, the power dependency of alloy nanowires was studied using the 488 nm laser.

The maximum power density of the 488 nm laser line using a 50x objective lens is $33.74\,\mathrm{W\,m^{-2}}$. The power was reduced through optical filters controlled automatically by the PL software settings. For a conversion table between power percentages and actual power density at the sample see Appendix C.

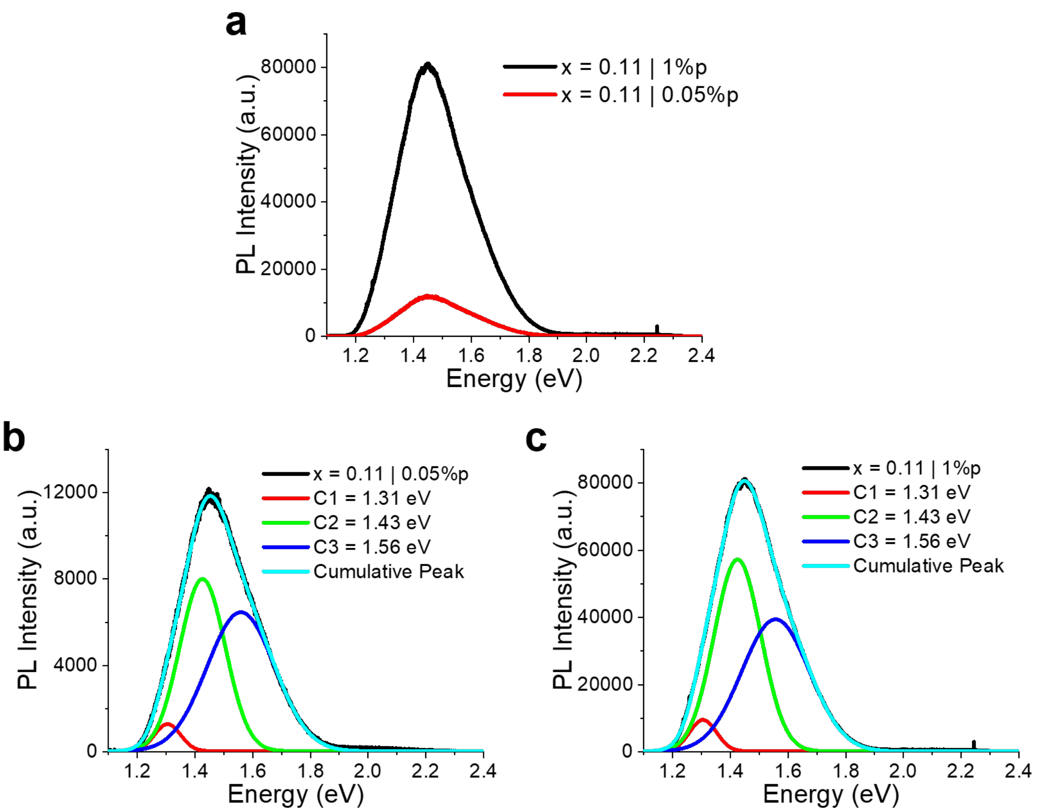

Figure 3.8: PL power dependency of an alloy nanowire with nominal composition $x = 0.11$ measured with a 488nm laser line. (a) Comparison of PL spectra from alloy nanowire measured with 1% and 0.05% laser powers. (b) PL spectrum of alloy nanowire measured with 0.05% laser power and fitted with three Gaussian functions. (c) PL spectrum of alloy nanowire measured with 1% laser power and fitted with three Gaussian functions.

The difference in PL intensities between the two power measurements for the same alloy nanowire is shown in Figure 3.8a. The PL spectrum for an alloy nanowire with nominal composition of $x = 0.11$ measured with 1% ($0.29\,\mathrm{W\,m^{-2}}$) laser power exhibits more than four times higher intensity than the same wire measured with 0.05% ($0.04\,\mathrm{W\,m^{-2}}$) laser power. The PL peak positions for the two power settings were analyzed in Figures 3.8b and c. The PL spectrum for the 0.05% power measurements has center peaks at 1.31 eV (signal from the substrate), 1.43 eV, and 1.56 eV. The PL spectrum for the 1% power measurement has center peaks at exactly the same locations as the 0.05% measurement. Therefore, using a higher PL power increases the intensity of the PL spectrum but does cause shifts in the PL peak positions when increasing the power from 0.05% to 1%. Finally, measurements with higher laser power were attempted but the PL signal saturated above 5% ($1.68\,\mathrm{W\,m^{-2}}$) laser power.

3.1.5 Energy versus Nominal Composition

The PL peak energies from the 488 nm laser line and the band gaps of GaS from literature are plotted versus the nominal tellurium composition in Figure 3.9. The energies of PL peaks measured with 100x and 50x objective lenses were averaged, as well as PL peaks of similar energies from nanowires with the same nominal compositions. For pure GaS, the room-temperature PL and PzR values for the direct band gap (2.86 eV), indirect band gap (2.53 eV), and donor level from the epsilon stacking defect (2.43 eV) were obtained from the work of Ho *et al.* [114].

At composition of $x = 0.03$, the PL peaks show a decrease in energy from the reported indirect and direct band gaps of GaS of $E_{g,direct} = 2.86\,\mathrm{eV}$ and $E_{g,indirect} = 2.53\,\mathrm{eV}$ [114] to 1.42 eV, 1.55 eV and 1.91 eV. However, the energy follows a flat trend with additional tellurium incorporation. A possible explanation for this behavior is that the tellurium is not incorporating substitutionally into the GaS host matrix. Instead, due to a miscibility gap, the tellurium atoms are incorporated as interstitials or intercalated between the layers. As a result, the measured composition of tellurium from EDS is the nominal composition in the alloy nanowire and not the substitutionally alloyed composition. Further evidence of the nominal composition being different than the substitutional composition is the behavior of the Raman modes with tellurium composition. All three Raman modes, A^1_{1g}, E^2_{1g}, and A^2_{1g}, show a prominent decrease in wavenumber with a few percent of tellurium incorporation and a flat trend with additional tellurium incorporation, as shown in Figure 2.12b.

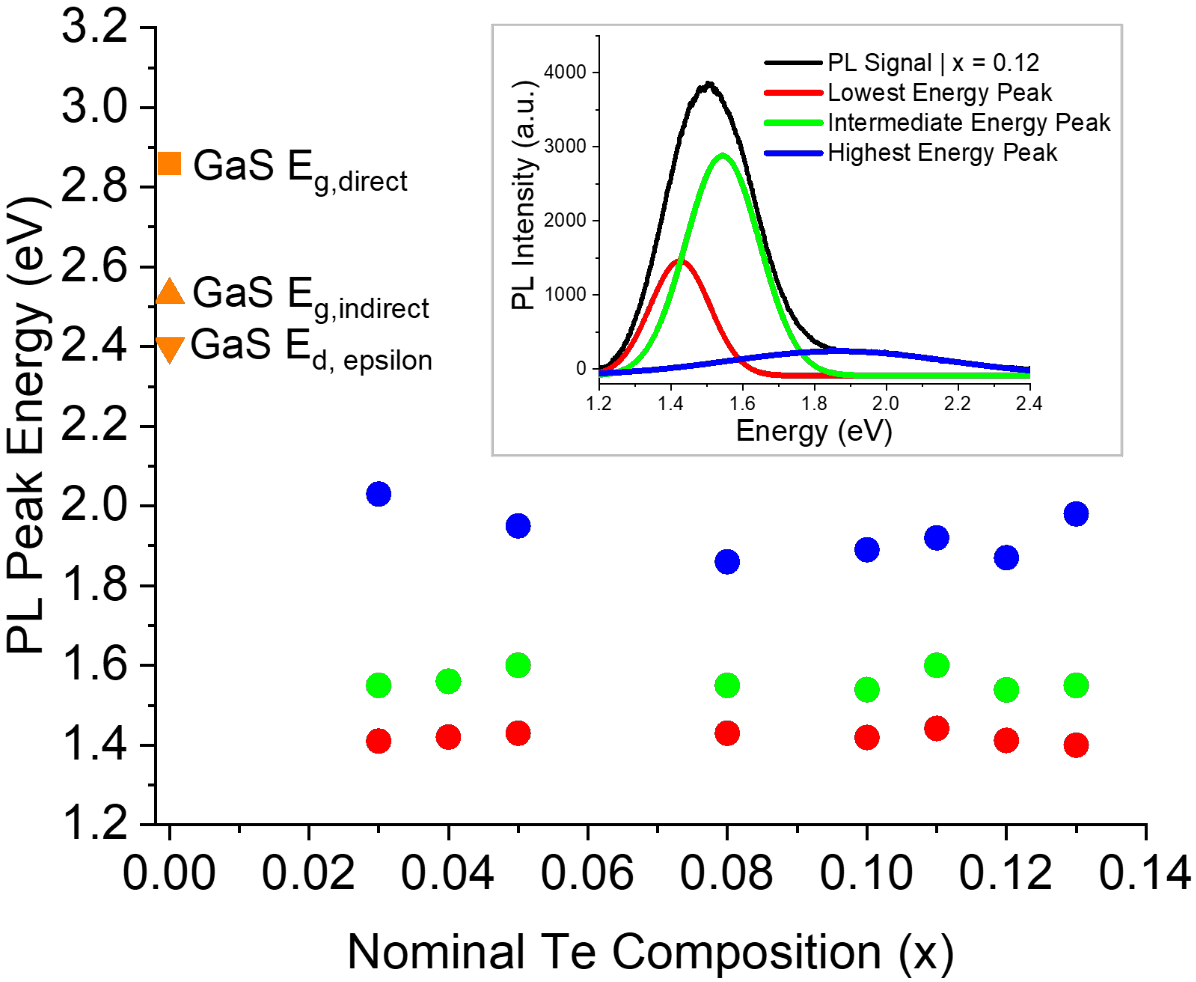

Figure 3.9: PL peak energy versus nominal tellurium composition. The PL measurements were performed at room-temperature with the 488 nm laser line. The GaS band gap values and epsilon defect level were obtained from Ho *et al.* [114].

3.2 Cathodoluminescence Spectroscopy of Alloy Nanowires

In cathodoluminescence (CL), high energy electrons are used as the excitation source. In general, CL provides higher spatial resolution than PL and leads to emission from all luminescence processes. In this work, CL spectroscopy was performed on selected alloy nanowires. The CL experiments and the data analysis, specifically the principal component analysis (PCA), were performed in collaboration with Dr. Shaul Aloni at the Molecular

Foundry. The CL measurements were performed at 85 K and consisted of raster-scanning an area surrounding the wire and taking a CL spectrum at each pixel in the scanned image.

There were two approaches to analyzing the CL data that offered different information. In the first approach, the raw data was manually inspected. The data from a CL measurement consists of an intensity map of the area containing the nanowire, with each pixel in the map having a corresponding CL spectrum. Analyzing the CL data in this manual approach allowed for the comparison of individual pixels along the nanowire to assess the uniformity of the nanowire. For example, in Figure 3.10, five pixels are selected from the intensity map. Pixel 1 corresponds to a pixel off the nanowire, and shows a low-intensity signal. The non-zero signal from Pixel 1 is expected due to the large penetration volume from the high-energy electron beam and the short distance of Pixel 1 from the nanowire. Pixels 2-5 are located along the nanowire. The CL spectra from Pixels 2 and 3 have similar intensity and are fitted with Gaussian peaks centered at 1.86 eV and 2.23 eV. It is likely that the broad, lower intensity shoulder is composed of two Gaussian peaks, but due to the low intensity of the spectra, the broad shoulders cannot be deconvolved. The CL spectra for Pixels 4 and 5 have higher intensities than the other pixels and therefore three Gaussian functions can be used to perform the fitting. The centers of these Gaussian functions are located at 1.73 eV, 1.86 eV, and 2.24 eV for Pixel 4 and 1.75 eV, 1.90 eV, and 2.24 eV for Pixel 5. This manual data analysis approach showed that the alloy nanowire possesses uniform luminescence properties as the four pixels on the alloy nanowire showed similar luminescence peaks.

The second approach of processing the CL data consisted of using principal component analysis (PCA) to analyze the entire CL map at once, rather than manually analyzing one pixel at a time. PCA is a mathematical algorithm that aids in the comparison and grouping of different data by reducing the dimensionality of large data sets while preserving as much statistical information, or variance, as possible [144–146]. Principal components are uncorrelated, linear combinations of the original data variables that contain most of the information in the original data set. In the case of assessing the CL data of an alloy nanowire, PCA offers higher statistical accuracy in determining peak positions compared to a single spectrum from a nanowire pixel because it takes into account all the spectra in the CL map. Furthermore, because PCA bins data into different components, it can separate the background signal from the nanowire signal, since each luminescence source is represented by a different component. Figure 3.11 shows the eight different components and their respective spectra for the data collected from the same nanowire shown in Figure 3.10.

Component 2 from the PCA analysis best represents the luminescence from the nanowire. Therefore, the spectrum from Component 2 is smoothed with a percent filter function and fitted with three Gaussian functions centered at 1.74 eV, 1.90 eV, and 2.23 eV, as shown in Figure 3.12. The CL peaks from the spectrum for Component 2 match the CL peaks from the spectra in Figure 3.10, further confirming the luminescence homogeneity of the nanowire. It is important to note that the Gaussian fittings for the CL data were performed with the least number of Gaussian functions that yielded a reasonable fit. Fittings with additional Gaussian functions were also performed. For example, the high-intensity peak in the CL spectrum can be fitted with two Gaussian functions, instead of one, with centers at 2.20 eV and 2.25 eV. The physical validity of the additional Gaussian function will have to be determined by additional experiments addressing the presence of poltytypes and defect levels in the alloy nanowires.

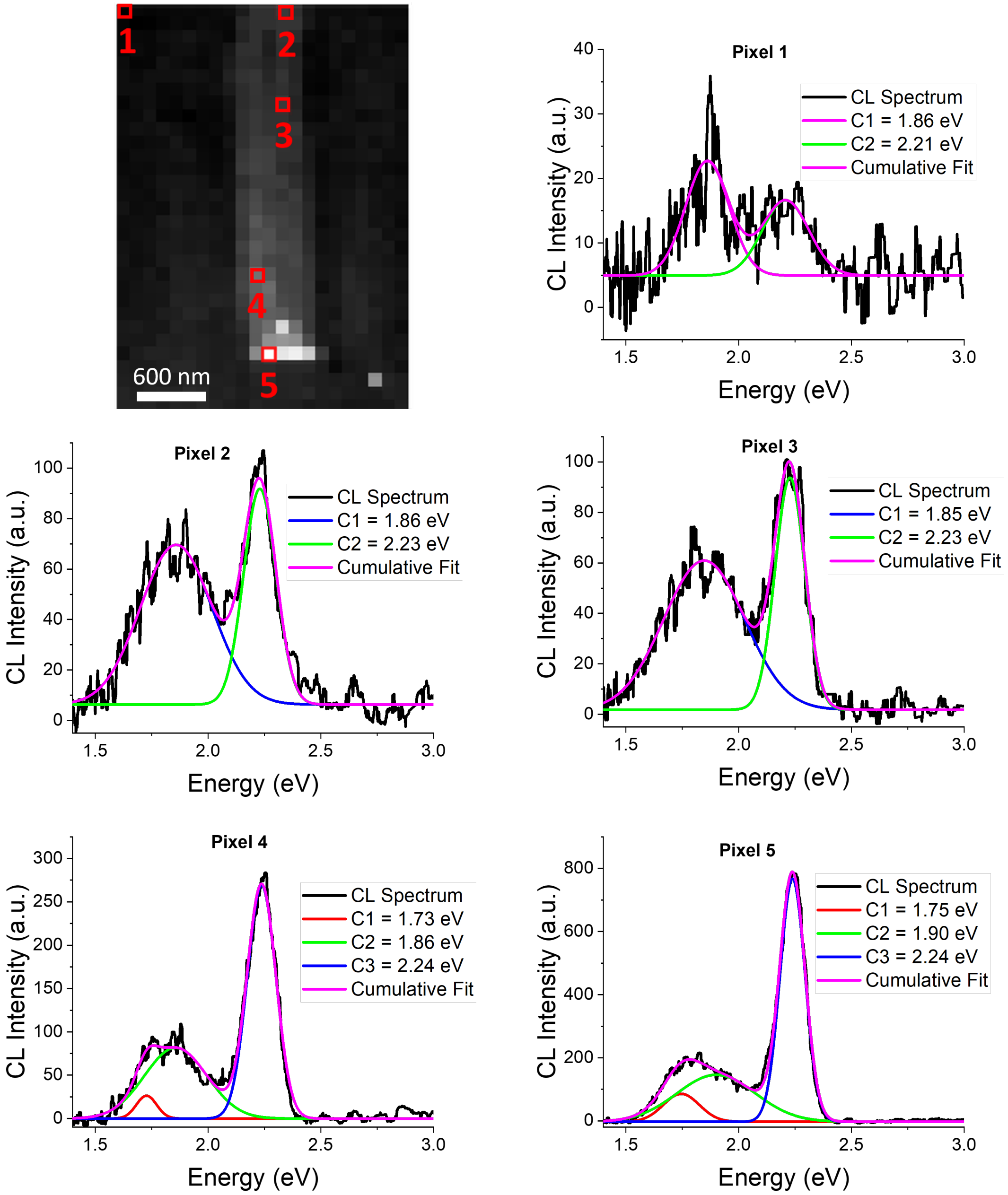

Figure 3.10: CL performed at 85 K for an alloy nanowire with nominal composition $x = 0.10$. SEM image of alloy nanowire has Pixels 1-5 denoted by red squares. The corresponding CL spectra are processed with a percent filter function and fitted with Gaussian functions.

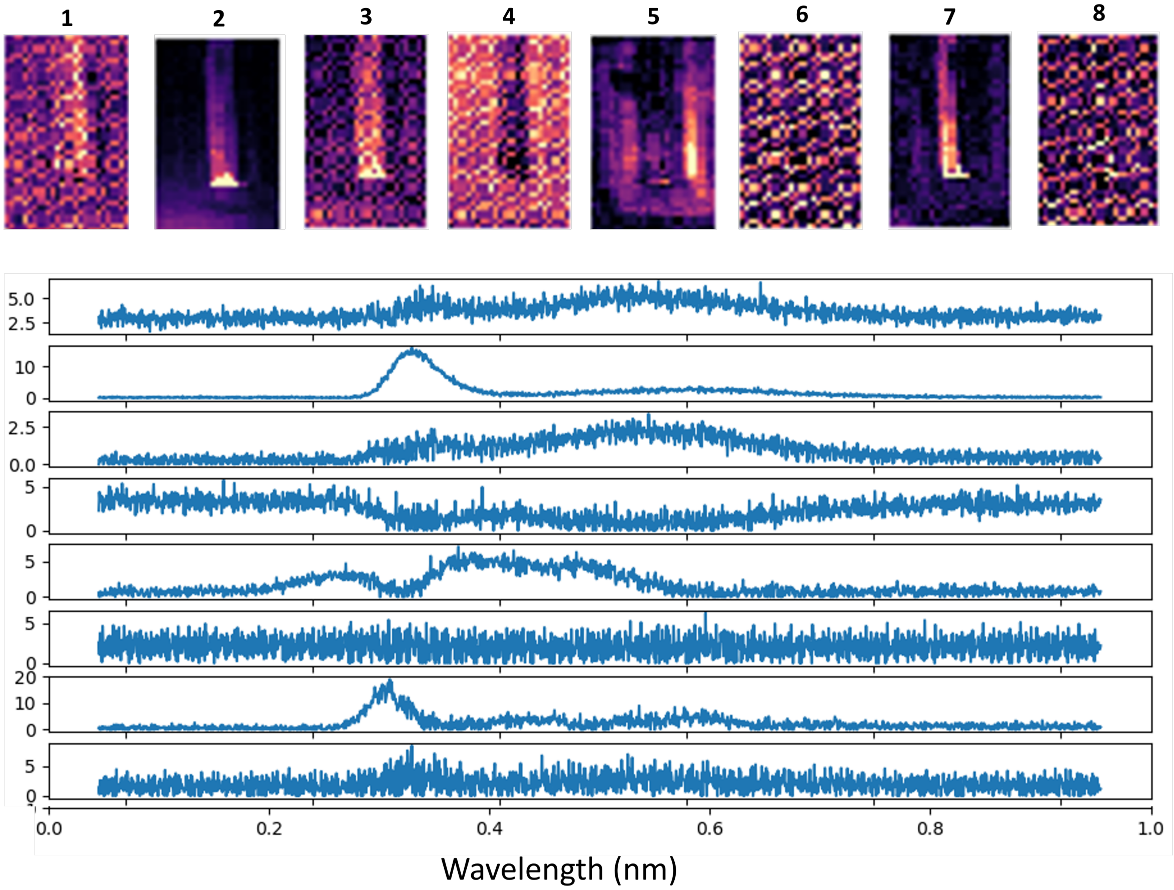

Figure 3.11: Different components generated by PCA analysis from a CL map containing alloy nanowire in Figure 3.10. Component 2 best represents the luminescence from the alloy nanowire.

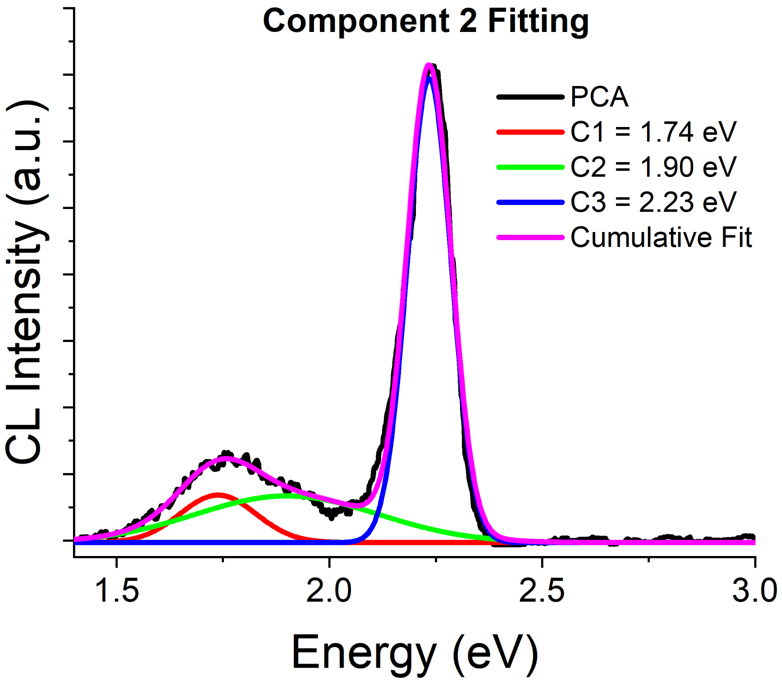

Figure 3.12: Gaussian fitting of PCA Component 2.

3.3 Band Structure Model for $\mathbf{GaS_{1-x}Te_x}$ Nanowires

In this section, a band structure model is proposed for the $\mathrm{GaS}_{1-x}\mathrm{Te}_x$ nanowires. The model is based on three assumptions derived from the Raman, PL, and CL data presented thus far. The first assumption is that there exist two polytypes, β and ϵ, within a $\mathrm{GaS}_{1-x}\mathrm{Te}_x$ nanowire. The second assumption is that the tellurium impurity band causes a restructuring of the GaS band structure, as it is expected for highly mismatched alloys. The third assumption is that indirect exciton transitions occur at room-temperature in the $\mathrm{GaS}_{1-x}\mathrm{Te}_x$ nanowires.

The first assumption is based on the Raman spectroscopy data shown in Figure 2.12 and the PL data shown in Figure 3.9. The Raman active modes of GaS red shift with the addition of tellurium. This red shift shows that the tellurium is indeed being alloyed into the GaS matrix. As the tellurium composition increases, the A_{1g}^1 splits into two different modes. The splitting of the A_{1g}^1 could be evidence of the two polytypes forming as tellurium is incorporated into the GaS matrix. Similarly, two PL peaks are present with sub-band gap excitation, possibly from two different polytypes. Finally, the coexistence of two polytypes within a similar alloy system has been shown for the $\mathrm{GaS}_{1-x}\mathrm{Se}_x$ system [114].

The second assumption is based on the CL measurements showing a high-intensity peak near 2.23 eV that is lower in energy from the reported band gap of GaS, and on the DFT calculations that will be presented in the next chapter. Due to the high-energy of the electron beam in CL measurements, carriers can be excited across the direct band gap of the material. Consequently, the 2.23 eV CL peak is attributed to the direct band gap of the alloy nanowire with nominal composition of $x = 0.10$. This would imply a 0.63 eV reduction in the reported direct band gap of GaS.

The third assumption is based on the high-intensity, room-temperature PL observed for the $\mathrm{GaS}_{1-x}\mathrm{Te}_x$ nanowires. The PL spectra from the 488 nm laser line displays three peaks near 1.42 eV, 1.55 eV, and 1.91 eV. The highest intensity peaks are those near 1.42 eV and 1.55 eV. Sub-band gap PL with a 660 nm laser line further confirmed the presence of PL peaks near 1.38 eV and 1.52 eV, supporting the assumption that these transitions originate from indirect band excitons, as opposed to deep defect levels.

Therefore, in this band model, two types of transitions can occur, as shown in Figure 3.13. In the first type of transition, the high-energy electron beam from the CL excites carriers across the direct band gap of the alloy nanowire. This transition corresponds to the high-intensity CL peak located at 2.23 eV. The second type of transition that occurs is the indirect exciton transition. Each of the two high-intensity, PL peaks is attributed to an indirect exciton transition from a different polytype. The higher energy PL peak located at 1.55 eV is attributed to the indirect exciton transition in the β-GaS polytype while the lower energy PL peak located at 1.42 eV is attributed to the indirect exciton transition in the ϵ-GaS polytype. These attributions were made based on the work by Ho *et al.* [114], in which the ϵ donor level is lower in energy than the β-GaS conduction band, as depicted in Figure 5.1. The intermediate energy peaks observed in the PL and CL spectra are attributed to structural defects, such as sulfur interstitials and gallium vacancies.

Further experiments need to be performed to test the validity of this model, such as performing PL on nanowires with nominal compositions of $x < 0.03$ to confirm whether there is indeed the formation of an impurity band and two polytypes. Moreover, performing low-temperature PL could elucidate on the nature of the PL peaks observed at room-temperature. Finally, as will be discussed in more detail in Chapter 5, performing TEM perpendicular to the basal plane of the c-axis nanowire could confirm the presence of polytypes in the system.

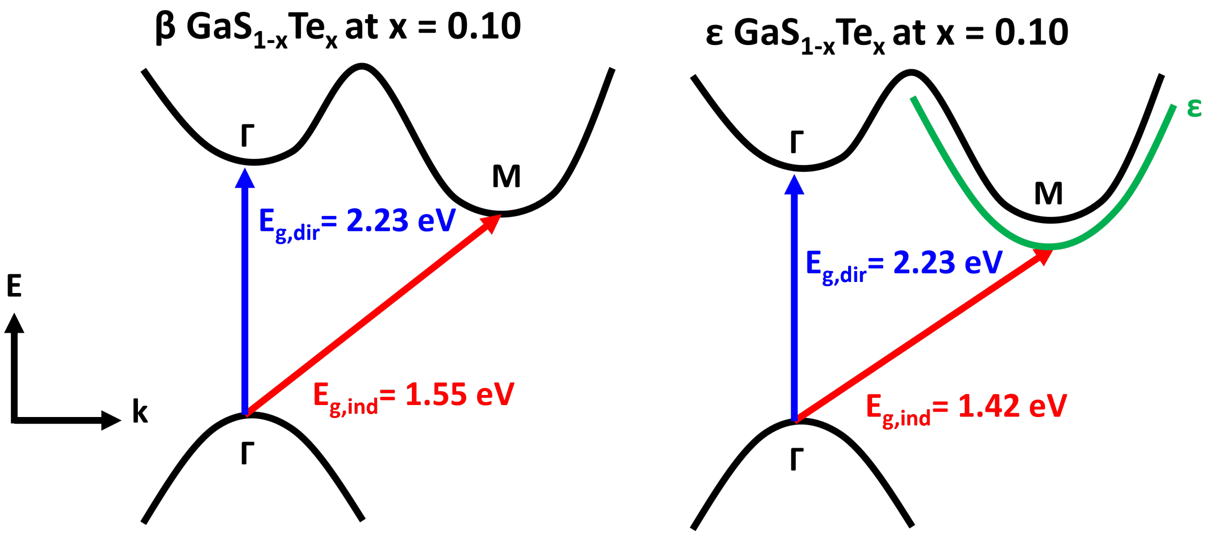

Figure 3.13: Schematic of band structure model for the $GaS_{1-x}Te_x$ alloy nanowires.

3.4 Summary

In this chapter, sulfur-rich, $GaS_{1-x}Te_x$ alloy nanowires were characterized using PL and CL spectroscopy. Specifically, the room-temperature PL spectrum of a pure GaS nanobelt measured with a 488 nm laser line was shown to have two peaks located near 1.7 eV and 1.9 eV. The origin of these PL peaks is attributed to structural defects, such as sulfur interstitials and gallium vacancies.

Furthermore, the room-temperature PL of alloy nanowires measured with a 488 nm laser line showed three peaks located near 1.42 eV, 1.55 eV, and 1.91 eV. The PL peaks do not shift significantly in energy with nominal tellurium composition. This can be explained by the presence of a miscibillity gap that prevents tellurium atoms from substitutionally incorporating above a certain composition. Measurements with sub-band gap excitation energy of 660 nm further confirm the presence of peaks near 1.38 eV and 1.52 eV, increasing the likelihood that the origin of one of these PL peaks is from a fundamental band gap transition rather than deep defects states. Additionally, CL measurements of an alloy nanowire with nominal composition of $x = 0.10$ show that the spectrum has three peaks located at 1.74 eV, 1.90 eV, and 2.23 eV.

Finally, a band structure model is proposed to reconcile the luminescence peaks observed in the PL and CL measurements, as well as the Raman modes presented in Chapter 2. In this model, the GaS band structure changes with the addition of the tellurium impurities, reducing the band gap of the material as the tellurium composition increases. The direct band gap of the alloy nanowire is observed from CL measurements. Furthermore, the β and

ϵ polytpes coexist within the $\mathrm{GaS}_{1-x}\mathrm{Te}_x$ nanowires, causing two possible indirect exciton transitions, one for each polytype, observed in PL measurements.

Chapter 4

DFT Calculations of the $\mathrm{GaS}_{1-x}\mathrm{Te}_x$ Alloy System

In this chapter, a brief introduction to density functional theory (DFT) is given in Section 4.1. In Section 4.2, DFT calculations of the $\mathrm{GaS}_{1-x}\mathrm{Te}_x$ alloy system using the HSE and PBE functionals are presented in regards to the band gap dependency with tellurium composition, energy differences between different GaS polytypes, direct band gap and alloy band gap differences as a function of tellurium composition, and the density of states for different tellurium compositions.

4.1 Introduction to Density Functional Theory (DFT)

Density functional theory (DFT) is a modeling method that can be used to calculate the electronic structure of materials by finding solutions to the Schrödinger equation [147, 148]. The Schrödinger equation is a partial differential equation that predicts the behavior of particles in a quantum system over time [148]. A familiar form of the Schrödinger equation is the time-independent, non-relativisitc form $H\psi = E\psi$, where H is the Hamiltonian operator, ψ is a set of eigenstates, or solutions, of the Hamiltonian, and E is a set of eigenvalues that satisfy the equation [147]. For the problem of multiple electrons interacting with multiple nuclei, the Schrödinger equation includes terms that represent the electron kinetic energy, the electron-nuclei interactions, and the interaction among electrons [147]. In this case, ψ is the electron wave function and E is the ground-state of the electrons. The wave function in Schrödinger's equation contains all the information of the quantum system and therefore is used to calculate the total energy of atoms, for instance. However, in 1927, Llewellyn Thomas and Enrico Fermi showed atomic calculations that used the electron density rather than the wave function as the fundamental variable [148]. Subsequently, two theorems developed by Pierre Hohenberg and Walter Kohn helped lay the foundation of the field of DFT. Before stating the theorems, it is important to define what a functional is. A functional is a function that takes in a function as input and gives a number as the output [148]. In the case of a density functional, the functional takes in the electron density as the input and yields an energy as the output [148].

The first of the Hohenberg-Kohn theorems states that “the ground-state energy from Schrödinger’s equation is a unique functional of the electron density” [147]. In other words, there is a one-to-one mapping between the ground-state wave function and the ground-state electron density, and therefore the ground-state electron density determines the ground-state energy of the system [147]. This theorem is important because the Schrödinger equation can be solved by finding a function of three spatial variables (i.e. the electron density) as opposed to a function of 3N variables (i.e. the wave function), where N is the number of electrons [147]. The second Hohenberg-Kohn theorem states that “the electron density that minimizes the energy of the overall function is the true electron density corresponding to the full solution to the Schrödinger equation” [147]. This theorem is important because it states that the energy of the functional can be minimized by varying the electron density to find the ground-state electron density, and once the ground-state electron density is known, other properties can be calculated [149].

In 1965, Walter Kohn and Lu Jeu Sham further developed the field of DFT by developing the Kohn-Sham equations that allow the electron density to be found by solving a set of equations in which each equation involves a single-electron wave function [147, 149]. In the Kohn-Sham equations, there are three potentials: the first potential describes the interaction between an electron and the nuclei, the second potential describes the Coulombic repulsion between electrons included in the Kohn-Sham equations and the total electron density (this is known as the Hartree potential), and the third potential describes all the interactions not described by the first two potentials (this is known as the exchange-correlation potential) [147, 149]. The nature of the exchange-correlation potential is not known, but there are a number of approximations, such as local density approximation (LDA) and generalized gradient approximation (GGA), that can be used to specify this potential.

A big-picture description of the iterative process used to find the electron density is described by Sholl *et al.* [147] in the following steps:

1. Define a trial electron density.
2. Solve the Kohn-Sham equations to find the single electron wave function.
3. Calculate the electron density defined by the single-electron wave function found in Step 2.
4. Compare the calculated electron density in Step 2 with the initial, trial density in Step 1. If the two densities are the same, then this is the ground-state electron density. If

the two electron densities are not the same, then the trial electron density must be updated and the process is repeated.

To summarize, finding the ground-state of the Schrödinger equation is very difficult because it's a many-body problem [147]. However, the ground state can be found by minimizing the electron density functional [147]. The Kohn-Sham equations allow for the ground state to be found by solving a a set of equations, with each equation involving a single-electron wave function. To solve Kohn-Sham equations, the exchange-correlation potential must be specified, and approximations, such as LDA and GGA, can be used to do so. Overall, the advantage of DFT calculations compared to other calculations, such as Hartree-Fock (HF) calculations, is that it only requires computation of the total electron density, which only consists of three spatial variables, and, unlike the wave function, is experimentally observable [148]. Consequently, DFT can provide, in some cases, higher accuracy than HF calculations at a lower computational cost [148]. For a more in-depth introduction to DFT, the reader is referred to Reference [147].

4.2 DFT of the $GaS_{1-x}Te_x$ Alloy System

In this dissertation, calculations using DFT were performed by Dr. Matthew Horton for the $GaS_{1-x}Te_x$ alloy system using the Vienna Ab Initio Simulation Package (VASP) [150, 151] and the Perdew-Burke-Ernzerhof (PBE) [152] and Heyd-Scuseria-Ernzehof (HSE) [153] exchange-correlation functionals. A detailed description of the calculation methods is given in Appendix E. In general, the PBE functional provides improved coverage of k-space for the same amount of computation. However, the PBE functional underestimates the value of band gaps. On the other hand, the HSE functional is more computationally expensive but offers a more accurate prediction of the band gap energies.

4.2.1 Energy versus Tellurium Composition

For DFT calculations with the HSE functional, the band gap of GaS was shown to decrease from 2.96 eV to 2.47 eV, a 0.49 eV decrease in energy, with the addition of $x = 0.06$ tellurium. For DFT calculations with the PBEsol [154] functional, the band gap of GaS changed from 2.12 eV to 1.64 eV, a 0.48 eV decrease in energy, with tellurium composition of $x = 0.06$. Therefore, both calculations agree that there is a decrease in the band gap energy of GaS of nearly 0.50 eV when $x = 0.06$ tellurium is added to the GaS host matrix.

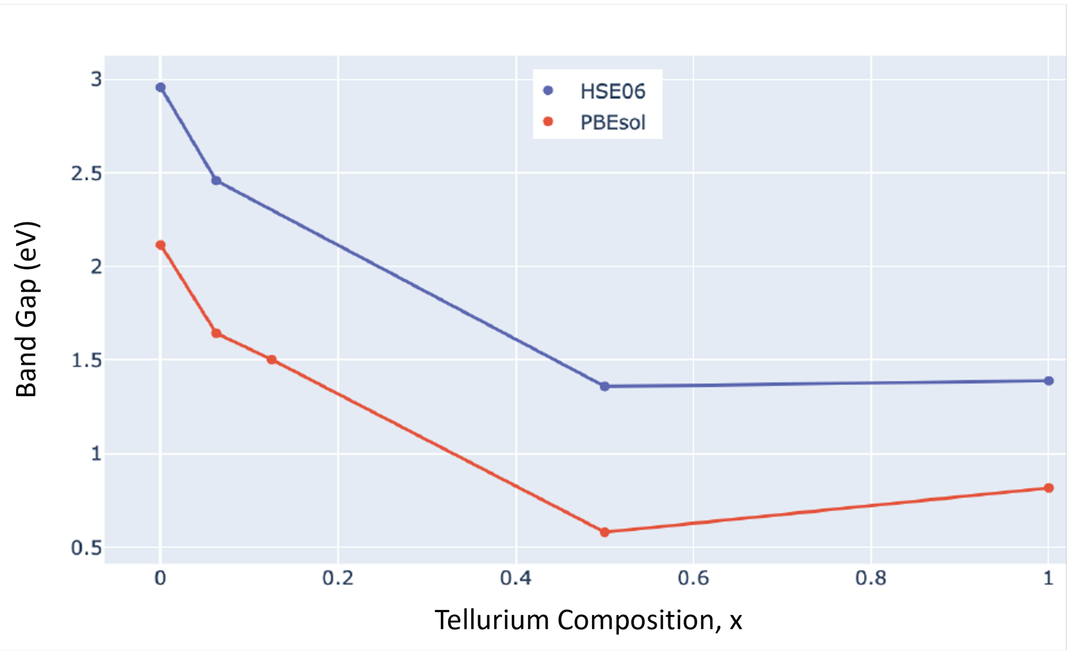

Figure 4.1: DFT calculations of the band gap versus tellurium composition of the $\mathrm{GaS}_{1-x}\mathrm{Te}_x$ alloy system performed with the HSE and PBEsol functionals.

A second set of calculations were performed using the generalized quasi-chemical approximation (GQCA) [155, 156]. In this method, a larger number of smaller cells of 16 atoms are used. Using a larger number of cells allows for statistical averages and, consequently, smoother plots. The GQCA method is still performed with the PBE functional, and therefore the band gap is systematically underestimated. Figure 4.2a shows the alloy band gap versus tellurium composition at different temperatures. The trend shows that there is a bowing that occurs as the tellurium composition increases. Furthermore, the inset in Figure 4.2a shows a phase diagram for the $\mathrm{GaS}_{1-x}\mathrm{Te}_x$ system generated by the GQCA method. The red region in the phase diagram represents where the system is predicted to have a miscibility gap, the blue region represents where the phase will be metastable, and the outer regions represent where the phases are thermodynamically stable. Note that the horizontal line in the phase diagram is likely spurious due to the solver used. Finally, Figure 4.2b shows the energy difference between the direct band gap and the alloy band gap as a function of composition for different temperatures. The energy difference approaches zero with increasing tellurium composition, reaching a minimum at tellurium composition near $x = 0.50$. Note that the actual minimum of the energy difference curve is likely zero, but the curve appears to only approach zero because some non-zero configurations are still included in the ensemble due to the statistical nature of the method used.

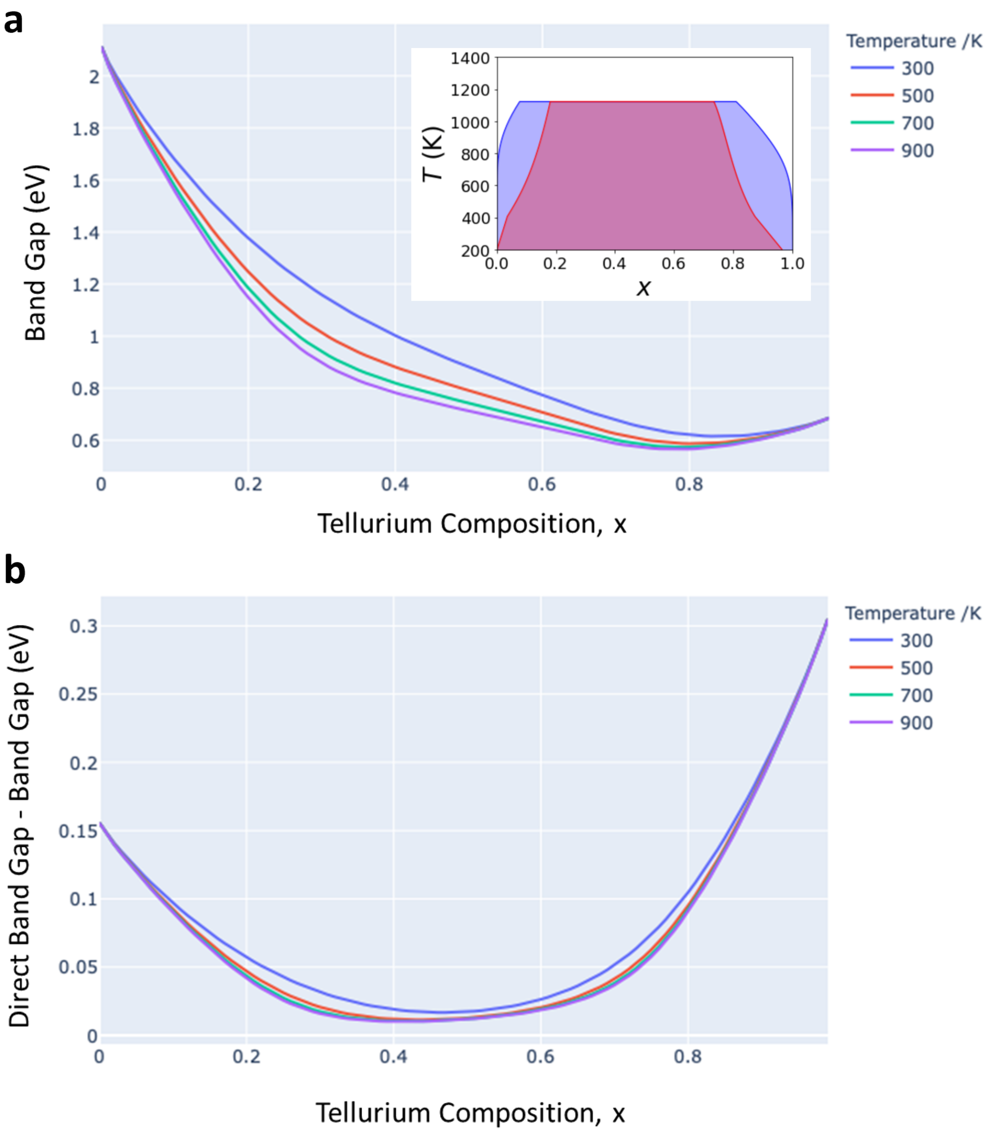

Figure 4.2: DFT calculations performed with the GCQA method. (a) Band gap versus tellurium composition. The inset is the phase diagram for the $\mathrm{GaS}_{1-x}\mathrm{Te}_x$ system. The red region is where the system is predicted to have a miscibility gap, the blue region is where the phase will be metastable, and the outer regions are where the phase is thermodynamically stable. (b) Energy difference between the direct band gap and the alloy band gap.

4.2.2 Band Structures for GaS Polytypes

The band structures for β-GaS (space group: $P6_3/mmc$) and ϵ-GaS (space group: $P\overline{6}m2$) were calculated to investigate energy changes due to stacking sequence, as shown in Figure 4.3. For β-GaS, the conduction band minimum was located at the M-point with energy 4.98 eV and the valence band maximum was located between the K and Γ-points with energy 2.03 eV. The direct and indirect band gaps were calculated to be 3.36 eV and 2.96 eV, respectively. For ϵ-GaS, the conduction band minimum is located at the M-point with energy 5.05 eV and the valence band maximum is located between the K and Γ-points with energy 2.04 eV. The direct and indirect band gaps were calculated to be 3.39 eV and 3.01 eV, respectively. The difference in the direct and indirect band gaps between β-GaS and ϵ-GaS are 0.03 eV and 0.04 eV, respectively. Therefore, there are no significant differences in the calculated band structure between the β and ϵ GaS polytypes.

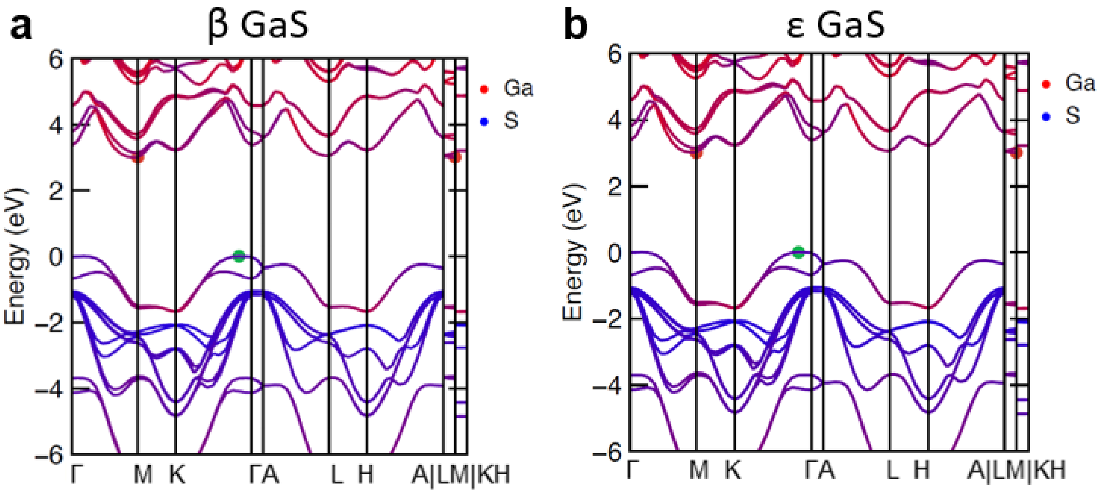

Figure 4.3: Calculated band structures for (a) β-GaS and (c) ϵ-GaS polytypes.

4.2.3 Density of States

The density of states for the $GaS_{1-x}Te_x$ alloy system were also calculated with the PBE functional for compositions $x = 0$, $x = 1/16$ (0.06), $x = 1/8$ (0.13), and $x = 1/2$ (0.50), as shown in Figure 4.4a-d, respectively. The density of states is defined as the number of allowed states per unit energy in the energy range between E and $E + \delta$ per unit volume [1]. Thus, the plots show that the density of states in the valence band experiences the effects of tellurium incorporation more strongly than the conduction band and that the system undergoes a decrease in the band gap with the addition of tellurium.

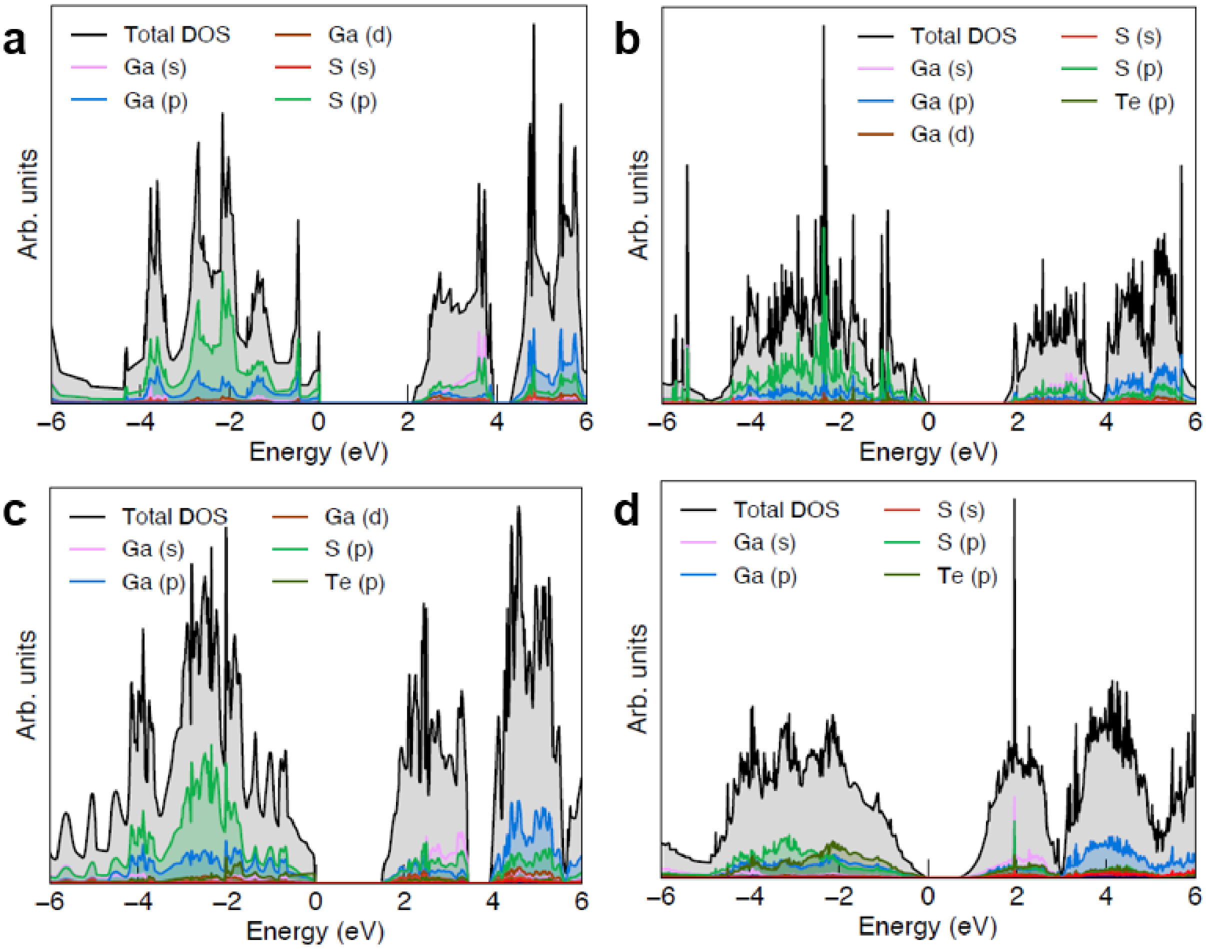

Figure 4.4: Calculated density of states for the GaS$_{1-x}$Te$_x$ alloy system with compositions (a) $x = 0$, (b) $x = 1/16$ (0.06), (c) $x = 1/8$ (0.13), and (d) $x = 1/2$ (0.50).

4.3 Summary

In this chapter, DFT calculations of the GaS$_{1-x}$Te$_x$ alloy system were presented to compliment the optical characterization discussed in Chapter 3. First, DFT calculations showed that the band gap energy differences between the β and ϵ polytypes of GaS are small ($E_g < 0.05\,\text{eV}$).

Second, DFT calculations demonstrated that the density of states in the valence band experiences the effects of tellurium more strongly than the conduction band. Third, similar to experimental data from PL measurements presented in Chapter 3, DFT calculations displayed an energy decrease from the band gap of pure GaS with the addition of tellurium. Additionally, calculations performed with the GCQA method further confirmed the non-linear behavior of the band gap with tellurium composition. It is important to highlight that the bowing shown by the $\mathrm{GaS}_{1-x}\mathrm{Te}_x$ alloy system in Figure 4.2a is more prominent than the bowing shown by the $\mathrm{GaSe}_{1-x}\mathrm{Te}_x$ alloy system [68, 69] in Figure 1.5. This large bowing is consistent with the behavior of highly-mismatched alloys. The origin of the large bowing can be explained in the framework of the band anti-crossing model [122, 157]. The bowing originates from the large differences in atomic size and electronegativity between sulfur and tellurium. As the tellurium incorporates into the GaS matrix, the tellurium impurity level forms close to the valence band, as shown in the density of states plots in Figure 4.4. With increasing tellurium incorporation, a tellurium impurity band forms and it hybridizes with the valence band, forming and E_+ and E_- energy bands.

Fourth, the phase diagram generated using the GQCA method indicates that there is a miscibility gap in the $\mathrm{GaS}_{1-x}\mathrm{Te}_x$ alloy system as well a metastable phase at room-temperature. This predicted miscibility gap is consistent with the explanation presented in Chapters 2 and 3 regarding the Raman modes and PL peak positions staying virtually constant with tellurium composition $x > 0.03$. In this explanation, the alloy system has a solubility limit, after which tellurium is not substitutionally incorporated, but likely intercalated.

Finally, the energy difference between the direct and alloy band gaps is predicted to approach zero near tellurium composition of $x = 0.50$. These calculations elucidate on the interplay between optical properties, composition and crystal structure for mismatched, layered materials.

Chapter 5

Conclusion and Future Work

5.1 Conclusion

In conclusion, sulfur-rich, $GaS_{1-x}Te_x$ alloy nanostructures were synthesized for the first time. The synthesis consisted of a gold-catalyzed, vapor transport method. The dominant growth mechanism for alloy nanowires is the vapor-liquid-solid growth mechanism as evidenced by the presence of catalyst droplets at the end of the wires and by the large ratio of the length to width of the alloy nanowires. Furthermore, the growth direction of GaS nanobelts is perpendicular to the c-axis while the growth direction of sulfur-rich, alloy nanowires is parallel to the c-axis. This change in growth direction is hypothesized to originate from the edge growth passivation by tellurium atoms. Due to the larger atomic radius, tellurium atoms at the edges might bind to other tellurium atoms, forming a lower energy and less chemically reactive edge. C-axis nanowires offer new and exciting opportunities for sensor technologies due to the dangling bonds decorating the nanowire.

In addition to the changes in growth direction, the alloy nanowires show an initial red shift in the Raman-active modes from GaS Raman-active modes with tellurium incorporation. As the tellurium composition continues to increase, the Raman-active modes do not continue to shift significantly. This behavior might be indicative of a tellurium solubility limit in the $GaS_{1-x}Te_x$ alloy system. It is possible that the tellurium is being incorporated interstitially or intercalted, instead of substitutionally incorporated. Finally, the splitting of the A^1_{1g} mode into two modes is proposed to be due to the presence of S-Ga-Ga-S and S-Ga-Ga-Te domains within the crystal or to the different stacking sequence, β or ϵ, within each cell configuration.

Sulfur-rich, alloy nanowires also showed a strong PL signal at room-temperature and CL signal at 85 K. A band model was proposed to reconcile the PL and CL data. In this model, two types of transitions can occur. In the first type of transition, CL excites carriers across the direct band gap of the alloy nanowire. This transition corresponds to the high-intensity CL peak located at 2.23 eV. The second type of transition that occurs is the indirect exciton transition. Each of the two high-intensity, PL peaks is attributed to an indirect exciton transition from a different polytype. The higher energy PL peak located at 1.55 eV is attributed to the indirect exciton transition in the β-GaS polytype while the lower energy PL peak located at 1.42 eV is attributed to the indirect exciton transition in the ϵ-GaS polytype. Overall, the environmental stability and strong luminescence in the near infra-red region of the $\mathrm{GaS}_{1-x}\mathrm{Te}_x$ alloy nanowires makes this material system a promising candidate for optoelectronic applications, such as photodetectors.

DFT calculations showed that the $\mathrm{GaS}_{1-x}\mathrm{Te}_x$ alloy system indeed has a non-linear dependency with tellurium composition and that there is a pronounced decrease in energy with a few percent of tellurium incorporation, typical of a highly mismatched alloy. Moreover, calculations using the GQCA method predicted that there is a miscibility gap as well as a metastable phase in the $\mathrm{GaS}_{1-x}\mathrm{Te}_x$ alloy system. The presence of a miscibility gap in the calculated phase diagram is consistent with the observation that the Raman modes and PL peak energies follow a flat trend with increasing tellurium composition as a result of a solubility limit being reached. These calculations contribute to the foundation for studying layered materials that are highly mismatched that possessing diffent crystal structures and polytypes.

Finally, the future work outlined in the next section seeks to further elucidate on the alloy formation of layered nanowires and on the band structure model of the $\mathrm{GaS}_{1-x}\mathrm{Te}_x$ alloy system. In particular, elucidating on the alloy formation of c-axis, layered nanowires could lead to novel nanowires with mixed growth direction, potentially opening the door to novel and exciting applications in carrier transport in layered nanowires. Finally, investigating the presence of different polytypes in the alloy nanowires will be instrumental to further develop a model for the electronic structure of the $\mathrm{GaS}_{1-x}\mathrm{Te}_x$ alloy system and layered nanowires in general.

5.2 Future Work

The $\mathrm{GaS}_{1-x}\mathrm{Te}_x$ system has been shown to have environmental stability, c-axis growth direction, and strong luminescence in the infra-red region. However, important questions remain to be answered for the synthesis, growth, and properties for the $\mathrm{GaS}_{1-x}\mathrm{Te}_x$ alloy system. In this section, the next steps for this project are discussed to address these questions; in particular, the tuning of the nanowire size and morphology and the stacking sequence determination of the alloy nanowires.

5.2.1 Achieve Higher Control of Nanowire Size

Achieving control of the size of materials is key to characterize and engineer their optoelectronic properties. For example, by growing crystals with at least one physical dimension approaching the exciton Bohr radius, quantum confinement effects can be induced. In general, the size and morphology of nanowires have been shown to be determined by growth parameters such as time, catalyst size, and growth temperature. In this section, each of this parameters is discussed for future experiments.

Growth time is an important parameter that can be tuned to control the size of nanowires. As shown in Appendix F, preliminary work on understanding growth time was performed with sulfur-rich alloy nanowires by undergraduate researcher Andre Palacios in our research group. In particular, an alloy growth was performed that was three hours long, as compared to the half an hour growths studied previously in this dissertation. As expected, increasing the growth time results in a larger cross-sectional area and longer nanowires along the fast-growth direction. Synthesizing larger nanostructures offers some characterization benefits. For example, electron backscatter diffraction (EBSD), a technique with simpler sample preparation requirements than TEM, can be used to characterize the crystal structure and growth direction of these larger nanostructures. Another example of a characterization benefit of larger nanostructures is that their chemical composition can be more accurately characterized through EDS due to the larger excitation volume of the nanowire. Finally, a group of larger nanostructures might allow for micro-absorption measurements to further confirm the optical properties of the alloy crystals.

The catalyst size is another essential parameter to control nanowire size and therefore its properties. For example, tuning the catalyst diameter to be on the order of the exciton Bohr radius could allow for quantum confinement effects to be observed in the nanowires. Furthermore, an alloy nanowire with a smaller cross-section would allow for a higher amount of stress to be accommodated through lateral relaxation, possibly allowing for nanowires with higher tellurium compositions to be synthesized. Finally, nanowires with smaller cross-sections would allow for higher-quality, crystallographic characterization by TEM.

5.2.2 Elucidate on the Alloy Nanowire Growth Mechanism

Understanding the growth mechanism of alloy nanowires is imperative to attain a high degree of compositional, morphological and structural control. Important parameters that affect the growth mechanism are the temperatures of the source materials, which controls the flux, and the temperature of the substrate, which controls absorption and diffusion of atoms into the nanowire. The nanowires presented in this dissertation were synthesized in a single-zone furnace. This limited the range of temperatures accessible for the substrate and sources as well as the accuracy and reproducibility of the experiments.

Currently, our laboratory is setting up a programmable, three-zone furnace, with the temperature in each zone ranging from room-temperature to 1200 °C. This experimental set up will allow for a wider range of temperature differentials (i.e. temperature differences among the substrate, GaS and GaTe powders) to be explored compared to the single-zone furnace experimental set up. Additionally, having independent heaters for each zone will ensure temperature homogeneity within each zone, allowing for higher compositional homogeneity within each growth. Finally, because the temperatures of the substrate and sources can be controlled more gradually, accurately and independently, experiments that test the role of tellurium in the growth can be designed. For example, by gradually tuning the temperature of the tellurium source, a more systematic study of the post-growth, tellurium composition in the catalyst droplet and the growth direction of the nanowire can be conducted.

Understanding the growth mechanism of the $\mathrm{GaS}_{1-x}\mathrm{Te}_x$ alloy system could enable the engineering of novel nanostructures. For example, by finding the exact threshold temperature for the growth direction of the alloy nanowire to switch from perpendicular to the c-axis to parallel to the c-axis, engineering mixed growth direction nanostructures could be possible. Specifically, by cycling the tellurium source temperature above and below the threshold for c-axis growth could result in a nanowire whose growth direction oscillates between parallel and perpendicular to the c-axis. Studying the optical and transport properties in such mixed growth direction nanowires would be scientifically and technologically exciting.

5.2.3 Stacking Sequence Determination

Determining the stacking sequence of the $\mathrm{GaS}_{1-x}\mathrm{Te}_x$ alloy nanowires is necessary to understand their optical properties. As reported by Ho *et al.*, the β-GaS matrix has ϵ stacking faults that cause a defect level to form at the Γ point 2.4 eV from the valence band, as shown in Figure 5.1. This defect level shifts to lower energies as the selenium content increases for the $\mathrm{GaSe}_{1-x}\mathrm{S}_x$ alloy system.

Similar to the $\mathrm{GaSe}_{1-x}\mathrm{S}_x$ alloy crystals, it is possible that the $\mathrm{GaS}_{1-x}\mathrm{Te}_x$ alloy nanostructures in this work also possess stacking fault defects that dominate the optical transitions. In fact, the splitting of the A^1_{1g} Raman-active mode into two modes with nominal tellurium composition of $x = 0.04$ could be an indication of different polytypes present in the alloy nanowire. A possible way to unambiguously determine the stacking sequence in the nanowires synthesized in this work is by performing TEM on a thin cross-section of the alloy nanowire with the electron beam perpendicular to the basal plane of the cross-section. To isolate a thin cross-section of the nanowire, a sonication-assisted liquid exfoliation process could be used, as shown in Figure 5.2. In this process, the alloy nanowires could be submerged into a solvent and sonicated to break the van der Waal bonds. This would result in cross-sections of alloy nanowires with different thicknesses to be dispersed in the solution. The dispersed cross-sections can then be drop casted onto a TEM grid.

Using TEM to identify different polytypes has been performed by Shevitski *et al.* [158] for $\mathrm{GaSe}_{1-x}\mathrm{S}_x$ alloy crystals, as shown in Figure 5.3. In their work, Shevitski *et al.* performed HR-STEM on a $\mathrm{GaSe}_{1-x}\mathrm{S}_x$ alloy crystal with sulfur content of $x \approx 0.75$ and a pure GaSe crystal to unambiguously discern between the ϵ and β stacking phases. As shown in Figure

5.3c and g, the HR-STEM images show a clear difference in contrast based on the ϵ and β stacking phases present in the crystals, with the β stacking phase showing a clear honeycomb lattice and the ϵ stacking phase showing spots at the center of each hexagon.

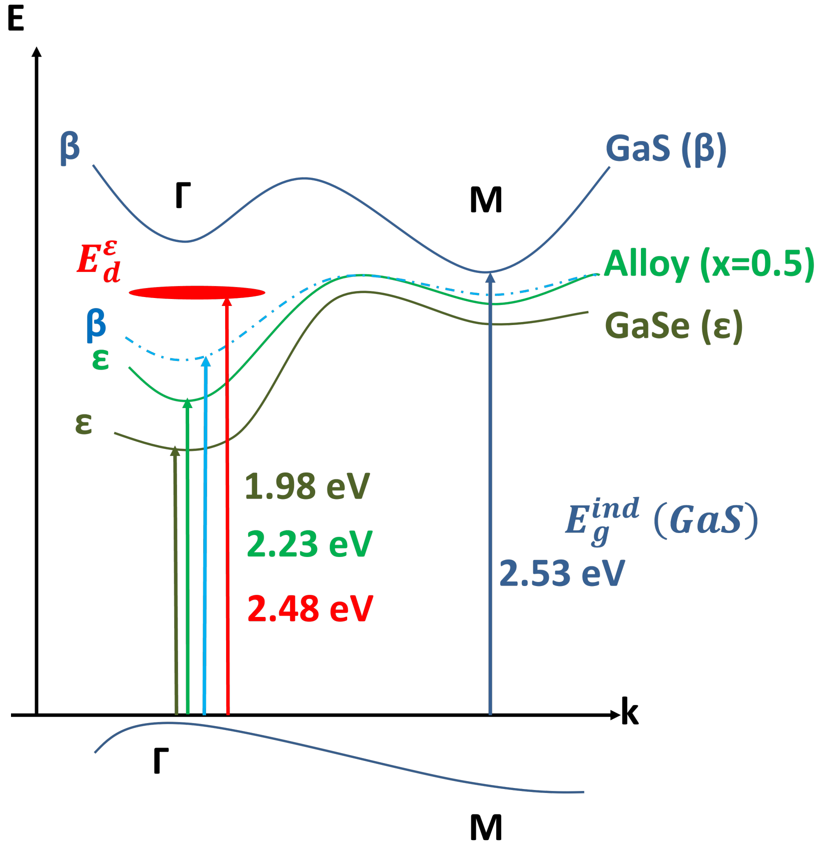

Figure 5.1: Schematic of band transitions for the $GaSe_{1-x}S_x$ alloy system. A donor defect level forms close to the Γ point in the conduction band as a result of stacking fault defects in the β-GaS matrix. As selenium is incorporated into the β-GaS matrix, the ϵ defect level shifts to lower energy. Figure adapted from [114]

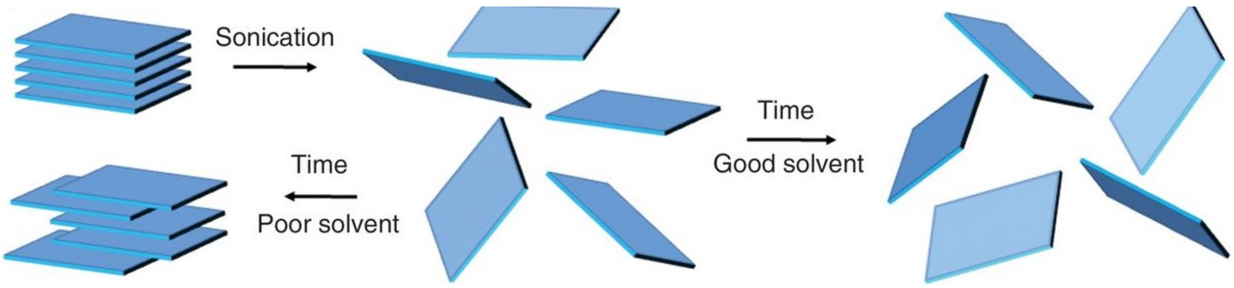

Figure 5.2: Schematic of sonication-assisted liquid exfoliation. The layered material is sonicated in a solvent to break the van deer Waals bonds and form nanosheets. "Good solvent" is defined as a solvent that prevents reaggregation while bad solvent allows for reaggregation and sedimentation. Image from [159]

.

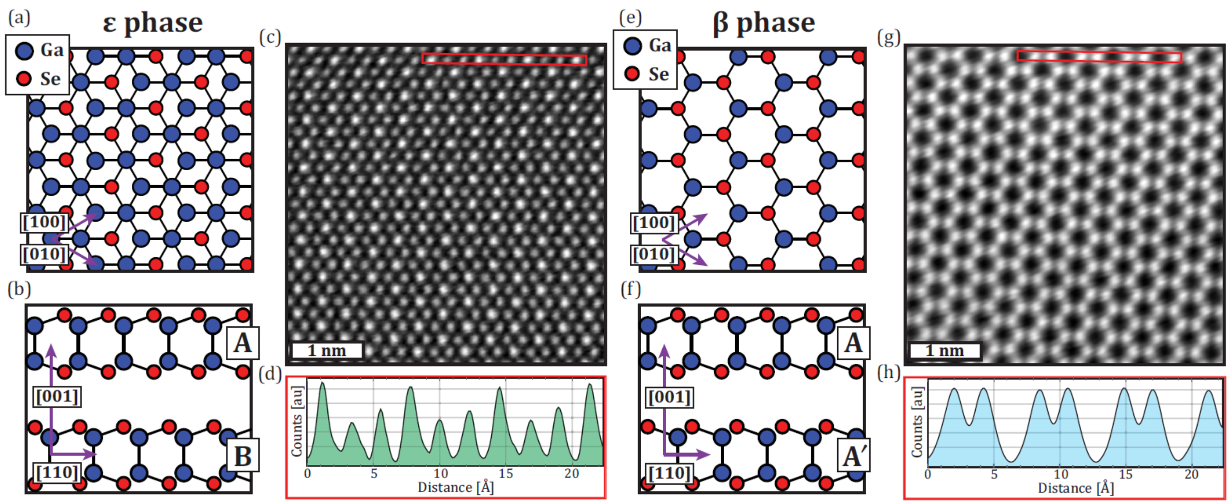

Figure 5.3: (a, b) Schematic of the ϵ stacking phase from different crystallographic orientations. (c) HR-STEM of an $GaSe_{1-x}S_x$ alloy crystal with sulfur content of $x \approx 0.75$ and ϵ stacking phase. (d) Plot of the intensity from the red rectangle in (c). (e-h). Analogous images as in (a-d) for a pure GaSe crystal with β stacking phase. Image from [158].

Bibliography

1. Yu, P. Y. & Cardona, M. *Fundamentals of semiconductors: physics and materials properties* 4th ed. 1 p. ISBN: 978-3-642-00710-1 (Springer, Berlin ; London, 2010).
2. Novoselov, K. S. *et al.* Electric Field Effect in Atomically Thin Carbon Films. *Science* **306,** 666–669. ISSN: 0036-8075, 1095-9203 (Oct. 22, 2004).
3. Geim, A. K. & Novoselov, K. S. The rise of graphene. *Nature Materials* **6,** 183–191. ISSN: 1476-1122 (Mar. 2007).
4. Novoselov, K. S. *et al.* Two-dimensional gas of massless Dirac fermions in graphene. *Nature* **438.** Number: 7065 Publisher: Nature Publishing Group, 197–200. ISSN: 1476-4687 (Nov. 2005).
5. Castro Neto, A. H., Guinea, F., Peres, N. M. R., Novoselov, K. S. & Geim, A. K. The electronic properties of graphene. *Reviews of Modern Physics* **81,** 109–162. ISSN: 0034-6861, 1539-0756 (Jan. 14, 2009).
6. Wang, L. *et al.* One-Dimensional Electrical Contact to a Two-Dimensional Material. *Science* **342,** 614–617. ISSN: 0036-8075 (2013).
7. Novoselov, K. S. *et al.* A roadmap for graphene. *Nature* **490,** 192–200. ISSN: 0028-0836 (Oct. 11, 2012).
8. Xia, F., Mueller, T., Lin, Y.-M., Valdes-Garcia, A. & Avouris, P. Ultrafast graphene photodetector. *Nature Nanotechnology* **4,** 839–843. ISSN: 1748-3395 (Dec. 2009).
9. Chhowalla, M. *et al.* The chemistry of two-dimensional layered transition metal dichalcogenide nanosheets. *Nature Chemistry* **5,** 263–275. ISSN: 1755-4330 (Apr. 2013).
10. Pospischil, A. & Mueller, T. Optoelectronic Devices Based on Atomically Thin Transition Metal Dichalcogenides. *Applied Sciences* **6.** Number: 3 Publisher: Multidisciplinary Digital Publishing Institute, 78 (Mar. 2016).
11. Kolobov, A. V. & Tominaga, J. *Two-dimensional transition-metal dichalcogenides Springer series in materials science* **volume239.** 1 p. ISBN: 978-3-319-31450-1 (Springer, Switzerland, 2016).
12. Wang, Q. H., Kalantar-Zadeh, K., Kis, A., Coleman, J. N. & Strano, M. S. Electronics and optoelectronics of two-dimensional transition metal dichalcogenides. *Nature Nanotechnology* **7,** 699–712. ISSN: 1748-3387 (Nov. 2012).

13. He, J., Hummer, K. & Franchini, C. Stacking effects on the electronic and optical properties of bilayer transition metal dichalcogenides MoS2, MoSe2, WS2, and WSe2. *Physical Review B* **89.** Publisher: American Physical Society, 075409 (Feb. 10, 2014).
14. McDonnell, S. J. & Wallace, R. M. Atomically-thin layered films for device applications based upon 2D TMDC materials. *Thin Solid Films* **616,** 482–501. ISSN: 0040-6090 (Oct. 1, 2016).
15. Wilson, J. A. & Yoffe, A. D. The transition metal dichalcogenides discussion and interpretation of the observed optical, electrical and structural properties. *Advances in Physics* **18,** 193–335. ISSN: 0001-8732 (May 1, 1969).
16. Kuc, A. in *Chemical Modelling* (eds Springborg, M. & Joswig, J.-O.) 1–29 (Royal Society of Chemistry, Cambridge, 2014). ISBN: 978-1-84973-954-2.
17. Luo, X. *et al.* Stacking sequence determines Raman intensities of observed interlayer shear modes in 2D layered materials – A general bond polarizability model. *Scientific Reports* **5.** ISSN: 2045-2322 (Nov. 2015).
18. Splendiani, A. *et al.* Emerging Photoluminescence in Monolayer MoS2. *Nano Letters* **10.** Publisher: American Chemical Society, 1271–1275. ISSN: 1530-6984 (Apr. 14, 2010).
19. Mak, K. F., Lee, C., Hone, J., Shan, J. & Heinz, T. F. Atomically Thin MoS 2 : A New Direct-Gap Semiconductor. *Physical Review Letters* **105.** ISSN: 0031-9007, 1079-7114 (Sept. 24, 2010).
20. Tongay, S. *et al.* Thermally Driven Crossover from Indirect toward Direct Bandgap in 2D Semiconductors: MoSe $_2$ versus MoS $_2$. *Nano Letters* **12,** 5576–5580. ISSN: 1530-6984, 1530-6992 (Nov. 14, 2012).
21. Zhao, W. *et al.* Evolution of Electronic Structure in Atomically Thin Sheets of WS $_2$ and WSe $_2$. *ACS Nano* **7,** 791–797. ISSN: 1936-0851, 1936-086X (Jan. 22, 2013).
22. Abderrahmane, A. *et al.* High photosensitivity few-layered MoSe2 back-gated field-effect phototransistors. *Nanotechnology* **25.** Publisher: IOP Publishing, 365202. ISSN: 0957-4484 (Aug. 2014).
23. Perea-López, N. *et al.* Photosensor Device Based on Few-Layered WS2 Films. *Advanced Functional Materials* **23,** 5511–5517. ISSN: 1616-3028 (2013).
24. Zhang, W. *et al.* Role of Metal Contacts in High-Performance Phototransistors Based on WSe2 Monolayers. *ACS Nano* **8.** Publisher: American Chemical Society, 8653–8661. ISSN: 1936-0851 (Aug. 26, 2014).
25. Lopez-Sanchez, O., Lembke, D., Kayci, M., Radenovic, A. & Kis, A. Ultrasensitive photodetectors based on monolayer MoS 2. *Nature Nanotechnology* **8.** Number: 7 Publisher: Nature Publishing Group, 497–501. ISSN: 1748-3395 (July 2013).

26. Lee, H. S. *et al.* MoS2 Nanosheet Phototransistors with Thickness-Modulated Optical Energy Gap. *Nano Letters* **12.** Publisher: American Chemical Society, 3695–3700. ISSN: 1530-6984 (July 11, 2012).
27. Aydinli, A., Gasanly, N. M. & Gökşen, K. Donor–acceptor pair recombination in gallium sulfide. *Journal of Applied Physics* **88,** 7144–7149. ISSN: 0021-8979, 1089-7550 (Dec. 15, 2000).
28. Gasanly, N. M., Aydınlı, A., Özkan, H. & Kocabaş, C. Temperature dependence of the first-order Raman scattering in GaS layered crystals. *Solid State Communications* **116,** 147–151. ISSN: 0038-1098 (Sept. 5, 2000).
29. Aulich, E., Brebner, J. L. & Mooser, E. Indirect Energy Gap in GaSe and GaS. *physica status solidi (b)* **31,** 129–131. ISSN: 1521-3951 (Jan. 1, 1969).
30. Ho, C. H. & Lin, S. L. Optical properties of the interband transitions of layered gallium sulfide. *Journal of Applied Physics* **100,** 083508. ISSN: 0021-8979, 1089-7550 (Oct. 15, 2006).
31. Springford, M. The Luminescence Characteristics of Some Group III-VI Compounds. *Proceedings of the Physical Society* **82.** Publisher: IOP Publishing, 1020–1028. ISSN: 0370-1328 (Dec. 1963).
32. Cingolani, A., Minafra, A., Tantalo, P. & Paorici, C. Edge emission in GaSe and GaS. *physica status solidi (a)* **4,** K83–K85. ISSN: 1521-396X (1971).
33. Catalano, I. M., Ferrara, M. & Tantalo, P. Luminescence and photocurrent of gallium sulphide. *physica status solidi (a)* **20,** K135–K138. ISSN: 1521-396X (1973).
34. Jin, C., Kim, H., Park, S. & Lee, C. Effects of substrate temperature on the evolution of GaS nanostructures and their photoluminescence properties. *Journal of the Korean Physical Society* **61,** 1298–1302. ISSN: 1976-8524 (Oct. 1, 2012).
35. Sinha, G. *et al.* Controlled Growth of Well-Aligned GaS Nanohornlike Structures and Their Field Emission Properties. *ACS Applied Materials & Interfaces* **3,** 2130–2135. ISSN: 1944-8244 (June 22, 2011).
36. Akhundov, G. A., Gasumov, G. M. & Ismailov, F. I. Photoluminescence of GaSxSe1-x. *Optics and Spectroscopy* **26,** 351. ISSN: 0030-400X (Apr. 1, 1969).
37. Karaman, M. I. & Mushinskii, V. P. Excitation and Photoluminescence Spectra of GaSxSe(1-x) Crystals. *Soviet Physics: Semincoductors* **4,** 464 (1970).
38. Aono, T., Kase, K. & Kinoshita, A. Near-blue photoluminescence of Zn-doped GaS single crystals. *Journal of Applied Physics* **74,** 2818–2820. ISSN: 0021-8979, 1089-7550 (Aug. 15, 1993).
39. Chiricenco, V., Caraman, M., Rusu, I. I. & Leontie, L. On the luminescence of GaS(Cu) single crystals. *Journal of Luminescence* **101,** 71–77. ISSN: 0022-2313 (Jan. 1, 2003).
40. Shigetomi, S., Sakai, K. & Ikari, T. Photoluminescence of layered semiconductor GaS doped with Mn. *physica status solidi (b)* **241,** 2607–2612. ISSN: 1521-3951 (2004).

41. Ho, C. H., Wu, C. C. & Cheng, Z. H. Crystal structure and electronic structure of GaSe(1-x)Sx series layered solids. *Journal of Crystal Growth* **279,** 321–328. ISSN: 0022-0248 (June 1, 2005).
42. Hu, J. Q., Bando, Y., Zhan, J. H., Liu, Z. W. & Golberg, D. Uniform and high-quality submicrometer tubes of GaS layered crystals. *Applied Physics Letters* **87.** Publisher: American Institute of Physics, 153112. ISSN: 0003-6951 (Oct. 7, 2005).
43. Hu, P. A., Liu, Y. Q., Fu, L., Cao, L. C. & Zhu, D. B. GaS multi-walled nanotubes from the lamellar precursor. *Applied Physics A* **80,** 1413–1417. ISSN: 0947-8396, 1432-0630 (Jan. 27, 2005).
44. Jung, C. S. *et al.* Red-to-Ultraviolet Emission Tuning of Two-Dimensional Gallium Sulfide/Selenide. *ACS Nano* **9.** Publisher: American Chemical Society, 9585–9593. ISSN: 1936-0851 (Oct. 27, 2015).
45. Jung, C. S. *et al.* Photoluminescence and Photocurrents of GaS1–xSex Nanobelts. *Chemistry of Materials* **28,** 5811–5820. ISSN: 0897-4756 (Aug. 23, 2016).
46. Wang, X. *et al.* Chemical Vapor Deposition Growth of Two-Dimensional Monolayer Gallium Sulfide Crystals Using Hydrogen Reduction of Ga2S3. *ACS Omega* **3.** Publisher: American Chemical Society, 7897–7903. ISSN: 2470-1343 (July 31, 2018).
47. Shigetomi, S. & Ikari, T. Radiative centers in GaS doped with Zn and Cd. *Review of Scientific Instruments* **76.** Publisher: American Institute of Physics, 066108. ISSN: 0034-6748 (June 1, 2005).
48. Shigetomi, S. & Ikari, T. Radiative transitions of layered semiconductor GaS doped with P. *Journal of Luminescence* **118,** 106–110. ISSN: 0022-2313 (May 1, 2006).
49. Shigetomi, S. & Ikari, T. Optical properties of layered semiconductor GaS doped with As. *Journal of Applied Physics* **102,** 033701. ISSN: 0021-8979 (Aug. 1, 2007).
50. Shigetomi, S. & Ikari, T. Photoluminescence Studies of Layered Semiconductor GaS Doped with Ge. *Japanese Journal of Applied Physics* **48,** 030211. ISSN: 1347-4065 (Mar. 5, 2009).
51. Shigetomi, S. & Ikari, T. Temperature Dependence of Photoluminescence in Layered Semiconductor n-GaS Doped with Sn. *Japanese Journal of Applied Physics* **49,** 050201. ISSN: 1347-4065 (May 6, 2010).
52. Mercier, A., Mooser, E. & Voitchovsky, J. P. Near edge optical absorption and luminescence of GaSe, GaS and of mixed crystals. *Journal of Luminescence* **7,** 241–266. ISSN: 0022-2313 (Jan. 1, 1973).
53. Wieting, T. J. & Verble, J. L. Interlayer Bonding and the Lattice Vibrations of Beta GaSe. *Physical Review B* **5,** 1473–1479 (Feb. 15, 1972).
54. Kuhn, A., Chevy, A. & Chevalier, R. Crystal structure and interatomic distances in GaSe. *physica status solidi (a)* **31,** 469–475. ISSN: 1521-396X (1975).

55. Terhell, J. C. J. M. Polytypism in the III–VI layer compounds. *Progress in Crystal Growth and Characterization* **7,** 55–110. ISSN: 0146-3535 (Jan. 1, 1983).

56. Schmid, P., Voitchovsky, J. P. & Mercier, A. Impurity effects on low temperature photoluminescence of GaSe. *physica status solidi (a)* **21,** 443–450. ISSN: 1521-396X (1974).

57. Voitchovsky, J. P. & Mercier, A. Photoluminescence ofGaSe. *Il Nuovo Cimento B (1971-1996)* **22,** 273–292. ISSN: 1826-9877 (Aug. 1, 1974).

58. Shigetomi, S., Ikari, T. & Nakashima, H. Electrical and Optical Characteristics of the Layer Semiconductor p-GaSe Doped with Ag. *physica status solidi (a)* **160,** 159–164. ISSN: 1521-396X (1997).

59. Manfredotti, C., Murri, R., Rizzo, A., Vasanelli, L. & Micocci, G. Electrical properties of GaTe grown by various methods. *physica status solidi (a)* **29,** 475–480. ISSN: 1521-396X (June 16, 1975).

60. Brebner, J. L., Fischer, G. & Mooser, E. Optical absorption edge of GaTe. *Journal of Physics and Chemistry of Solids* **23,** 1417–1421. ISSN: 0022-3697 (Oct. 1, 1962).

61. Abdel Rahman, M. & Belal, A. E. Single crystal growth and optical energy gap of gallium telluride. *Journal of Physics and Chemistry of Solids* **61,** 925–929. ISSN: 0022-3697 (June 2000).

62. Pearson, W. B. The crystal structures of semiconductors and a general valence rule. *Acta Crystallographica* **17,** 1–15. ISSN: 0365-110X (1964).

63. Wang, Z. *et al.* High-performance flexible photodetectors based on GaTe nanosheets. *Nanoscale* **7,** 7252–7258. ISSN: 2040-3372 (Apr. 9, 2015).

64. Gillan, E. G. & Barron, A. R. Chemical Vapor Deposition of Hexagonal Gallium Selenide and Telluride Films from Cubane Precursors: Understanding the Envelope of Molecular Control. *Chemistry of Materials* **9,** 3037–3048. ISSN: 0897-4756 (Dec. 1, 1997).

65. Abdullaev, G. B. *et al.* Raman spectra of α-GaTe single crystals. *Solid State Communications* **31,** 851–855. ISSN: 0038-1098 (Sept. 1, 1979).

66. Irwin, J. C., Clayman, B. P. & Mead, D. G. Long-wavelength phonons in GaTe. *Physical Review B* **19,** 2099 (1979).

67. Pozo-Zamudio, O. D. *et al.* Photoluminescence of two-dimensional GaTe and GaSe films. *2D Materials* **2,** 035010. ISSN: 2053-1583 (2015).

68. Fonseca, J. J. *et al.* Structure–Property Relationship of Low-Dimensional Layered GaSexTe(1-x) Alloys. *Chemistry of Materials* **30,** 4226–4232. ISSN: 0897-4756 (July 10, 2018).

69. Cai, H. *et al.* Abnormal band bowing effects in phase instability crossover region of GaSe1-xTe x nanomaterials. *Nature Communications* **9.** ISSN: 2041-1723 (Dec. 2018).

70. Zhao, Q. *et al.* Thickness-induced structural phase transformation of layered gallium telluride. *Phys. Chem. Chem. Phys.* **18,** 18719–18726. ISSN: 1463-9076, 1463-9084 (2016).
71. Bae, C. J. *et al.* Influence of thickness on crystallinity in wafer-scale GaTe nanolayers grown by molecular beam epitaxy. *AIP Advances* **7.** Publisher: American Institute of Physics, 035113 (Mar. 1, 2017).
72. Fonseca, J. J. *et al.* Bandgap Restructuring of the Layered Semiconductor Gallium Telluride in Air. *Advanced Materials* **28,** 6465–6470. ISSN: 1521-4095 (Aug. 1, 2016).
73. Yang, S. *et al.* Environmental stability of 2D anisotropic tellurium containing nanomaterials: anisotropic to isotropic transition. *Nanoscale* **9,** 12288–12294. ISSN: 2040-3372 (Aug. 31, 2017).
74. Hu, P. *et al.* Highly Responsive Ultrathin GaS Nanosheet Photodetectors on Rigid and Flexible Substrates. *Nano Letters* **13,** 1649–1654. ISSN: 1530-6984 (Apr. 10, 2013).
75. Hu, P., Wen, Z., Wang, L., Tan, P. & Xiao, K. Synthesis of Few-Layer GaSe Nanosheets for High Performance Photodetectors. *ACS Nano* **6,** 5988–5994. ISSN: 1936-0851 (July 24, 2012).
76. Li, X. *et al.* Controlled Vapor Phase Growth of Single Crystalline, Two-Dimensional GaSe Crystals with High Photoresponse. *Scientific Reports* **4.** ISSN: 2045-2322 (June 30, 2014).
77. Zhou, Y. *et al.* Epitaxy and Photoresponse of Two-Dimensional GaSe Crystals on Flexible Transparent Mica Sheets. *ACS Nano* **8,** 1485–1490. ISSN: 1936-0851 (Feb. 25, 2014).
78. Li, X. *et al.* Two-dimensional GaSe/MoSe2 misfit bilayer heterojunctions by van der Waals epitaxy. *Science Advances* **2.** Publisher: American Association for the Advancement of Science Section: Research Article, e1501882. ISSN: 2375-2548 (Apr. 1, 2016).
79. Liu, F. *et al.* High-Sensitivity Photodetectors Based on Multilayer GaTe Flakes. *ACS Nano* **8,** 752–760. ISSN: 1936-0851 (Jan. 28, 2014).
80. Lieber, C. M. One-dimensional nanostructures: Chemistry, physics & applications. *Solid State Communications* **107,** 607–616. ISSN: 0038-1098 (Aug. 7, 1998).
81. Dai, X., Tchernycheva, M. & Soci, C. in *Semiconductors and Semimetals* 75–107 (Elsevier, 2016). ISBN: 978-0-12-804016-4.
82. Ertekin, E., Greaney, P. A., Chrzan, D. C. & Sands, T. D. Equilibrium limits of coherency in strained nanowire heterostructures. *Journal of Applied Physics* **97.** Publisher: American Institute of Physics, 114325. ISSN: 0021-8979 (June 1, 2005).
83. Wagner, R. S. & Ellis, W. C. Vapor-Liquid-Solid Mechanism of Single Crystal Growth. *Applied Physics Letters* **4,** 89–90. ISSN: 0003-6951, 1077-3118 (Mar. 1, 1964).
84. Law, M., Goldberger, J. & Yang, P. Semiconductor Nanowires and Nanotubes. *Annual Review of Materials Research* **34,** 83–122 (2004).

85. Rehman, S., Shehzad, M. A., Hafeez, M. & Bhatti, A. S. Essential role of catalysts (Mn, Au, and Sn) in the vapor liquid solid growth kinematics of ZnS nanowires. *Journal of Applied Physics* **115,** 024312. ISSN: 0021-8979, 1089-7550 (Jan. 14, 2014).

86. Hu, J., Odom, T. W. & Lieber, C. M. Chemistry and Physics in One Dimension: Synthesis and Properties of Nanowires and Nanotubes. *Accounts of Chemical Research* **32,** 435–445. ISSN: 0001-4842 (May 1, 1999).

87. Choi, H.-J. in *Semiconductor Nanostructures for Optoelectronic Devices: Processing, Characterization and Applications* (ed Yi, G.-C.) 1–36 (Springer, Berlin, Heidelberg, 2012). ISBN: 978-3-642-22480-5.

88. Sutter, E., French, J. S., Sutter, S., Idrobo, J. C. & Sutter, P. Vapor–Liquid–Solid Growth and Optoelectronics of Gallium Sulfide van der Waals Nanowires. *ACS Nano.* Publisher: American Chemical Society. ISSN: 1936-0851 (May 5, 2020).

89. Peng, H., Meister, S., Chan, C. K., Zhang, X. F. & Cui, Y. Morphology control of layer-structured gallium selenide nanowires. *Nano letters* **7,** 199–203 (2007).

90. Panda, S. K. *et al.* Synthesis of Well-Crystalline GaS Nanobelts and Their Unique Field Emission Behavior. *The Journal of Physical Chemistry C* **112,** 6240–6244. ISSN: 1932-7447, 1932-7455 (Apr. 2008).

91. Shen, G., Chen, D., Chen, P.-C. & Zhou, C. Vapor-Solid Growth of One-Dimensional Layer-Structured Gallium Sulfide Nanostructures. *ACS Nano* **3,** 1115–1120. ISSN: 1936-0851 (May 26, 2009).

92. Pan, A. *et al.* Color-Tunable Photoluminescence of Alloyed CdSxSe1-x Nanobelts. *Journal of the American Chemical Society* **127,** 15692–15693. ISSN: 0002-7863 (Nov. 1, 2005).

93. Liu, Y. *et al.* Helical van der Waals crystals with discretized Eshelby twist. *Nature* **570,** 358–362. ISSN: 0028-0836, 1476-4687 (June 2019).

94. Sutter, P., Wimer, S. & Sutter, E. Chiral twisted van der Waals nanowires. *Nature* **570,** 354. ISSN: 1476-4687 (June 2019).

95. Tsai, A. .-P. A test of Hume-Rothery rules for stable quasicrystals. *Journal of Non-Crystalline Solids. 8th International Conference on Quasicrystals* **334-335,** 317–322. ISSN: 0022-3093 (Mar. 15, 2004).

96. Van Vechten, J. A. & Bergstresser, T. K. Electronic structures of semiconductor alloys. *Physical Review B* **1,** 3351 (1970).

97. Komsa, H.-P. & Krasheninnikov, A. V. Two-Dimensional Transition Metal Dichalcogenide Alloys: Stability and Electronic Properties. *The Journal of Physical Chemistry Letters* **3,** 3652–3656. ISSN: 1948-7185 (Dec. 6, 2012).

98. Feng, Q. *et al.* Growth of Large-Area 2D MoS2(1-x)Se2x Semiconductor Alloys. *Advanced Materials* **26,** 2648–2653. ISSN: 1521-4095 (2014).

99. Gong, Y. *et al.* Band Gap Engineering and Layer-by-Layer Mapping of Selenium-Doped Molybdenum Disulfide. *Nano Letters* **14,** 442–449. ISSN: 1530-6984 (Feb. 12, 2014).
100. Li, H. *et al.* Growth of Alloy MoS2xSe2(1–x) Nanosheets with Fully Tunable Chemical Compositions and Optical Properties. *Journal of the American Chemical Society* **136,** 3756–3759. ISSN: 0002-7863 (Mar. 12, 2014).
101. Mann, J. *et al.* 2-Dimensional Transition Metal Dichalcogenides with Tunable Direct Band Gaps: MoS2(1–x)Se2x Monolayers. *Advanced Materials* **26,** 1399–1404. ISSN: 1521-4095 (Mar. 1, 2014).
102. Klee, V. *et al.* Superlinear Composition-Dependent Photocurrent in CVD-Grown Monolayer MoS2(1–x)Se2x Alloy Devices. *Nano Letters* **15,** 2612–2619. ISSN: 1530-6984 (Apr. 8, 2015).
103. Yu, P. *et al.* Metal–Semiconductor Phase-Transition in WSe2(1-x)Te2x Monolayer. *Advanced Materials* **29,** 1603991. ISSN: 1521-4095 (2017).
104. Huang, J. *et al.* Stable electrical performance observed in large-scale monolayer WSe2(1-x)S2xwith tunable band gap. *Nanotechnology* **27.** Publisher: IOP Publishing, 13LT01. ISSN: 0957-4484 (Feb. 2016).
105. Duan, X. *et al.* Synthesis of WS $_{2x}$ Se $_{2-2x}$ Alloy Nanosheets with Composition-Tunable Electronic Properties. *Nano Letters* **16,** 264–269. ISSN: 1530-6984, 1530-6992 (Jan. 13, 2016).
106. Qian, X. *et al.* Anisotropic thermal transport in van der Waals layered alloys WSe2(1-x)Te2x. *Applied Physics Letters* **112,** 241901. ISSN: 0003-6951, 1077-3118 (June 11, 2018).
107. Dumcenco, D. O., Chen, K. Y., Wang, Y. P., Huang, Y. S. & Tiong, K. K. Raman study of 2H-Mo1-xWxS2 layered mixed crystals. *Journal of Alloys and Compounds* **506,** 940–943. ISSN: 0925-8388 (Sept. 17, 2010).
108. Dumcenco, D. O., Kobayashi, H., Liu, Z., Huang, Y.-S. & Suenaga, K. Visualization and quantification of transition metal atomic mixing in Mo 1-x W x S 2 single layers. *Nature Communications* **4.** Number: 1 Publisher: Nature Publishing Group, 1351. ISSN: 2041-1723 (Jan. 15, 2013).
109. Tongay, S. *et al.* Two-dimensional semiconductor alloys: Monolayer Mo1-xWxSe2. *Applied Physics Letters* **104.** Publisher: American Institute of Physics, 012101. ISSN: 0003-6951 (Jan. 2, 2014).
110. Zhang, M. *et al.* Two-Dimensional Molybdenum Tungsten Diselenide Alloys: Photoluminescence, Raman Scattering, and Electrical Transport. *ACS Nano* **8,** 7130–7137. ISSN: 1936-0851 (July 22, 2014).

111. Arancia, G., Grandolfo, M., Manfredotti, C. & Rizzo, A. Electron diffraction study of melt- and vapour-grown GaSe1-xSx single crystals. *physica status solidi (a)* **33,** 563–571. ISSN: 1521-396X (1976).

112. Cardetta, V., Mancini, A., Manfredotti, C. & Rizzo, A. Growth and habit of GaSe crystals obtained from vapour by various methods. *Journal of Crystal Growth* **17,** 155–161. ISSN: 00220248 (Dec. 1972).

113. Terhell, J. C. J. M., Brabers, V. A. M. & van Egmond, G. E. Polytype phase transition in the series GaSe1-xSx. *Journal of Solid State Chemistry* **41,** 97–103. ISSN: 0022-4596 (Jan. 1, 1982).

114. Ho, C. & Huang, K. Visible luminescence and structural property of GaSe1-xSx (0≤x≤1) series layered crystals. *Solid State Communications* **136,** 591–594. ISSN: 00381098 (Dec. 2005).

115. Ho, C. H., Wang, S. T., Huang, Y. S. & Tiong, K. K. Structural and luminescent property of gallium chalcogenides GaSe1-x S x layer compounds. *Journal of Materials Science: Materials in Electronics* **20,** 207–210. ISSN: 0957-4522, 1573-482X (S1 Jan. 2009).

116. Nan, H. *et al.* Strong Photoluminescence Enhancement of MoS2 through Defect Engineering and Oxygen Bonding. *ACS Nano* **8.** Publisher: American Chemical Society, 5738–5745. ISSN: 1936-0851 (June 24, 2014).

117. Camassel, J., Merle, P., Mathieu, H. & Gouskov, A. Near-band-edge optical properties of Ga Se x Te 1- x mixed crystals. *Physical Review B* **19,** 1060 (1979).

118. Walukiewicz, W. *et al.* Interaction of Localized Electronic States with the Conduction Band: Band Anticrossing in II-VI Semiconductor Ternaries. *Physical Review Letters* **85,** 1552–1555 (Aug. 14, 2000).

119. Alberi, K. *et al.* Valence-band anticrossing in mismatched III-V semiconductor alloys. *Physical Review B* **75,** 045203. ISSN: 1098-0121, 1550-235X (Jan. 16, 2007).

120. Jaquez, M. *et al.* Growth and characterization of ZnO1-xSx highly mismatched alloys over the entire composition. *Journal of Applied Physics* **118,** 215702. ISSN: 0021-8979, 1089-7550 (Dec. 7, 2015).

121. Weyers, M., Sato, M. S. M. & Ando, H. A. H. Red Shift of Photoluminescence and Absorption in Dilute GaAsN Alloy Layers. *Japanese Journal of Applied Physics* **31.** Publisher: IOP Publishing, L853. ISSN: 1347-4065 (July 1, 1992).

122. Wu, J., Walukiewicz, W. & Haller, E. E. Band structure of highly mismatched semiconductor alloys: Coherent potential approximation. *Physical Review B* **65.** ISSN: 0163-1829, 1095-3795 (June 24, 2002).

123. Hu, P. *et al.* Highly sensitive phototransistors based on two-dimensional GaTe nanosheets with direct bandgap. *Nano Research* **7,** 694–703. ISSN: 1998-0124, 1998-0000 (May 1, 2014).

124. Mercier, A. & Voitchovsky, J. .-P. Donor-acceptor pair recombination and phonon replica in GaSxSe1-x. *Journal of Physics and Chemistry of Solids* **36,** 1411–1417. ISSN: 0022-3697 (Dec. 1, 1975).

125. Wadsten, T. Thermal decomposition of the binary compounds GaS, GaSe and GaTe. *Thermochimica Acta* **29,** 261–264. ISSN: 0040-6031 (Apr. 1, 1979).

126. Late, D. J., Liu, B., Matte, H. S. S. R., Rao, C. N. R. & Dravid, V. P. Rapid Characterization of Ultrathin Layers of Chalcogenides on SiO2/Si Substrates. *Advanced Functional Materials* **22,** 1894–1905. ISSN: 1616-3028 (May 9, 2012).

127. Zemann, J. Crystal structures, 2nd edition, Vol. 2 by R. W. G. Wyckoff. *Acta Crystallographica* **19,** 490–490. ISSN: 0365-110X (1965).

128. Irwin, J. C., Hoff, R. M., Clayman, B. P. & Bromley, R. A. Long wavelength lattice vibrations in GaS and GaSe. *Solid State Communications* **13,** 1531–1536. ISSN: 0038-1098 (Nov. 1, 1973).

129. Taylor, M. J. Raman and infrared spectra and vibrational assignments of gallium (II) sulphide. *Journal of Raman Spectroscopy* **1,** 355–358. ISSN: 1097-4555 (Oct. 1, 1973).

130. Lucazeau, G. Vibrational spectra of a GaS single crystal. *Solid State Communications* **18,** 917–922 (1976).

131. Wang, Z. L., Kong, X. Y. & Zuo, J. M. Induced Growth of Asymmetric Nanocantilever Arrays on Polar Surfaces. *Physical Review Letters* **91.** Publisher: American Physical Society, 185502 (Oct. 30, 2003).

132. Tasker, P. W. The stability of ionic crystal surfaces. *Journal of Physics C: Solid State Physics* **12,** 4977–4984. ISSN: 0022-3719 (Nov. 28, 1979).

133. Ma, C., Ding, Y., Moore, D., Wang, X. & Wang, Z. L. Single-Crystal CdSe Nanosaws. *Journal of the American Chemical Society* **126.** Publisher: American Chemical Society, 708–709. ISSN: 0002-7863 (Jan. 28, 2004).

134. Moore, D., Ronning, C., Ma, C. & Wang, Z. L. Wurtzite ZnS nanosaws produced by polar surfaces. *Chemical Physics Letters* **385,** 8–11. ISSN: 0009-2614 (Feb. 2, 2004).

135. Ross, F. M., Tersoff, J. & Reuter, M. C. Sawtooth Faceting in Silicon Nanowires. *Physical Review Letters* **95.** Publisher: American Physical Society, 146104 (Sept. 29, 2005).

136. Madelung, O. in *Semiconductors: Data Handbook* (ed Madelung, O.) 515–552 (Springer Berlin Heidelberg, Berlin, Heidelberg, 2004). ISBN: 978-3-642-18865-7.

137. Gasanly, N. M. & Aydinli, A. Low-Temperature Raman Scattering Spectra of GaSexS1-x Layered Mixed Crystals. *Crystal Research and Technology* **37,** 1011–1017. ISSN: 1521-4079 (2002).

138. León, C. P., Kador, L., Allakhverdiev, K. R., Baykara, T. & Kaya, A. A. Comparison of the layered semiconductors GaSe, GaS, and GaSe1-xSx by Raman and photoluminescence spectroscopy. *Journal of Applied Physics* **98.** Publisher: American Institute of Physics, 103103. ISSN: 0021-8979 (Nov. 15, 2005).

139. Fortuna, S. A. & Li, X. Metal-catalyzed semiconductor nanowires: a review on the control of growth directions. *Semiconductor Science and Technology* **25.** Publisher: IOP Publishing, 024005. ISSN: 0268-1242 (Jan. 2010).

140. Cao, B. *et al.* in *Nanomaterials* (eds Singh, S. C., Zeng, H., Guo, C. & Cai, W.) 555–620 (Wiley-VCH Verlag GmbH & Co. KGaA, 2012). ISBN: 978-3-527-64682-1.

141. Perkowitz, S. *Optical characterization of semiconductors: infrared, Raman, and photoluminescence spectroscopy Techniques of physics* **14.** 1 p. ISBN: 978-0-08-098427-8 (Academic Press, London ; San Diego, 1993).

142. *Luminescence of Solids* (ed Vij, D. R.) (Springer US, 1998). ISBN: 978-0-306-45643-5.

143. O'Donnell, K. P. & Chen, X. Temperature dependence of semiconductor band gaps. *Applied Physics Letters* **58.** Publisher: American Institute of Physics, 2924–2926. ISSN: 0003-6951 (June 24, 1991).

144. Ringnér, M. What is principal component analysis? *Nature Biotechnology* **26.** Number: 3 Publisher: Nature Publishing Group, 303–304. ISSN: 1546-1696 (Mar. 2008).

145. Jolliffe, I. T. & Cadima, J. Principal component analysis: a review and recent developments. *Philosophical Transactions of the Royal Society A: Mathematical, Physical and Engineering Sciences* **374.** Publisher: Royal Society, 20150202 (Apr. 13, 2016).

146. Lever, J., Krzywinski, M. & Altman, N. Principal component analysis. *Nature Methods* **14.** Number: 7 Publisher: Nature Publishing Group, 641–642. ISSN: 1548-7105 (July 1, 2017).

147. Sholl, D., Steckel, J. A. & Sholl. *Density Functional Theory: A Practical Introduction* ISBN: 978-0-470-44770-3 (John Wiley & Sons, Incorporated, Hoboken, United States, 2009).

148. Baseden, K. A. & Tye, J. W. Introduction to Density Functional Theory: Calculations by Hand on the Helium Atom. *Journal of Chemical Education* **91,** 2116–2123. ISSN: 0021-9584 (Dec. 9, 2014).

149. Frijns, A. J. H., Rindt, C. C. M. & Gaastra-Nedea, S. V. in *Advances in Thermal Energy Storage Systems (Second Edition)* (ed Cabeza, L. F.) 497–542 (Woodhead Publishing, Jan. 1, 2021). ISBN: 978-0-12-819885-8.

150. Kresse, G. & Furthmüller, J. Efficient iterative schemes for ab initio total-energy calculations using a plane-wave basis set. *Physical Review B* **54,** 11169–11186 (Oct. 15, 1996).

151. Hafner, J. Ab-initio simulations of materials using VASP: Density-functional theory and beyond. *Journal of Computational Chemistry* **29,** 2044–2078. ISSN: 1096-987X (2008).

152. Perdew, J. P., Burke, K. & Ernzerhof, M. Generalized Gradient Approximation Made Simple. *Physical Review Letters* **77,** 3865–3868 (Oct. 28, 1996).

153. Heyd, J., Scuseria, G. E. & Ernzerhof, M. Hybrid functionals based on a screened Coulomb potential. *The Journal of Chemical Physics* **118,** 8207–8215. ISSN: 0021-9606 (May 8, 2003).

154. Perdew, J. P. *et al.* Restoring the Density-Gradient Expansion for Exchange in Solids and Surfaces. *Physical Review Letters* **100,** 136406 (Apr. 4, 2008).

155. Sher, A., van Schilfgaarde, M., Chen, A.-B. & Chen, W. Quasichemical approximation in binary alloys. *Physical Review B* **36,** 4279–4295 (Sept. 15, 1987).

156. Chen, A.-B. & Sher, A. *Semiconductor Alloys: Physics and Materials Engineering* ISBN: 978-0-306-45052-5 (Springer US, 1995).

157. Wu, J. *et al.* Origin of the large band-gap bowing in highly mismatched semiconductor alloys. *Physical Review B* **67.** ISSN: 0163-1829, 1095-3795 (Jan. 28, 2003).

158. Shevitski, B. *et al.* Tunable electronic structure in gallium chalcogenide van der Waals compounds. *Physical Review B* **100.** Publisher: American Physical Society, 165112 (Oct. 9, 2019).

159. Cai, H. *et al.* Synthesis and emerging properties of 2D layered III–VI metal chalcogenides. *Applied Physics Reviews* **6.** Publisher: American Institute of Physics, 041312 (Nov. 18, 2019).

Appendix A

Calculations of Alloy Composition

The chemical composition of alloy nanowires is characterized by EDS. A single spot on the nanowire is chosen for EDS measurements, as opposed to obtaining an EDS map of the wire, to minimize nanowire damage for future experiments. An example EDS spectrum is shown in Figure A.1. The calculations for the alloy composition from the EDS spectrum are shown below.

First, the ratio of chalcogen to gallium is calculated:

$$\frac{chalcogens}{gallium} = \frac{S_{at\%} + Te_{at\%}}{S_{at\%} + Te_{at\%} + Ga_{at\%}} \tag{A.1}$$

If the ratio of chalcogen to gallium is 0.50 ± 0.02, then the alloy nanowire is considered stoichiometric. Alloy nanowires that are stoichiometric are then expressed as $\mathrm{GaS}_{1-x}\mathrm{Te}_x$, with the tellurium composition calculated as follows:

$$Te_x = \frac{Te_{at\%}}{S_{at\%} + Te_{at\%}} \tag{A.2}$$

For the alloy nanowire shown in Figure A.1, the chalcogen to gallium ratio is:

$$\frac{chalcogen}{gallium} = \frac{8.00 + 0.90}{8.00 + 0.90 + 8.20} = 0.52 \tag{A.3}$$

Therefore this alloy nanowire is considered stoichiometric and the tellurium composition is:

$$Te_x = \frac{0.90}{8.00 + 0.90} = 0.10 \tag{A.4}$$

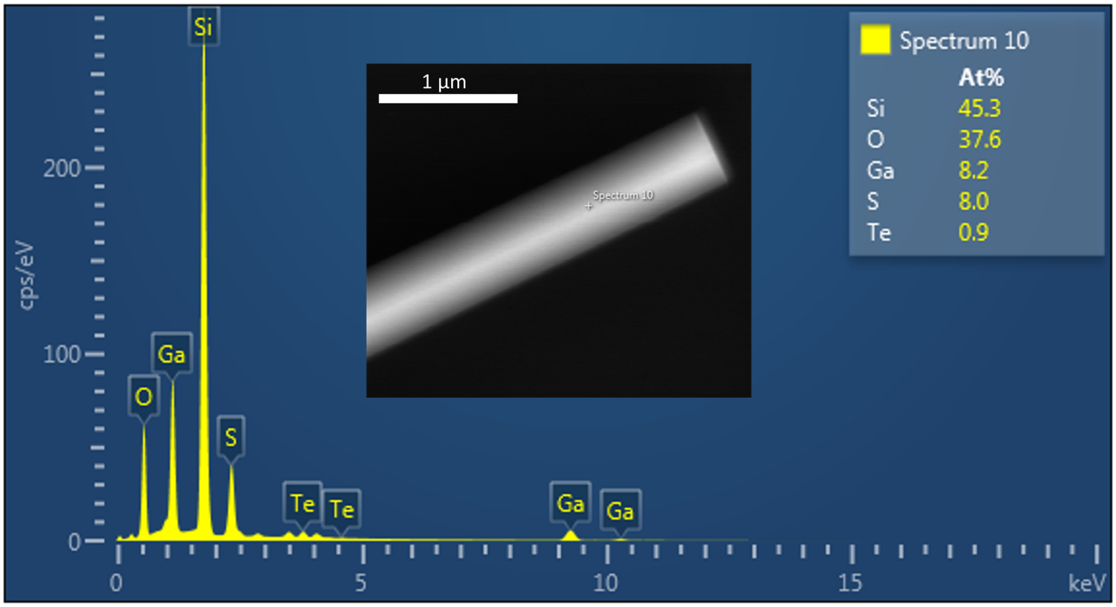

Spectrum 10

	At%
Si	45.3
O	37.6
Ga	8.2
S	8.0
Te	0.9

Figure A.1: EDS spectrum for the alloy nanowire shown in the SEM image.

Appendix B

Parameters for Kinematic Simulations

Lattice Parameter	β-GaS
a = b [Å]	3.59
c [Å]	15.50
α [°]	90
γ [°]	120

Table B.1: Lattice parameters for β-GaS obtained from the Crystallography Open Database (COD ID: 9008966).

Label	Occupancy	x	y	z	m
Ga	$Ga_{1.00}$	0.3333	0.6667	0.1700	4
S	$S_{1.00}$	0.3333	0.6667	0.6000	4

Table B.2: Wyckoff positions for β-GaS obtained from the Crystallography Open Database (COD ID: 9008966).

Label	Occupancy	x	y	z	m
Ga_1	$Ga_{1.00}$	0.3333	0.6667	0.4250	2
Ga_2	$Ga_{1.00}$	0.0000	0.0000	0.0750	2
S_1	$S_{1.00}$	0.6667	0.3333	0.1500	2
S_2	$S_{1.00}$	0.0000	0.0000	0.3500	2

Table B.3: Wyckoff positions for ϵ-GaSe obtained from the Crystallography Open Database (COD ID: 2105478) and adapted for ϵ-GaS.

Appendix C

Laser Power Conversions

Power %	Power (µW)	Spot Area (µm^2)	Power Density (W m^{-2})
0.05	0.6	14.67	0.04
0.1	1.2	22.97	0.05
0.5	4.8	30.05	0.16
1	10.2	29.85	0.29
5	52.6	31.37	1.68
10	110.3	*30	3.68
50	480.3	*30	16.01
100	1012.3	*30	33.74

Table C.1: Table of power conversions for the 488 nm laser line. The power was measured using a micro power sensor (Thor Labs S170C). The objective lens used was 50x with a numerical aperture of 0.75. The spot area was measured by taking optical microscope images of the laser spot size on a Si wafer. *These spot areas were not measured, but they are estimated based on the spot areas for the previous measurements.

Appendix D

Database of Alloy Nanowires

This appendix contains SEM images, Raman spectra, and room-temperature PL spectra for the alloy nanowires selected for Figure 3.9. The PL spectra measured with the 488 nm laser line were processed using a percent filter function with window size of 20 data points. The PL spectra measured with the 660 nm laser line was processed using a Savitzky-Golay function with window size of 50 data points. All PL spectra were processed with a background removal function and fitted with Gaussian functions.

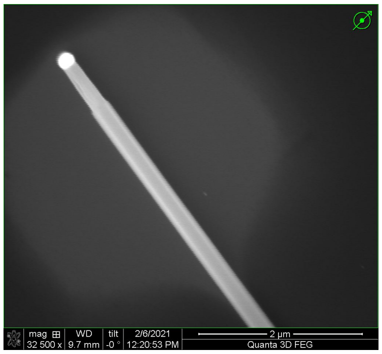

(a) SEM

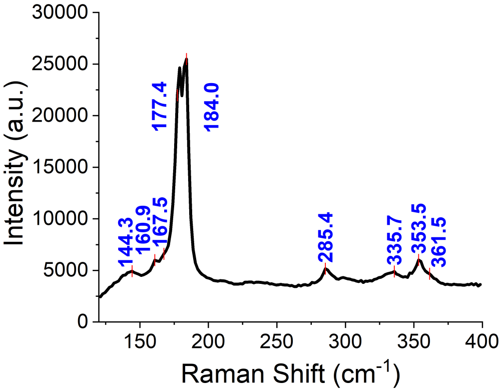

(b) Raman

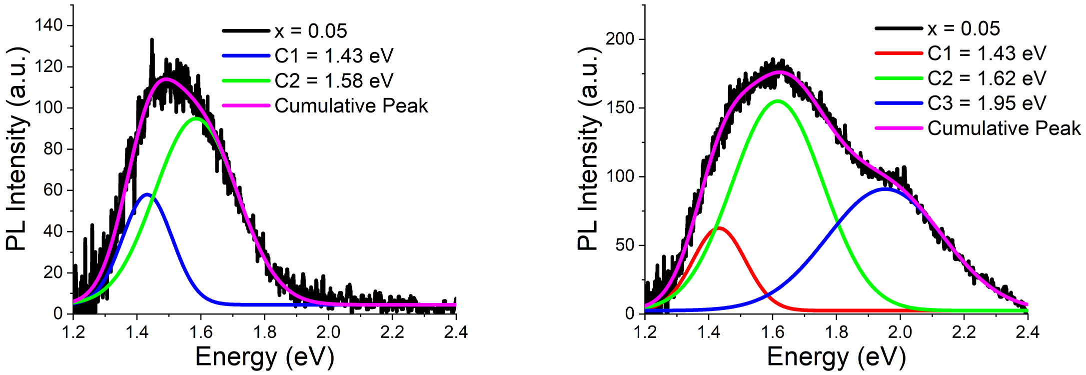

(c) PL 488 nm Laser Line, 100x Objective (d) PL 488 nm Laser Line, 50x Objective

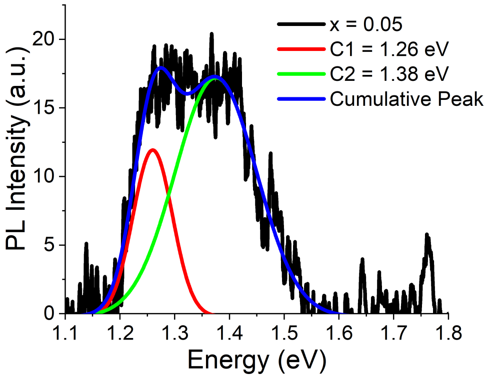

(e) PL 660 nm Laser Line, 50x Objective

Figure D.1: Alloy nanowire with nominal composition of $x = 0.05$ (Wire ID: 14-34 W1).

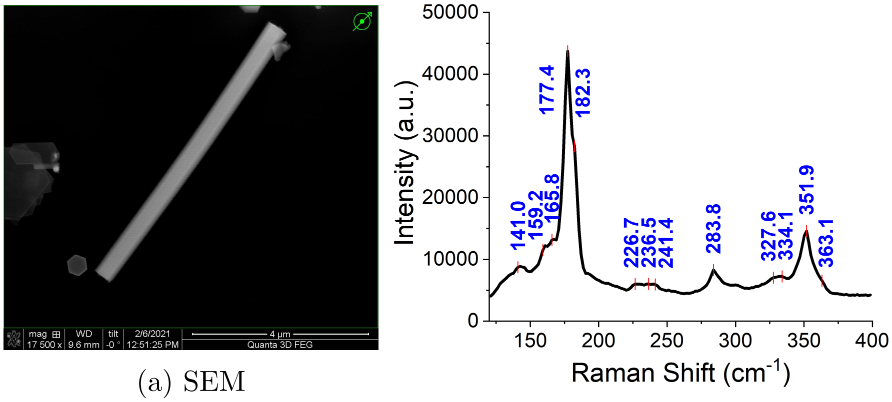

(a) SEM

(b) Raman

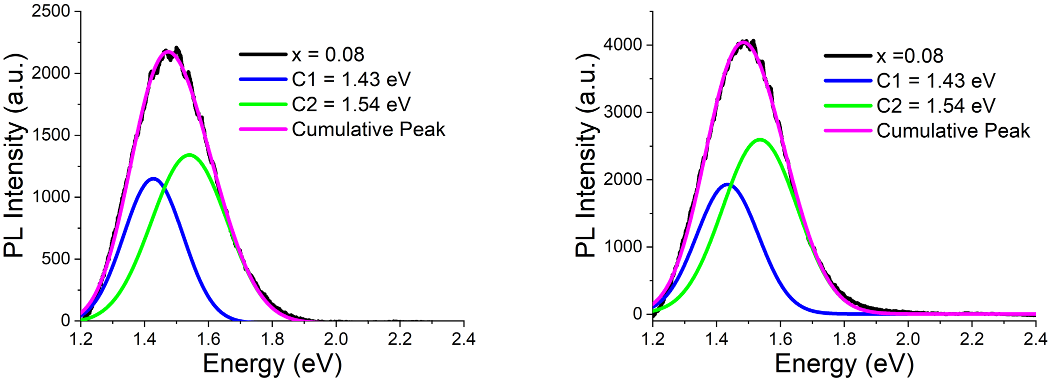

(c) PL 488 nm Laser Line, 100x Objective

(d) PL 488 nm Laser Line, 50x Objective

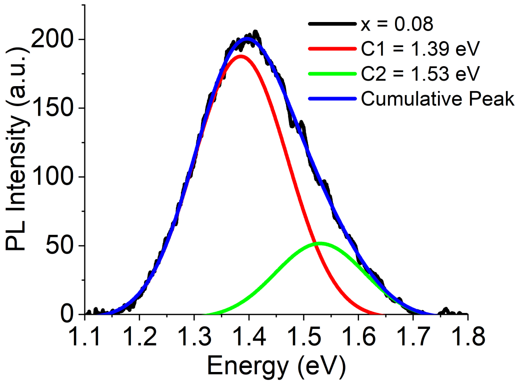

(e) PL 660 nm Laser Line, 50x Objective

Figure D.2: Alloy nanowire with nominal composition of $x = 0.08$ (Wire ID: 15-40 W1).

(a) SEM

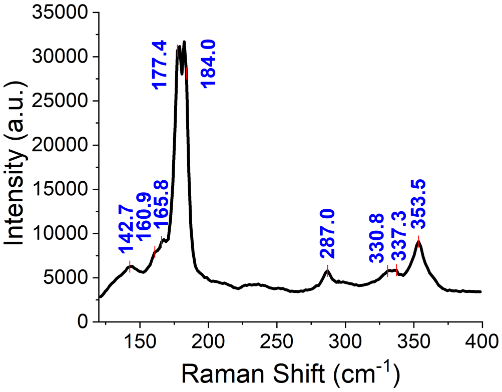

(b) Raman

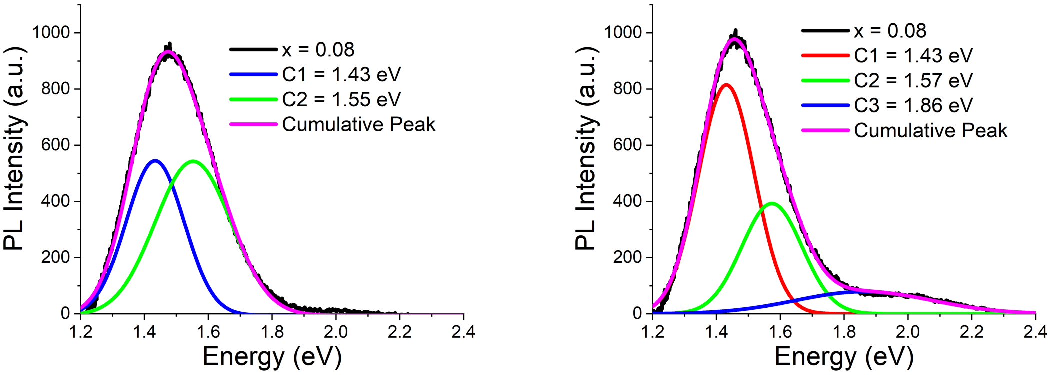

(c) PL 488 nm Laser Line, 100x Objective

(d) PL 488 nm Laser Line, 50x Objective

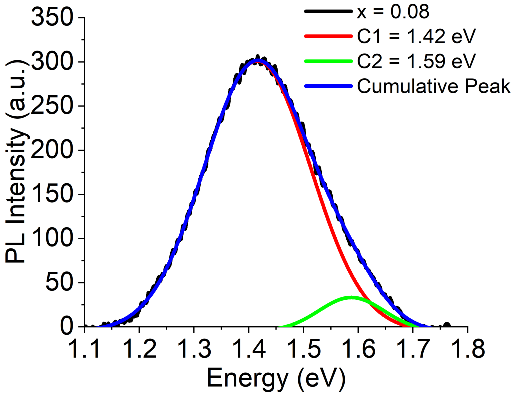

(e) PL 660 nm Laser Line, 50x Objective

Figure D.3: Alloy nanowire with nominal composition of $x = 0.10$ (Wire ID: 15-40 W2).

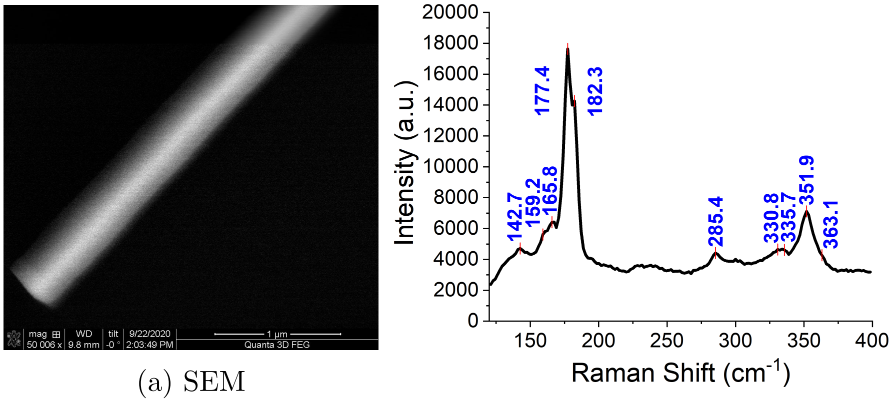

(a) SEM

(b) Raman

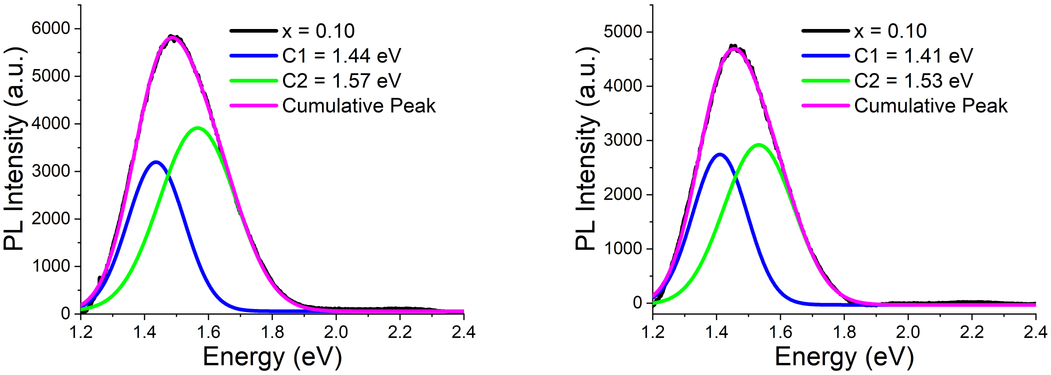

(c) PL 488 nm Laser Line, 100x Objective

(d) PL 488 nm Laser Line, 50x Objective

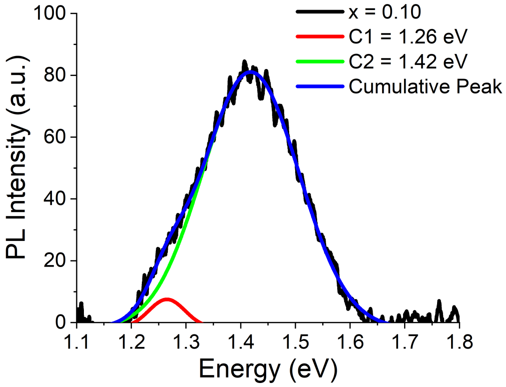

(e) PL 660 nm Laser Line, 50x Objective

Figure D.4: Alloy nanowire with nominal composition of $x = 0.10$ (Wire ID: 12-38 W2).

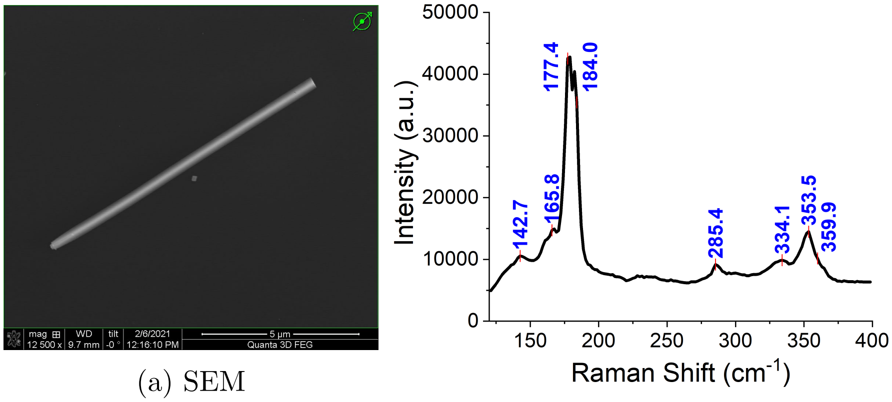

(a) SEM

(b) Raman

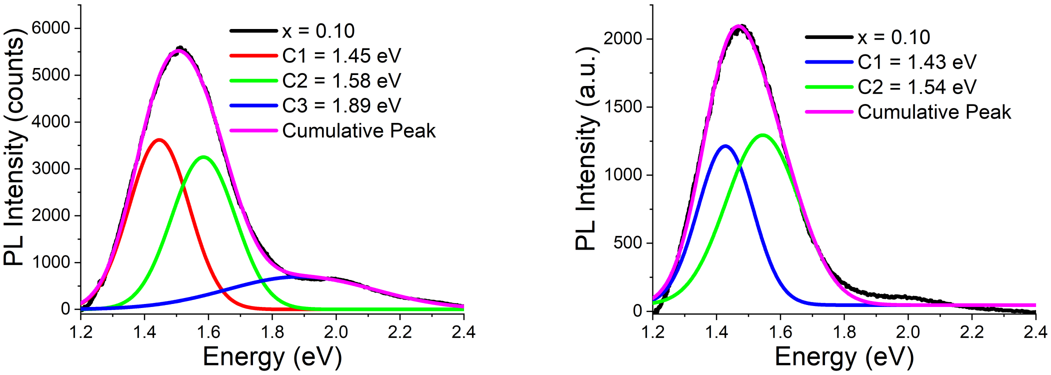

(c) PL 488 nm Laser Line, 100x Objective

(d) PL 488 nm Laser Line, 50x Objective

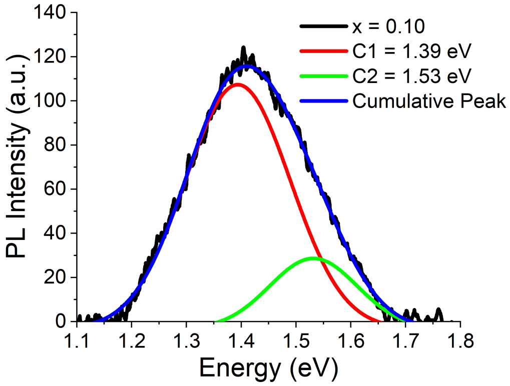

(e) PL 660 nm Laser Line, 50x Objective

Figure D.5: Alloy nanowire with nominal composition of $x = 0.10$ (Wire ID: 14-30 W3).

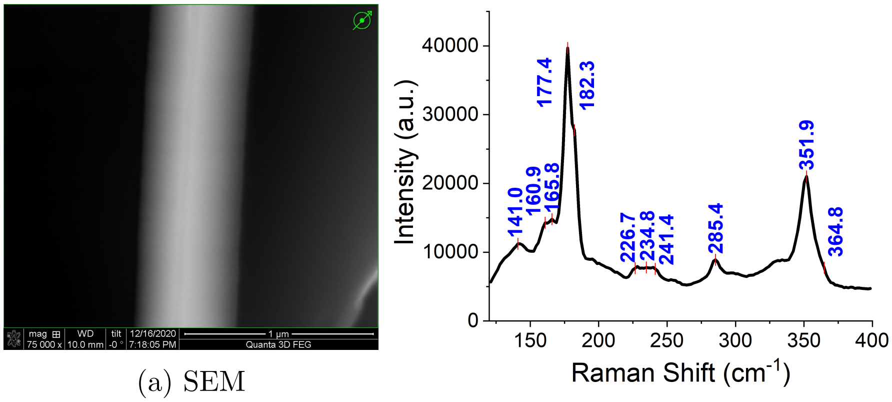

(a) SEM

(b) Raman

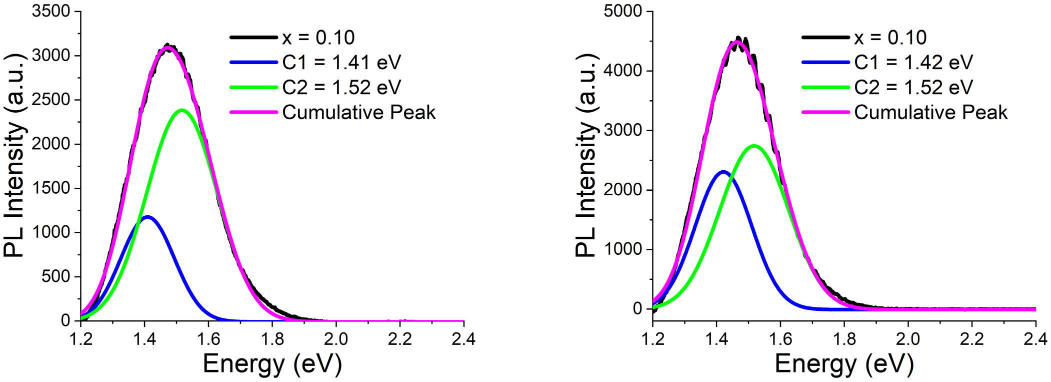

(c) PL 488 nm Laser Line, 100x Objective (d) PL 488 nm Laser Line, 50x Objective

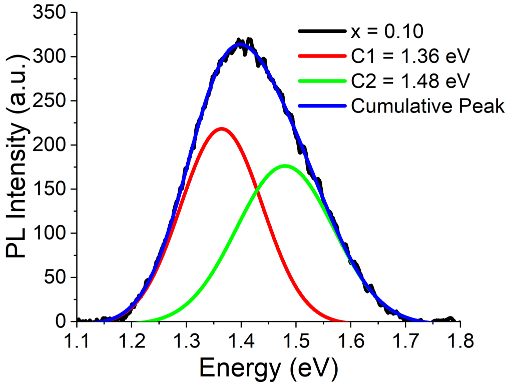

(e) PL 660 nm Laser Line, 50x Objective

Figure D.6: Alloy nanowire with nominal composition of $x = 0.10$ (Wire ID: 15-31 W1).

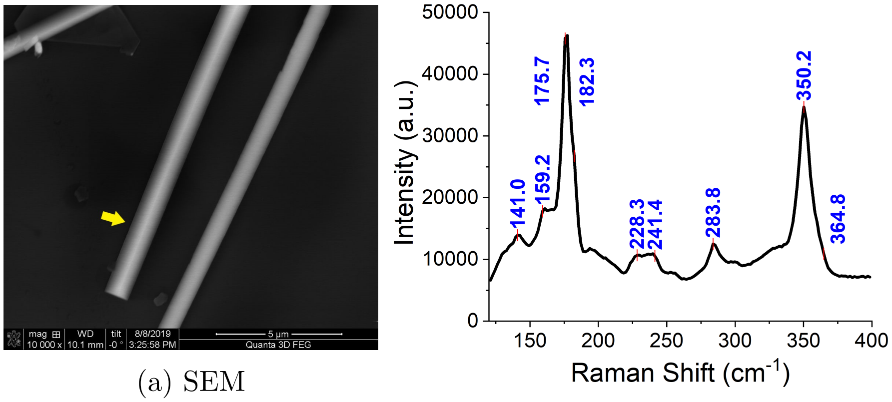

(a) SEM

(b) Raman

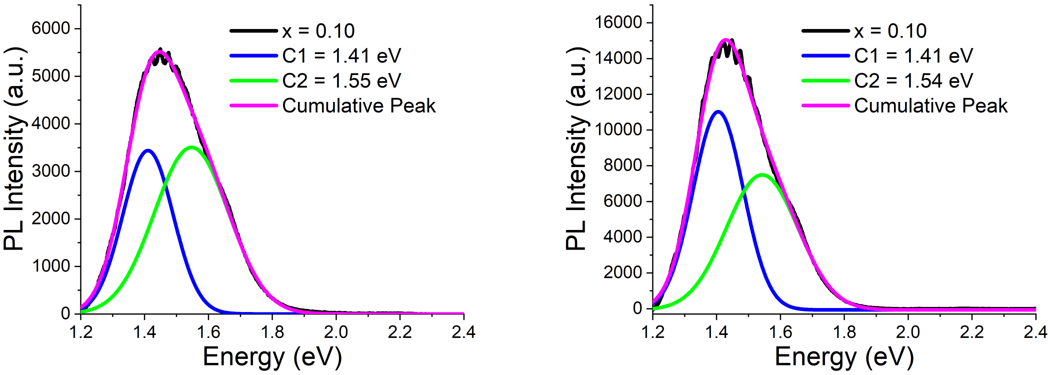

(c) PL 488 nm Laser Line, 100x Objective (d) PL 488 nm Laser Line, 50x Objective

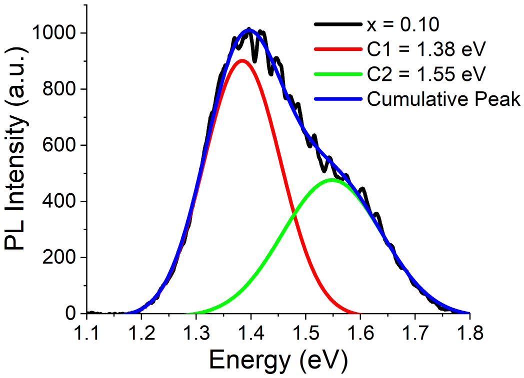

(e) PL 660 nm Laser Line, 50x Objective

Figure D.7: Alloy nanowire with nominal composition of $x = 0.10$ (Wire ID: 15-39 W2).

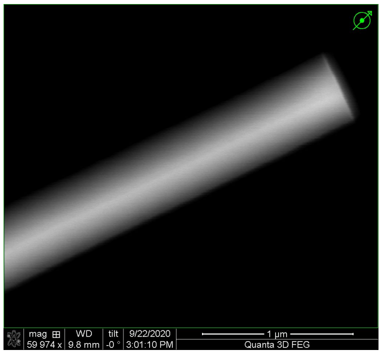

(a) SEM

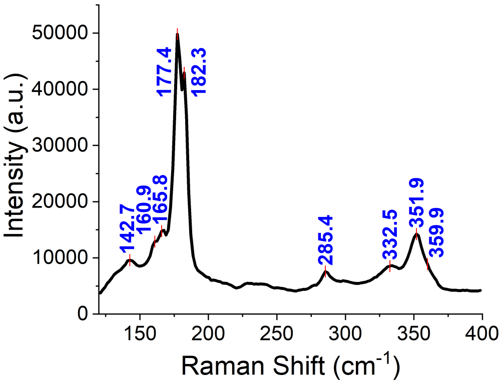

(b) Raman

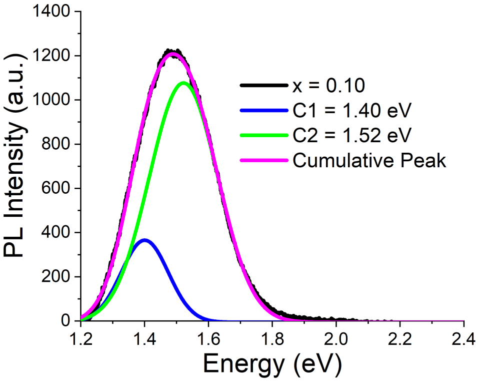

(c) PL 488 nm Laser Line, 100x Objective

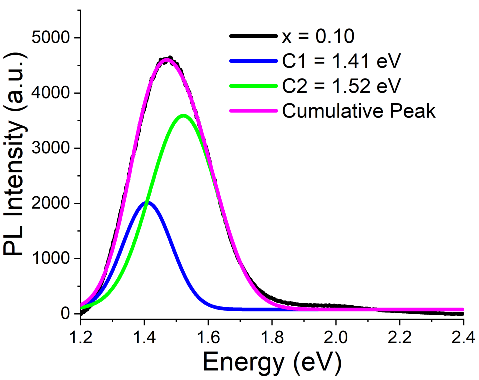

(d) PL 488 nm Laser Line, 50x Objective

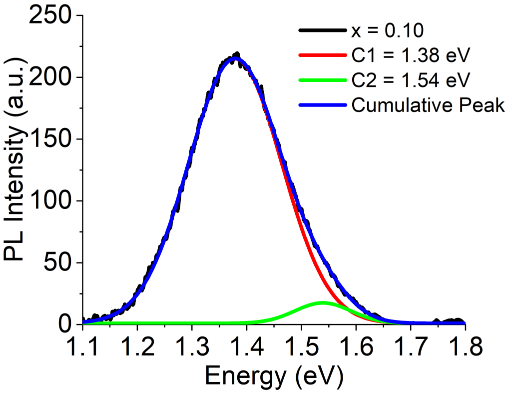

(e) PL 660 nm Laser Line, 50x Objective

Figure D.8: Alloy nanowire with nominal composition of $x = 0.10$ (Wire ID: 15-41 W1).

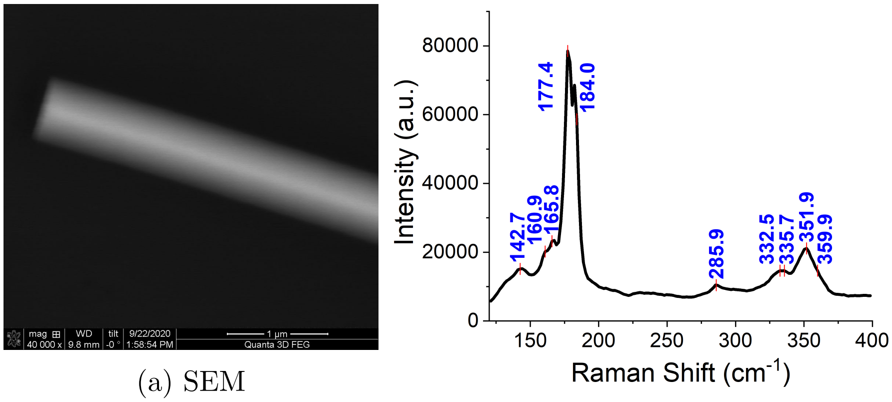

(a) SEM

(b) Raman

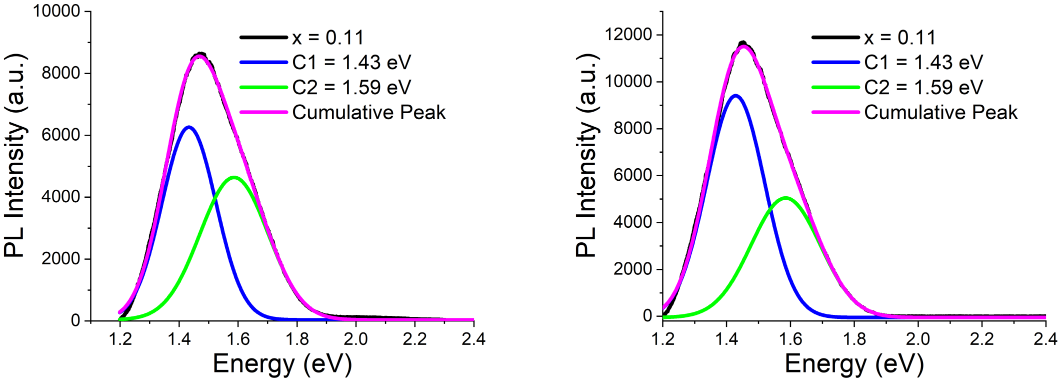

(c) PL 488 nm Laser Line, 100x Objective

(d) PL 488 nm Laser Line, 50x Objective

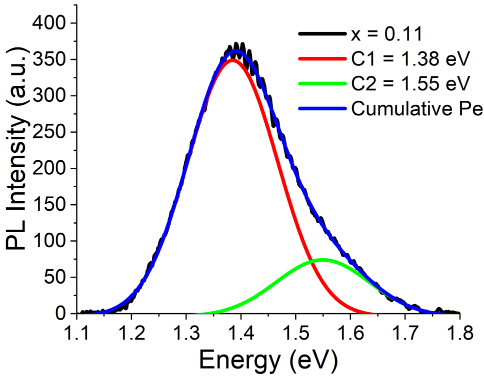

(e) PL 660 nm Laser Line, 50x Objective

Figure D.9: Alloy nanowire with nominal composition of $x = 0.11$ (Wire ID: 12-38 W1).

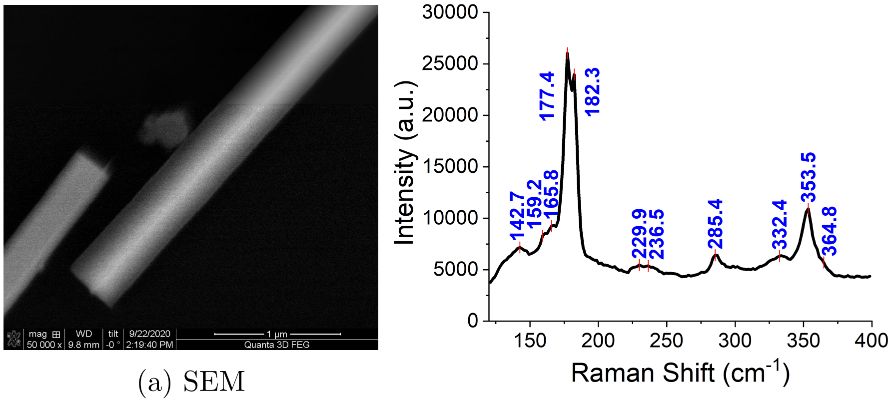

(a) SEM

(b) Raman

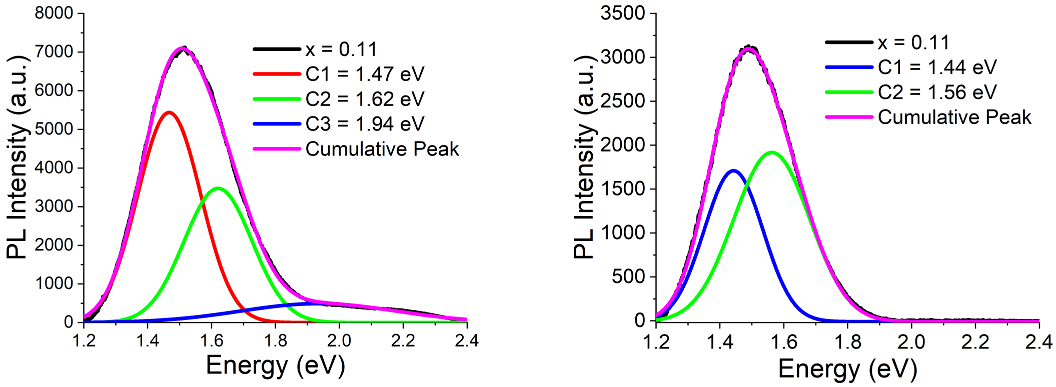

(c) PL 488 nm Laser Line, 100x Objective (d) PL 488 nm Laser Line, 50x Objective

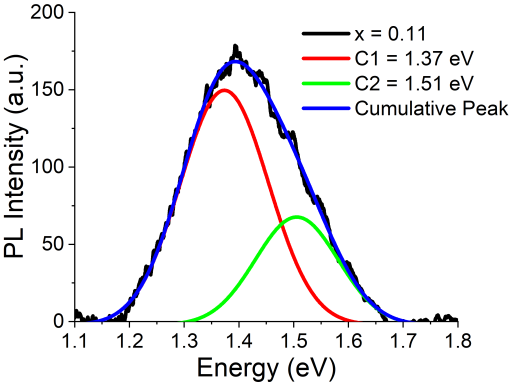

(e) PL 660 nm Laser Line, 50x Objective

Figure D.10: Alloy nanowire with nominal composition of $x = 0.11$ (Wire ID: 14-29 W1).

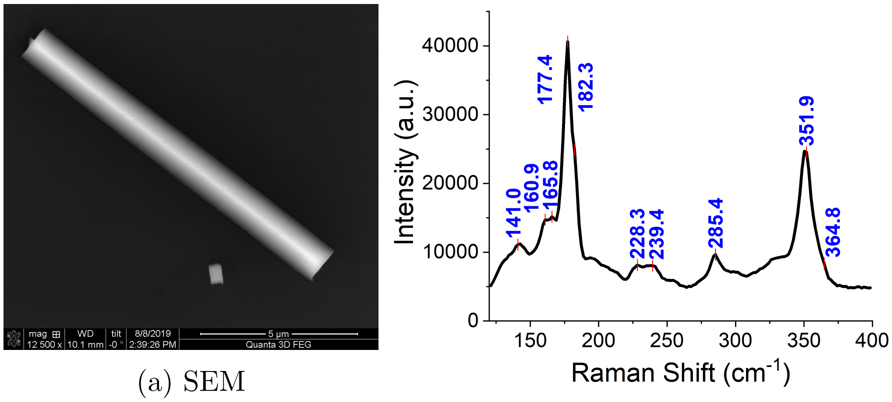

(a) SEM

(b) Raman

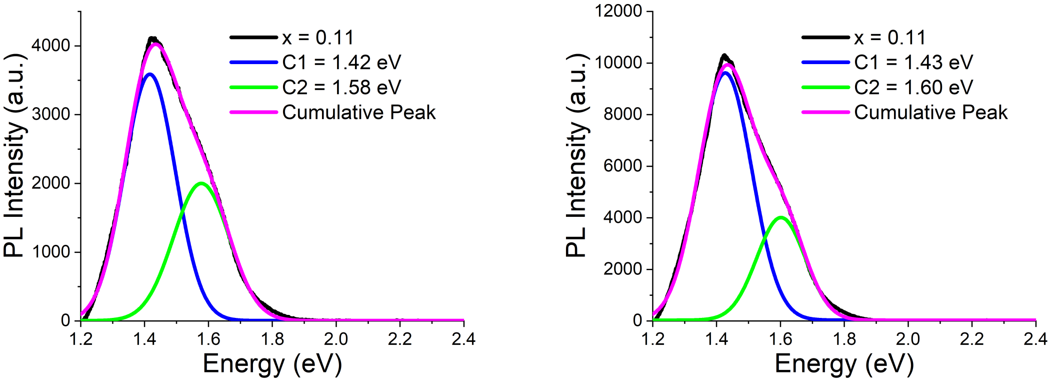

(c) PL 488 nm Laser Line, 100x Objective

(d) PL 488 nm Laser Line, 50x Objective

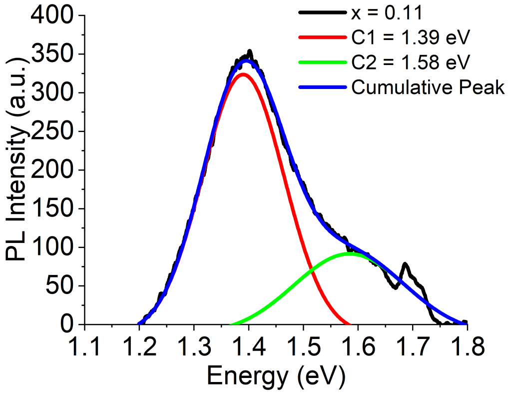

(e) PL 660 nm Laser Line, 50x Objective

Figure D.11: Alloy nanowire with nominal composition of $x = 0.11$ (Wire ID: 14-30 W1).

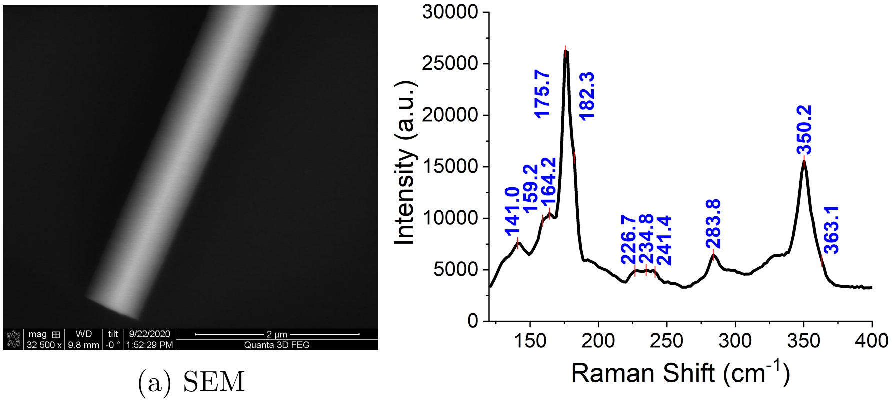

(a) SEM

(b) Raman

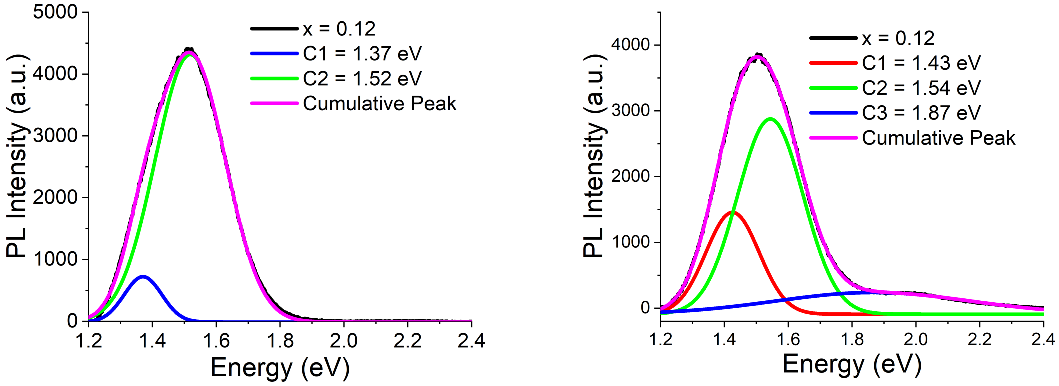

(c) PL 488 nm Laser Line, 100x Objective

(d) PL 488 nm Laser Line, 50x Objective

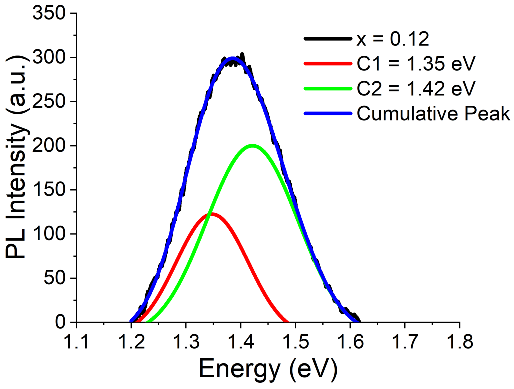

(e) PL 660 nm Laser Line, 50x Objective

Figure D.12: Alloy nanowire with nominal composition of $x = 0.12$ (Wire ID: 11-37 W1).

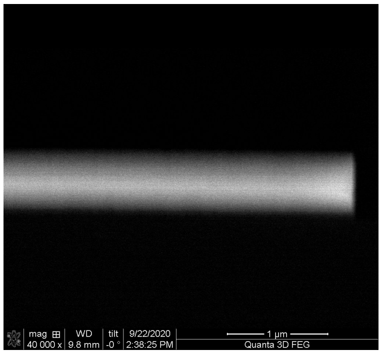

(a) SEM

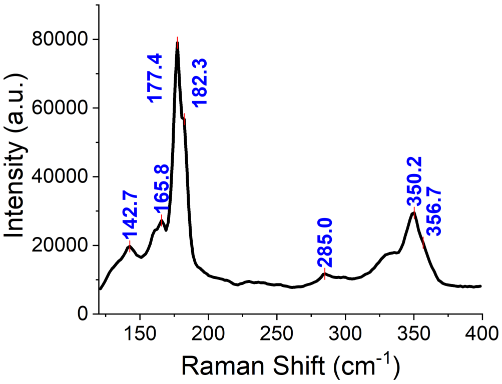

(b) Raman

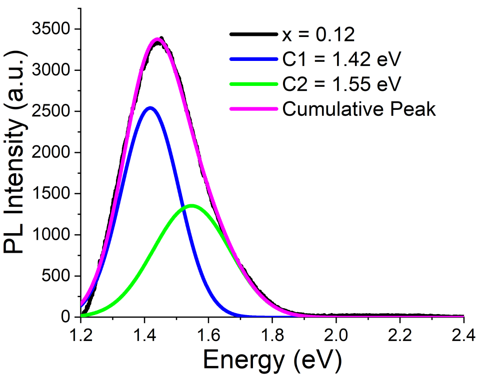

(c) PL 488 nm Laser Line, 100x Objective

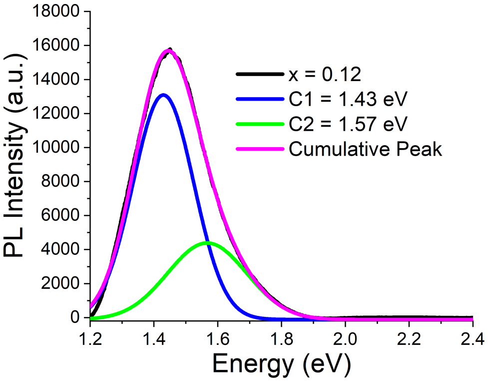

(d) PL 488 nm Laser Line, 50x Objective

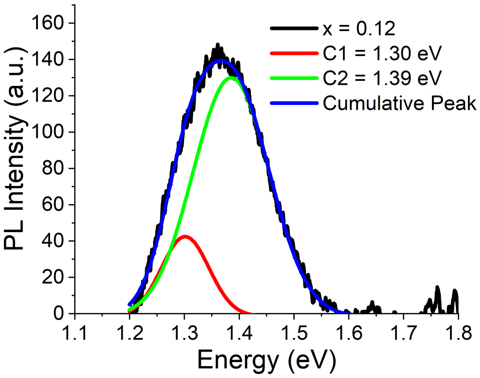

(e) PL 660 nm Laser Line, 50x Objective

Figure D.13: Alloy nanowire with nominal composition of $x = 0.12$ (Wire ID: 14-34 W2).

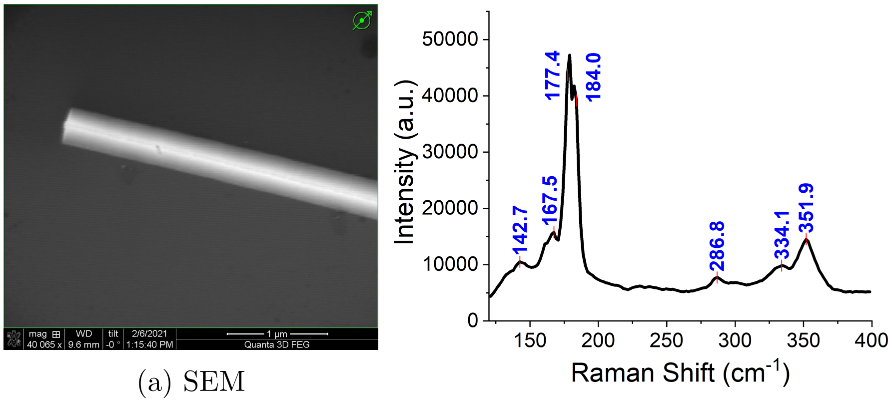

(a) SEM

(b) Raman

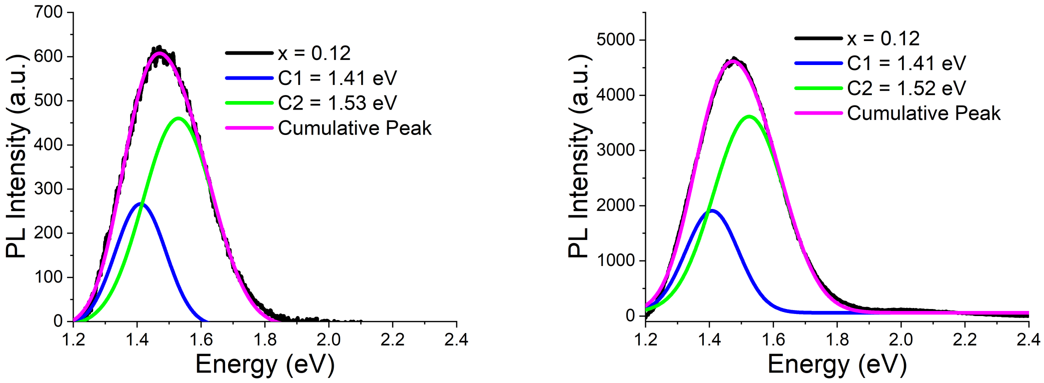

(c) PL 488 nm Laser Line, 100x Objective

(d) PL 488 nm Laser Line, 50x Objective

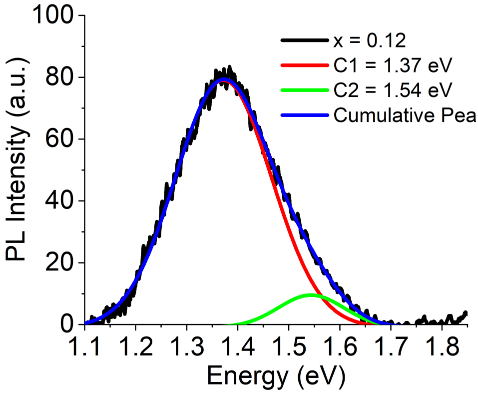

(e) PL 660 nm Laser Line, 50x Objective

Figure D.14: Alloy nanowire with nominal composition of $x = 0.12$ (Wire ID: 15-43 W1).

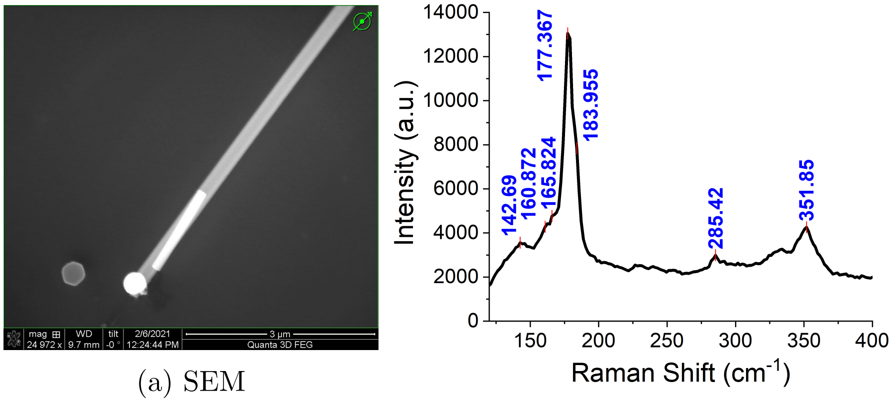

(a) SEM

(b) Raman

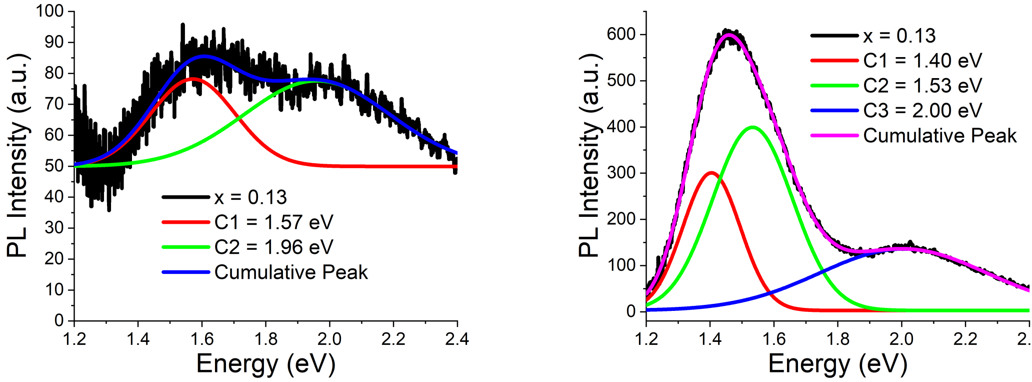

(c) PL 488 nm Laser Line, 100x Objective

(d) PL 488 nm Laser Line, 50x Objective

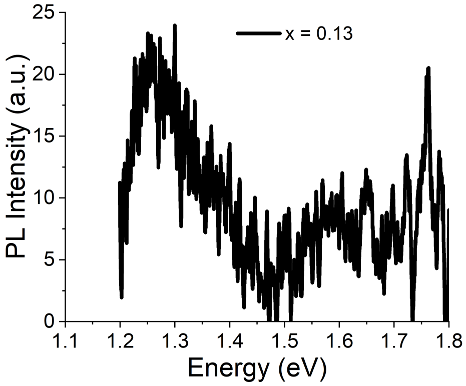

(e) PL 660 nm Laser Line, 50x Objective

Figure D.15: Alloy nanowire with nominal composition of $x = 0.13$ (Wire ID: 15-30 W1).

Appendix E

Density Functional Theory Methods

The following methods for the DFT calculations were provided by Dr. Matthew Horton:

Density Functional Theory (DFT) calculations were performed using VASP[vasp] following recipes provided by the atomate code[atomate]. Standard atomate settings were used, except that geometry optimizations were performed with a stricter force tolerance and using the PBEsol[PBEsol] density functional approximation, since PBEsol improves on the description of bulk solids and has satisfactory performance[PBEsol-dispersion] for geometry of layered materials without the need for additional empirical corrections. Initial structures were taken from the Materials Project as templates with beta-GaS (mp-2507) for the beta-GaS calculation and epsilon-GaSe (mp-1572) for the epsilon-GaS calculation with S substituted. For intermediate compositions it was assumed that Te would randomly incorporate on the S sub-lattice, and so special quasi-random structures were generated to represent each intermediate alloy composition[SQS]. Densities of states were generated for all systems but full band structures were only calculated for the end-points due to band folding for the larger supercells required for the intermediate alloy compositions. Since local functionals are known to systematically under-estimate the band gap, additional calculations were performed using the hybrid HSE06 functional which is known to provide more accurate band gaps[HSE06-gaps] and a scissor correction then applied to the PBEsol densities of states and band structures as appropriate, and visualized using sumo[sumo].

Appendix F

Longer Growth Time of Alloy Nanowires

In this appendix, the growth performed by undergraduate Andre Palacios is presented. The growth performed was three hours long, compared to the 30 minute growths presented in the main body of this dissertation. As shown in Figure F.1, the nanostructures are significantly larger in length and width compared to the 30 minute growths.

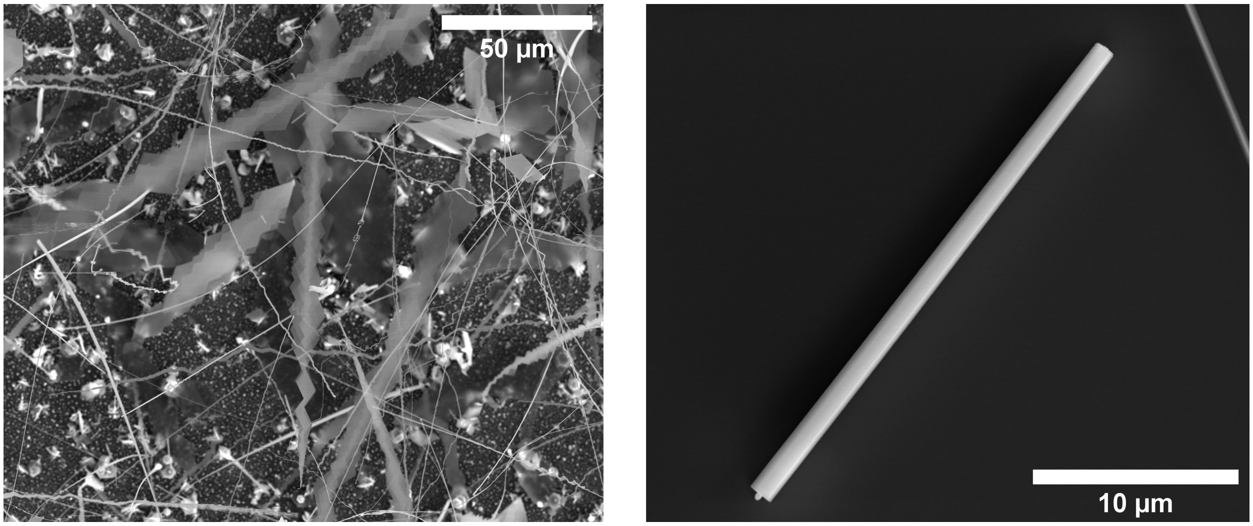

Figure F.1: Alloy nanowire growth performed with a growth time of three hours. Left: SEM image of as-grown sample. Right: SEM image of transferred nanowire.

CL and PL were also performed on alloy nanostructures from this growth, as shown in Figure F.2. The CL was performed at 85 K and the PL was performed at room-temperature with a 488 nm laser line.

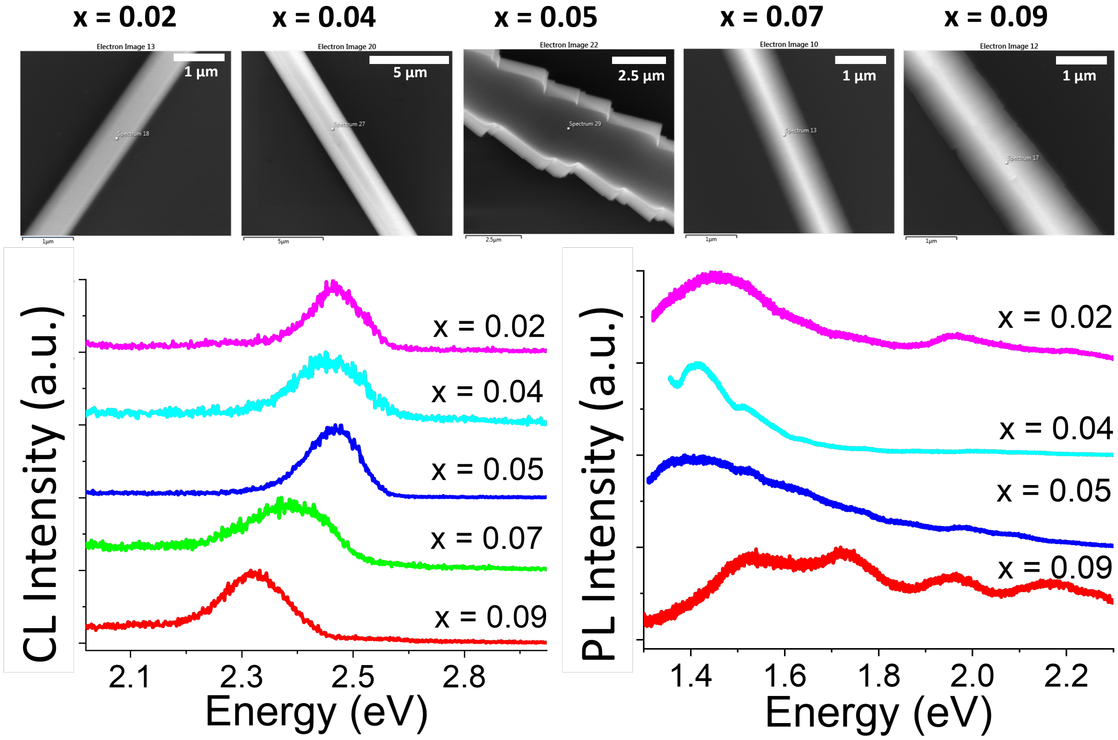

Figure F.2: Room-temperature PL and low-temperature (85 K) CL performed on selected nanostructures from the three-hour long growth shown in Figure F.1.

Appendix G

Nanowire Morpphologies

The following SEM images are from alloy nanowires with different morphologies, sizes, and contrasts in the composition range $0 \leq x \leq 0.10$. The SEM images are a representation of the diversity of nanowires observed in the growths conducted in this work.

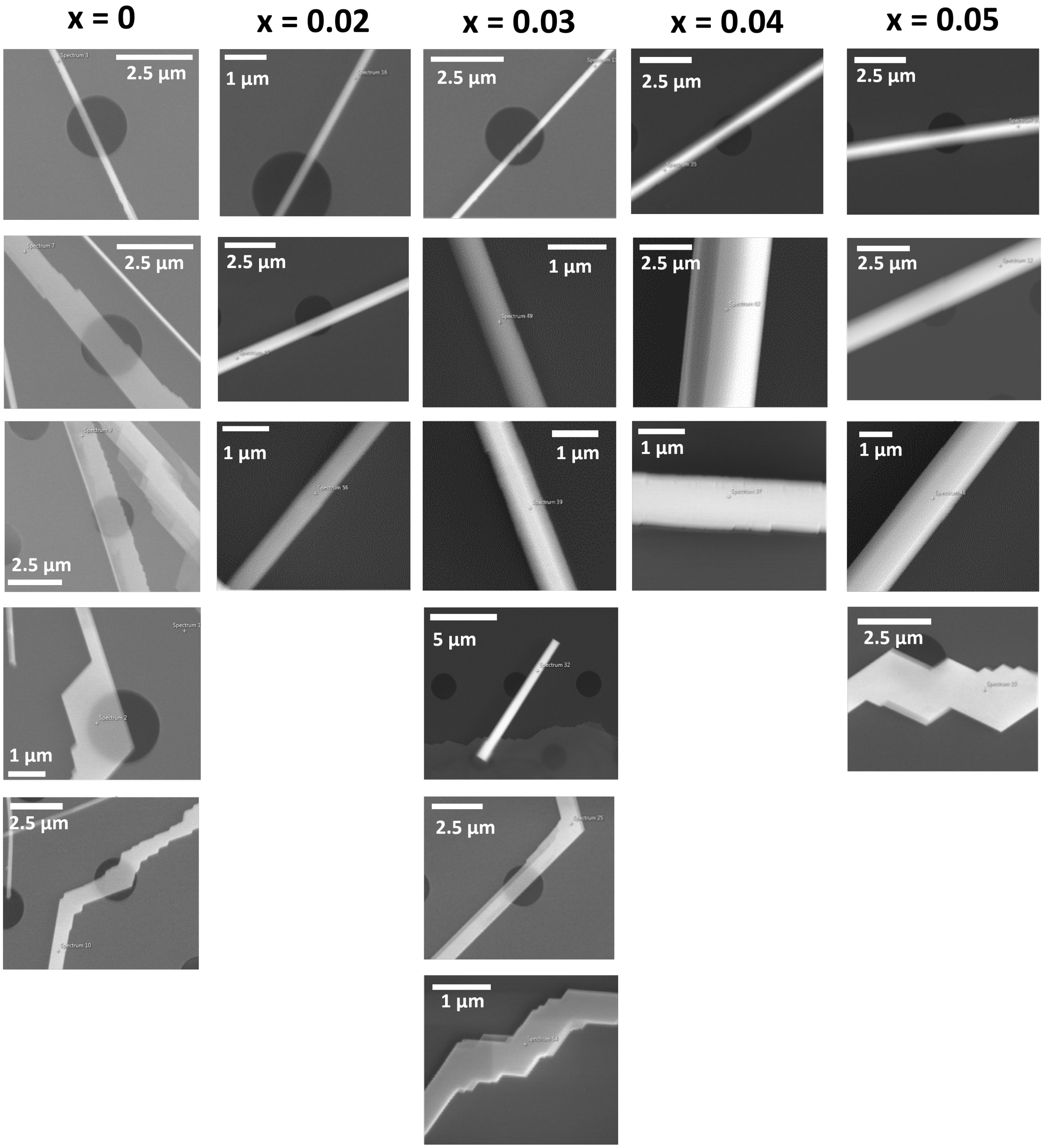

Figure G.1: SEM images of nanowires with composition $0 \leq x \leq 0.05$.

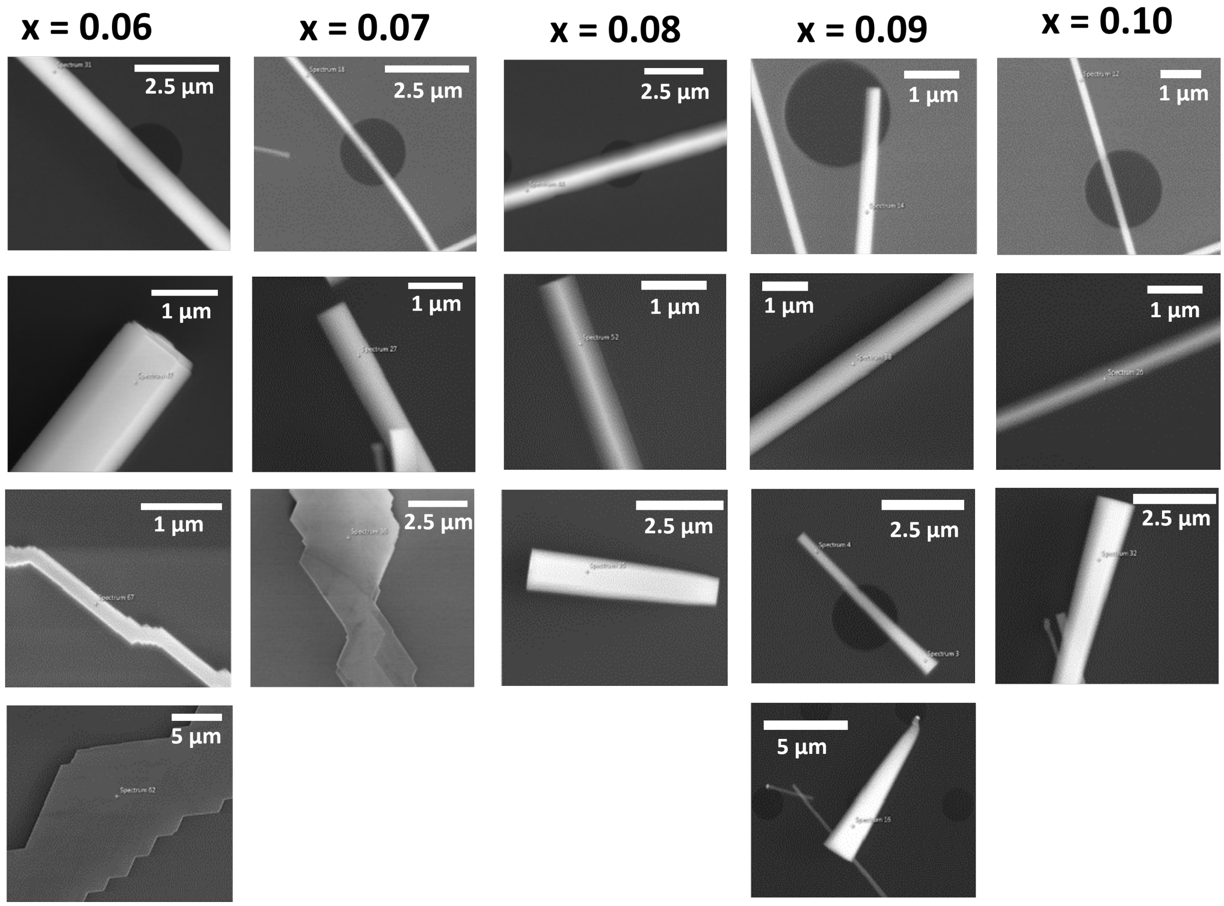

Figure G.2: SEM images of nanowires with composition $0.05 < x \leq 0.10$.